Influence of Topography and Irregular Soil Substructure on Seismic Ground Motion in Two Contrasting Populated Slopes in Lima, Peru

July 2017

GONZALES TRUJILLO, Carlos Eduardo

Graduate School of Engineering

CHIBA UNIVERSITY

（千葉大学審査学位論文）

Influence of Topography and Irregular Soil Substructure on Seismic Ground Motion in Two Contrasting Populated Slopes in Lima, Peru

ペルーのリマ市内の２つの対照的な住民の多い斜面における地震動に与える地形と不整形地盤構造の影響

July 2017

GONZALES TRUJILLO, Carlos Eduardo

Graduate School of Engineering

CHIBA UNIVERSITY

Table of Contents

Chapter 1: Introduction

1.1 Background and Objective

During the last sixty years, Lima, the capital of Peru, has experienced a reconfiguration of the distribution of its population along its territory. The so-called mass migration started as a consequence of the unequal development of the country which accentuated the differences between the urban and rural zones.

Throughout Peruvian history, Lima has always been the politico-economic center and has assumed a privileged position among the other parts of the country. This leading role started to become more evident during the decade of the 50's with the increase in public and private investment in infrastructure that led to the modernization of the metropolis (Matos, 1990). It is in this context that people from different provinces decided to migrate towards the capital aiming for a better standard of living and chose to encroach areas in the outskirts of the city that finally gave rise to shantytowns and human settlements (Riofrio, 2003; Saez et al., 2010).

One of the main problems of these new populated areas is that they were chosen without following any urban planning and, therefore, located in a variety of places such as steep slopes with unfavorable geological and geotechnical characteristics. In addition to that, there is no available information regarding the seismic response of the majority of these slopes since they started to be populated after the last big earthquake that lashed Lima in October 3rd, 1974. Hence, a systematic analysis that includes their particular characteristics is necessary in order to understand the factors that govern their behavior under the effect of strong motions.

There have been plenty of instrumental evidences and field measurements of the complex effects of topography throughout the world. Celebi (1987) studied a hilltop crowned by ridges and canyons in Viña del Mar, Chile. It was found that the damage due to the aftershocks of the March 3rd, 1985 central Chile earthquake (M_S = 7.8) concentrated mainly on the ridges, where all buildings were extremely affected, whereas the structures located in the canyon remain unaffected. Chávez-García et al. (1996, 1997), based on data of small earthquakes collected during summer in 1989 in Empire (Greece), suggested the use of horizontal-to-vertical spectral ratios (HVSR) and a generalized inversion scheme (GIS) in the determination of topographic effects in cases when the information of a reference site is unavailable and, therefore, the calculation of the standard spectral ratio (SSR) is impractical. Athanasopoulos et al. (1999) investigated the effects of the June 15th, 1995 Greece earthquake (M_S = 6.2) on a step-like slope in the most affected town of Egion. In this case, the damage was concentrated in the elevated zone, including the partial collapse of buildings close to the crest, whereas the flat region remained almost intact. This non-uniform damage pattern was attributable to the characteristic surface topography that very likely modified the intensity of the base motion. Kurita et al. (2003) analyzed the influence of the irregular topography in a rocky hill in Yokosuka, Japan by installing seismographs at several heights along the surface, and also within the slope body, and obtained seismic records primarily of the eastward offshore earthquake in Chiba Prefecture (M_J = 6.7) occurred on December 17th, 1987. The comparison of the Fourier spectral ratios showed an increment of the amplification on the way up to the crest, presumably due to a concentration of the energy caused by the reflected waves on the hilltop, in addition to the effect of the slope itself.

On the other hand, various theoretical, numerical and simulation studies have attempted to explain the phenomena of slope topography on seismic ground motions in particular cases. Bouckovalas and Papadimitriou (2005) studied step-like slopes by means of the finite difference method and concluded that the effect of topography is either to amplify or deamplify the peak horizontal seismic motion mainly behind the crest and also to produce a parasitic vertical acceleration. Pitilakis et al. (2004) investigated the slope close to the Aegion fault, Greece which is known to be prone to damage due to topographic effects. Preliminary one-dimensional response analysis, performed in a vertical downhole array located in the foothill, demonstrated that this type of analysis is unable to reproduce the seismic behavior in the time domain as a consequence of the influence of material and geometric discontinuities as well as the significant effect of surface waves originated close to the fault. Ktnediou et al. (2007) attempted to overcome this difficulty and conducted several parametric analyses on various finite difference models of the same site in Greece with the objective of isolating the effects of the topography from others that may influence the final response, such as local geology, frequency content and duration of the seismic motion, impedance contrast between soil layers, etc. Results in each case gave an idea of the complexity of the propagation pattern and also of the uniqueness in the prediction of the behavior for a particular slope. Gelagoti et al. (2010) explored the influence of the subsurface topography in a shallow soft valley by developing a finite element model of the Ohba Valley in Japan. It was also highlighted that the dynamic behavior is strongly dependent on the 2D substructure and cannot possibly be predicted by 1D soil response analysis since diffracted waves at the corners of the valley might aggravate the seismic motion. Jafazadeh et al. (2015) investigated the influence of surface waves generated close to the foot of step-like slopes by the comparison between numerical and scaled physical models and concluded that the effect of Rayleigh waves must be taken into consideration through the estimation of the effective depth of surficial amplification.

As it could be seen, distinct empirical efforts, as well as numerical and physical ones, have indicated that, under certain conditions, seismic motions might be affected due to topography (Ashford et al., 1997), with each case demanding a particular understanding of the mechanism governing the propagation pattern.

In the specific situation of the populated slopes in the city of Lima, this problem has been roughly outlined and the identification of susceptible critical zones due to the effect of earthquakes has been conducted by means of geological visual fieldworks only (Nuñez and Vasquez, 2009).

Therefore, it is the objective of the present work to estimate and comprehend the mechanisms governing the seismic behavior of populated slopes in Lima by means of more accurate and numerical tools. Two study cases with contrasting characteristics are presented, one corresponding to a rocky basin-shaped populated slope and the other located in a sandy dune, which intend to encompass the wide range of different geological and geotechnical conditions affecting their response.

- **Estimation of Shear-wave Velocity Profiles along the Populated Slopes**

Dynamic characterization of the soil substructure of the considered populated slopes was achieved mainly in the form of shear-wave velocity profiles along their respective surface.

Two different types of field surveys were utilized in order to extract reliable dispersion curves at selected locations along the topographic reliefs. First, passive surface waves methods consisting of circular microtremor arrays of different radius size were carried out. Information recorded by velocity sensors arranged in a polygonal deployment was processed by means of the widespread SPAC (Aki, 1957) and F-k techniques (Capon, 1969). Furthermore, the more recent development of the CCA (Cho et al., 2004) and the nc-CCA (Tada et al., 2007) methods allowed the deeper penetration of the soil structure for the same array size and, therefore, these formulations were also adopted in the analysis.

Second, active surface wave methods were also employed in the exploration of the shallowest part of the soil profile. This category includes the execution of linear arrays of velocimeters and the implementation of MASW tests (Park et al., 1999).

It is important to underline that the process of estimating shear-wave velocity profiles considers the verification of the results through the comparison of the fundamental period of the soil obtained from single point microtremor measurements conducted on the same location.

- **Dynamic, Geometric and Two-Dimensional Finite Element Modeling**

Information regarding the estimated shear-wave velocity profiles along the populated slopes in Chapter 3 is representative for the areas in the vicinities of the discrete locations where each of the tests was conducted. Nevertheless, in the process of defining a two-dimensional model which seeks to reflect a reasonable seismic response, a series of adequate assumptions have to be made.

For that purpose, within the limitations of data availability and with the help of altitude information extracted from satellite images, the entire slope models are assumed to be comprised of soil layers with well-defined boundaries and constant properties throughout their areas of influence.

With the determination of the soil substructure and the topographic relief, subsequent procedures involve the generation of finite element meshes whose elements vary properly in size according to the particular soil property aimed to be characterized.

- **Seismic Response and Comprehension of the Parameters that Govern the Behavior of the Selected Slopes**

Numerous studies have dealt with the estimation of the seismic response of slopes through the application of in-plane motions in the form of vertically incoming SV-waves (e.g. Harmsen and Harding, 1981; Ohtsuki and Harumi, 1983; Assimaki et al., 2005; Bouckovalas et al., 2005). Accordingly, the finite element models corresponding to the two contrasting populated slopes generated in Chapter 4 are analyzed by means of the finite element substructure methodology described in the same chapter and subjected to the aforementioned type of bottom motion.

The dynamic behavior of slopes is considered to be a complex phenomenon resulting from the superimposition of several parameters. Therefore, it is common practice the adoption of simpler and simplified cases which introduce to the comprehension of the factors controlling the global response.

In this study, the analysis begins with the consideration of synthetic motions of complex frequency content and continues with the examination of the effect of input motions of simpler frequencies represented by Ricker wavelets.

Finally, the incorporation of additional cycles for the input motions and simplified models such as basin-shaped slopes adjacent to a rock body and homogeneous sandy slopes permitted the study of the variation of the propagating ray paths, generation of surface waves and the computation of their effect through amplification factors for each of the cases considered.

1.2 Structure of the Research.

The current work is divided into six chapters (refer to the flow chart at the end). Aside from the first and last ones, related to the Introduction and Conclusions, respectively, the content of each chapter is described as follows:

In Chapter 2, preliminary information of the areas surrounding the target slopes is presented. Brief historical background regarding the encroachment of the slopes is described. In addition, geological, geotechnical and soil vibration data is provided for the two districts where the adopted target areas are located.

Chapter 3 focuses on the passive and active surface wave techniques utilized in the estimation of shear-wave velocity profiles at selected points. Additional emphasis is placed on the field surveys carried out within the framework of this work and the dependability of the results in describing the natural period of the underlying soil.

In Chapter 4, the procedures utilized in the evaluation of the soil substructures and the topographic reliefs are summarized. Furthermore, mesh generation methodologies are discussed as well as the finite element approach adopted with attention to its advantages and drawbacks by means of numerical applications.

Chapter 5 presents the dynamic response characteristics of the two contrasting populated slopes considered. Importance is given separately to each site since the factors governing their behavior are particularly different, including the analysis of complex cases and simpler ones.

CHAPTER 1
Introduction

CHAPTER 2
Preliminary Information:
History, Geology, Geotechnics
and Soil Vibration Data

CHAPTER 3
Estimation of Shear-wave
Velocity Profiles by Surface
Wave Methods

CHAPTER 4
Dynamic and Geometrical
Idealization. Mesh Generation
and Finite Element Modeling

CHAPTER 5a
Seismic Response of a
Populated Rocky Basin-shaped
Slope (Villa El Carmen)

CHAPTER 5b
Seismic Response of a
Populated Sandy Slope (Lomo
de Corvina)

CHAPTER 6
Conclusions

Chapter 2: Preliminary Information

2.1 Preface

Preliminary information of the studied zones is presented in the current chapter. First, general details about location of the Lima Metropolitan area, with emphasis on the target zones in the districts of Independencia and Villa El Salvador, are given.

Both districts, started to be populated as a result of the migration process from the provinces towards the capital that started back in the 1950s. Nevertheless, in case of Independencia, its development is linked to, at some extend, the history of the National University of Engineering. In the other hand, the encroachment of Villa El Salvador is more related to the relatively recent democratic transition as it is considered one of the last places to be informally populated in Lima.

Additionally, geological and geotechnical information of the areas surrounding the target zones is introduced with the objective of obtaining a preparatory knowledge to be taken into consideration for further estimations of the dynamic properties and reliable two-dimensional models of the slopes under analysis. Noticeable differences can be found between these two: whereas Independencia is mostly covered by stiff alluvial-colluvial materials and rocky outcrops towards the hilltop, Villa El Salvador is almost entirely placed in a sand dune with one of the most unfavorable mechanic conditions in the entire city. Dynamic measurements, such as the information of the natural periods of the soil, are also considered in this chapter and corroborate the aforementioned information.

2.2 Location

The Lima Metropolitan Area is located in the west-central part of Peru (Fig. 2.1a) and faces the Pacific Ocean. It includes the provinces of Callao and Lima, the latter being known as the capital of the country and further divided into 43 districts. This metropolitan area has a projected population of 9 904 727 people estimated for the year 2015 (INEI, 2012) that roughly represents one third of the entire populace.

Geographically, Lima is situated along the Peruvian coastal desert, in the lowlands of the western foothills of the Central Andes. Although it initially occupied the Rimac river valley only, over the years, its borders have expanded through practically the Chillon and Lurin river valleys in a total conurbation area of approximately 2 819 km^2. Fig. 2.1b shows the divisions of the city of Lima and the two districts where our target areas are located, Independencia and Villa El Salvador.

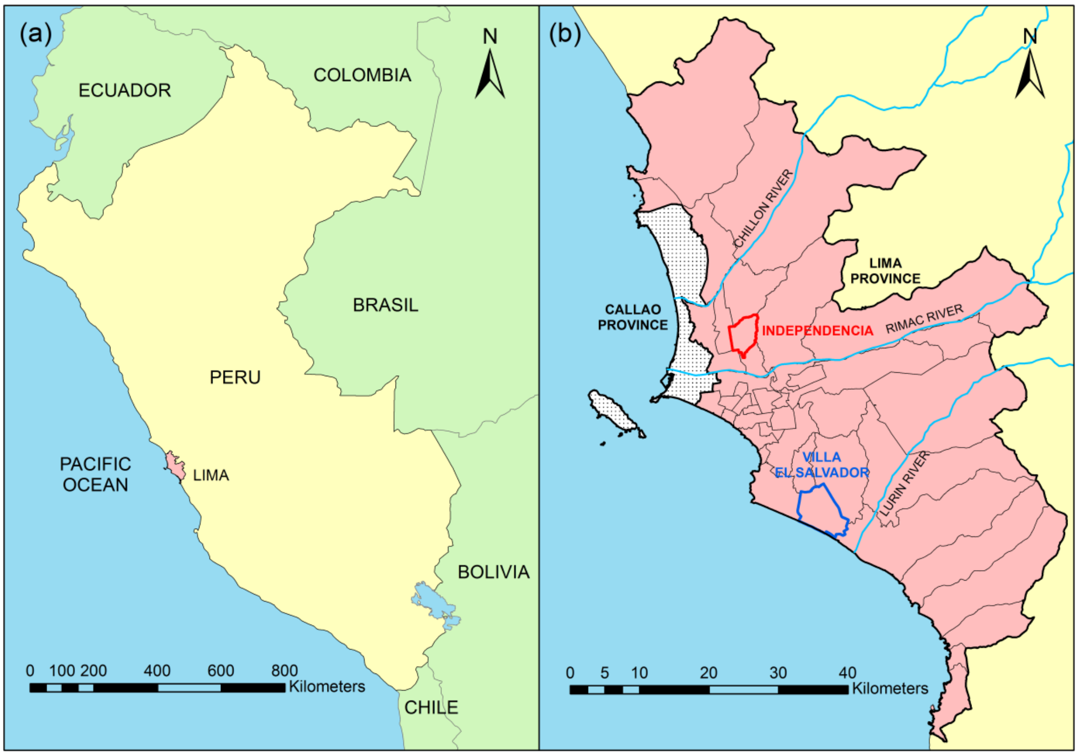

Fig. 2.1 (a) Location of Peru and the Metropolitan area of Lima. (b) Lima metropolitan area and location of the districts of Independencia (red) and Villa El Salvador (blue).

In case of the district of Independencia, it is located in the north-central part of Lima, with an estimated population of around 216 822 habitants, projected for 2015. Since its official foundation in 1964, this district has grown exponentially, which is reflected in the development of a considerable industrial zone in the west part. In total, Independencia is divided into six zones in an area of approximately 14.56.km^2.The specific region under study within this district is located in the south part in a zone called La Unificada, which in turn consists of six human settlements, being the target one located in Villa El Carmen (Fig. 2.2a).

On the other hand, Villa El Salvador is established in the south-west part of the capital, with a projected population of 463 014 people, also projected for 2015. Several proposals of urban planning and zonation have been elaborated through its relative recent history (e.g. INADUR, 1996) but have failed due to the constant change of the population distribution within the district as a consequence of continuous invasions. One of the last references can be found in Chambi, 2001 and it is used in this work. According to that, the total area of Villa El Salvador, of approximately 35.46km^2, is divided into four zones, mainly based on the main economic activity executed in a particular area.

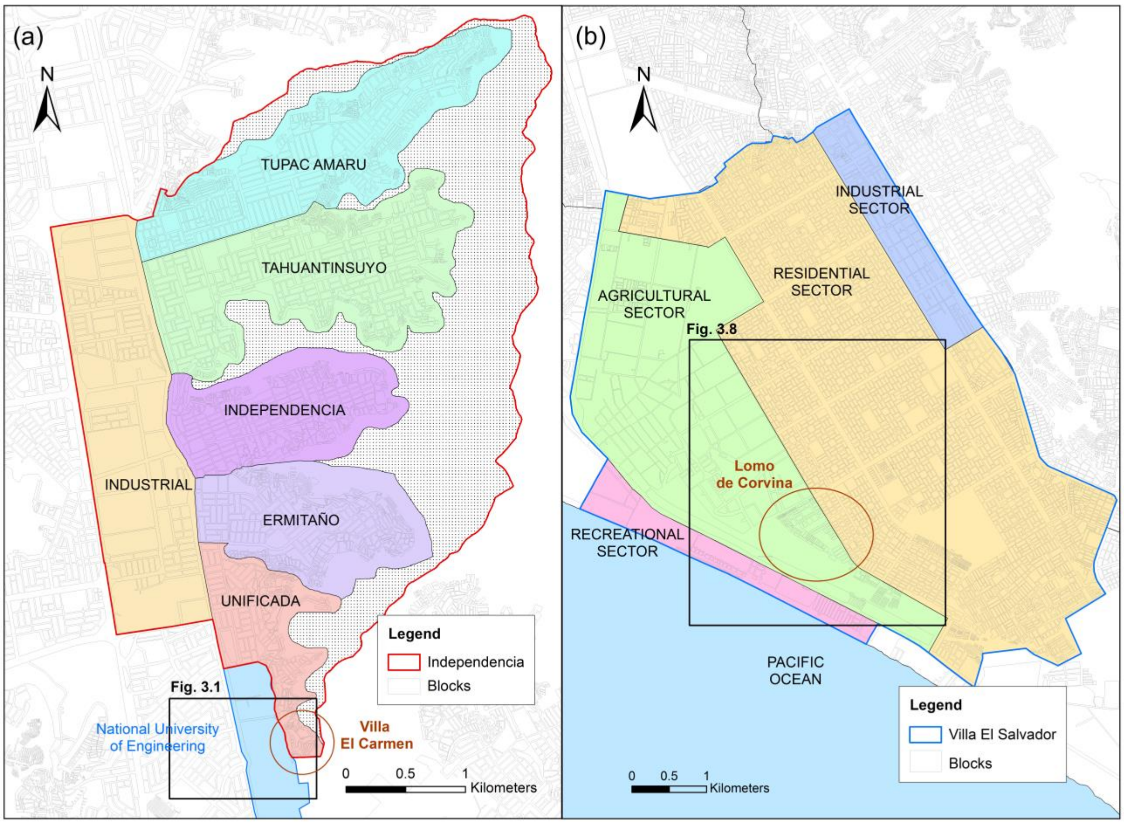

Fig. 2.2 (a) Zones in the district of Independencia, (b) Sectors in Villa El Salvador

Similar to Independencia, Villa El Salvador has developed an industrial zone, in the east part of the district, which essentially includes the mechanic, carpentry and craft sectors. The target region in this district is the sand slope called Lomo de Corvina (Fig. 2.2b) whose area, in theory, was reserved for agriculture and recreational tourism, but happened to be populated afterwards.

It is important to mention that, for the convenience of the reader, most of the figures presented in this chapter include references to the areas where complementary tests were conducted and that will be described in detail in the subsequent sections.

2.3 History

Although the urbanization process of both target areas, as the majority of the encroached places of the city, arose as a consequence of the complex mass migration with peak in the 1970s, each of them has particular characteristics and context in which they took place.

In case of Independencia, the encroachment started during the period in which the country was suffering from an economic recession period and the subsequent austerity program adopted by the Peruvian government during the late 1950s. It is in that context that a group of people, originally from El Callao, decided to invade the lands adjacent to the main pyramid of the Pre-Inca ruin called Pampa de la Cueva (Fig. 2.3a) in the southern part of the district (Stokes, 1989). At that time, this archaeological complex was surrounded by the vacant lands part of the former Aliaga agricultural estate that already has ceded a section of its land, in 1955, to the construction of the campus of the National University of Engineering, previously known as School of Civil Constructions and Mining Engineers (Lopez et al., 2012).

Specifically, Villa El Carmen, started to be populated by the employees of the National University of Engineering. After rightful claims supported by the student community, the university authorities grant the adjacent areas to 75 workers in total who settled in the low levels of the foothills on the west side of the university. The neighboring areas were taken over by a group of people from the district of Lince, constituting the human settlements known as Villa El Angel y El Milagro.

In case of Villa El Salvador, this district has one of the most recent histories compared to other encroached areas. It emerged in 1971 as one of the first planned shantytowns as a response of a land invasion implemented by a group of 200 families, that increased rapidly to 9000, occurred in the upper middle class lands in the district of Surco. This led the military regime into the decision of relocating them to the vast sandy lands in the south part of Lima (Fig. 2.3b) that, in theory, were considered as areas of future urban expansion (INADUR, 1996). Unfortunately, several proposals to regulate the urbanization of this emerging district have failed through the years due to erroneous political decisions.

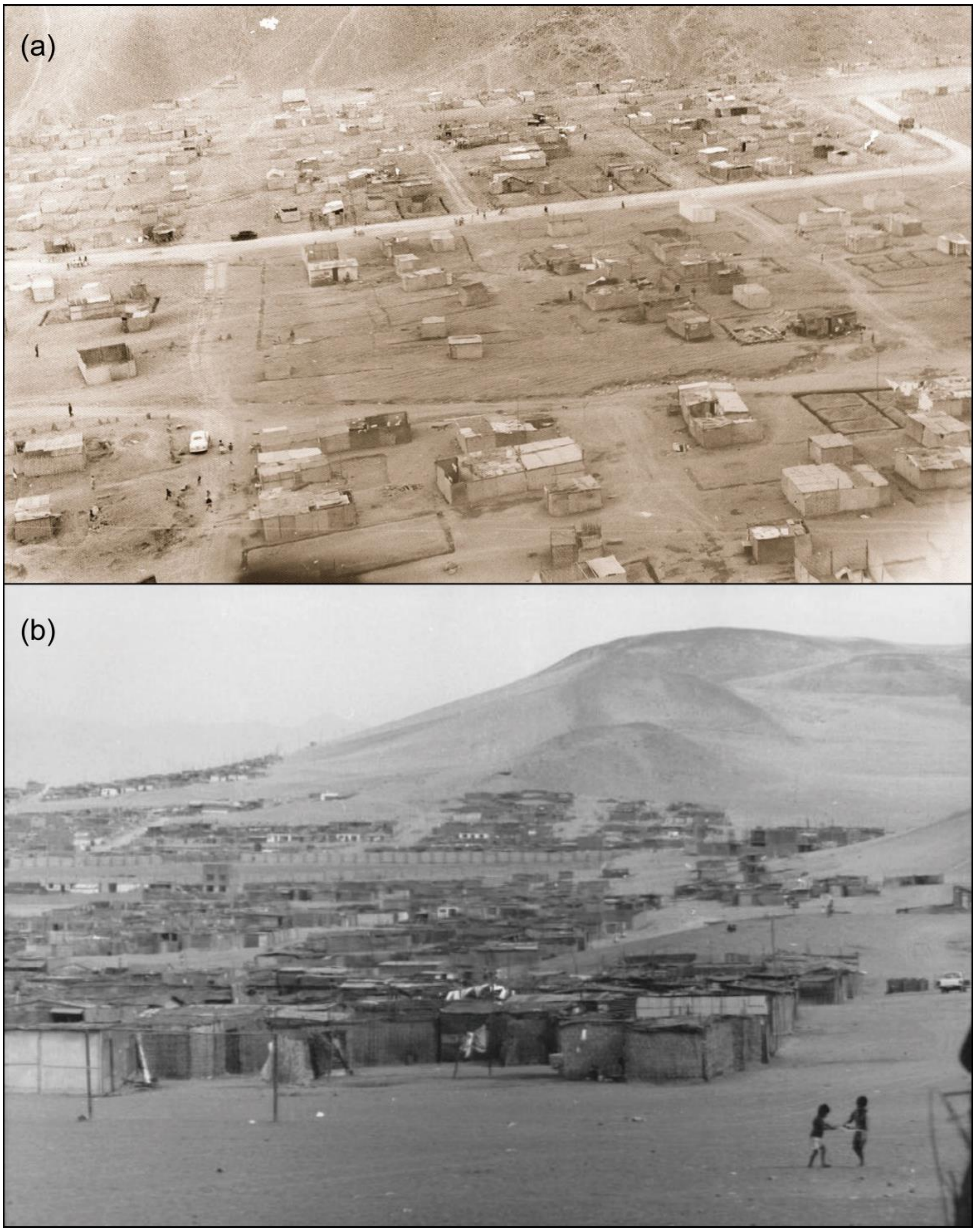

Fig. 2.3 (a) Encroachment of the Pampa de la Cueva (Independencia), (b) Invasion of the dune in the district of Villa El Salvador.

The specific case of Lomo de Corvina dates back to even more recent times. In 2002, around 198 families took possession of the eastern flank of the dune on the west side of the district (Mauricio, 2007). Originally this sector was meant to be kept as an archeological site since Pre-Inca graveyards were found there as in other parts of the district. Additional recommendations to use part of the area for the construction of a Convention Center, a museum and a university have been unsuccessful due to subsequent invasions that even led to build a separation wall at the top of the dune as a way of stopping the encroachment. More recently, the local government started to litigate with the silicon-calcareous brick company established in the seashore that was using Lomo de Corvina as a quarry weakening the slope, and demanded its progressive dismantlement (INDECI, 2014).

2.4 Geology

In general, Metropolitan Lima is located along the Peruvian coastal strip, over the alluvial fan system formed by the Chillon, Rimac and Lurin rivers and their tributaries during the Quaternary Period (Aguilar, 2005). The urbanized areas are also built over the westernmost hills of the western range of the Central Andes with slopes from moderate to steep (Fig. 2.4) which belong to a variety of geological groups with diverse origin. Therefore, aspects of local geology have to be included in order to describe in detail the target areas for this study.

The areas surrounding Villa El Carmen in the district of Independencia (Fig. 2.5) are mostly covered by alluvial soil deposits and rock formations of different ages (CISMID, 2013a):

- **Pleistocene Alluvial Deposits (Qp-al):** The lithology of these Pleistocene deposits is comprised of conglomerate, containing clasts of different types and rocks especially intrusive and volcanic, sub-rounded gravels, sands of diverse granulometry and lower portions of silt and clay.
- **Recent Alluvial Deposits (Qh-al):** Mainly composed of clasts and sub-angular gravels with a well-selected sand matrix in some cases. Due to their stony nature, these materials provide unfavorable conditions for agriculture.
- **Cerro Blanco Formation (Ki-cb):** It mainly consists of sedimentary rocks on the bottom part and volcanic rocks at the top. Its lithology corresponds to light gray feldspar sandstones with pyroclastic origin and intercalations of aphanitic andesites.

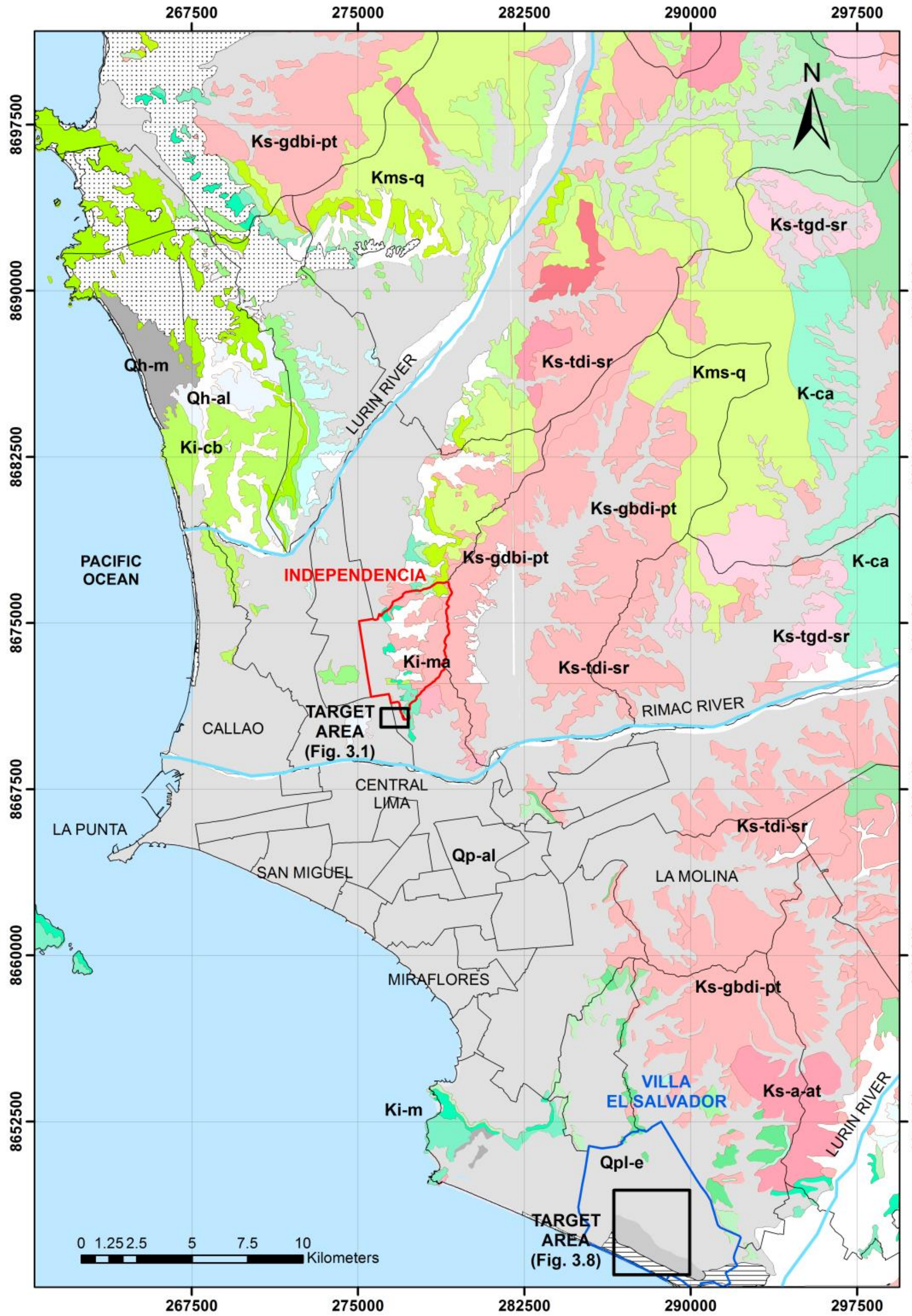

Fig. 2.4 Geological map of Metropolitan Lima.(Palacios et al., 1992)

- **Herradura Formation (Ki-he):** Consists of two geological members, La Virgen and Herradura, but in this case, due to its proximity to the Marcavilca formation, it is referred to the latter one. It is made of quartz sandstones, with partial yellowish-greenish tone and finely stratified, followed by gray to black lutite that changes to reddish brown when weathered. Finally, in the transition to the Marcavilca formation, it contains dark gray limestones

- **Marcavila Formation (Ki-ma):** It is composed of three geological members, Morro Solar, Marcavilca and La Chira, but since the target zone represents the transition from the previous formation, it is undoubtedly the first one. At the base of this member, it presents a gradual change from the clayey facies (Herradura formation) to the sandstone facies (Marcavilca formation), followed by sandstone horizons with variable proportions of lutite that provokes a change in color from dark tone on the bottom part to reddish at the top, where the transition to quartzite starts.

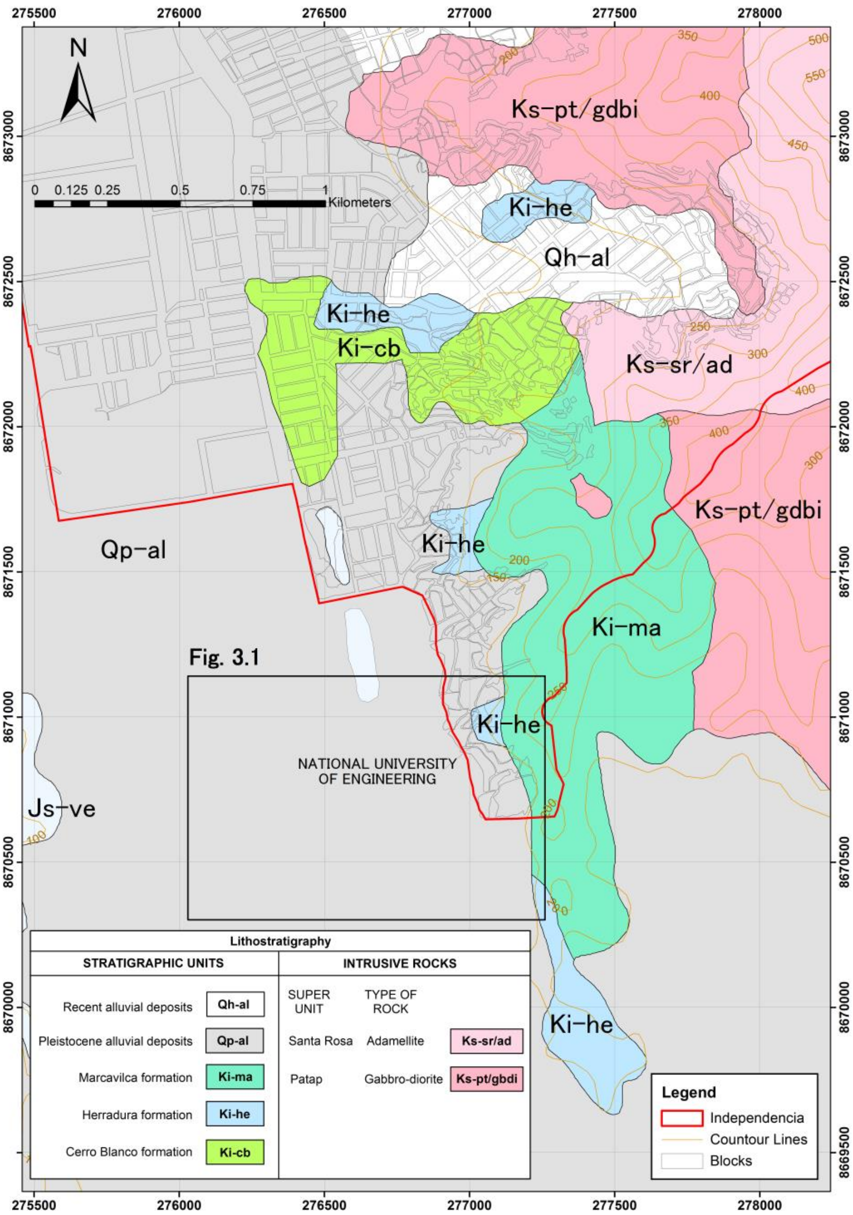

Fig. 2.5 Geological map of the area under study in Villa El Carmen (CISMID, 2013a)

- **Patap Superunit (Ks-ps/gdbi):** It is made up of gabbro and diorites, the oldest from the batholite, belonging to the Upper Cretaceous. Their characteristic dark tone is because of the magnesia content. Their textures vary from medium to coarse grain and possess a high specific weight due to the biotite and hornblende contained.
- **Santa Rosa Superunit (Ks-sr/ad):** This unit is composed of adamellitic bodies which are typically found disturbed, with signs of instability.

Regarding the area of study in Villa El Salvador, the following geological formations (Fig. 2.6) are found (Palacios et al., 1992):

- **Pleistocene Eolian Deposits (Qpl-e):** These deposits are composed of ancient eolian accumulations that are currently stabilized conforming sandy slopes and hills. In the past, these regions should have had the structure of dunes that might have been changed as a result of stabilization processes, such as humidity or growing vegetation, so in general they are found as extensive sandy areas of smooth shape.
- **Recent (Holocene) Eolian Deposits (Qh-e):** Mainly composed of shifting sands widely propagated in the area of study. These sands come from the winds blowing along the seashore and ended up being deposited in the form of mantles and dunes. In case of the latter ones, they can be found lying over sand mantles or rocky bodies, either in a crescentic shape or longitudinally arranged.
- **Recent (Holocene) Marine Deposits (Qh-m):** They extend into narrow strips of land (30-100m) made of sands, silts and clasts carried by the effects of the ocean currents to the seashore. In more detail, these deposits mainly contain medium to fine-grain sands, with characteristic yellowish-grey tone and variable amounts of quartz, micas and mafic particles. In a lesser proportion, they present light gray unconsolidated silts with remains of seashells.

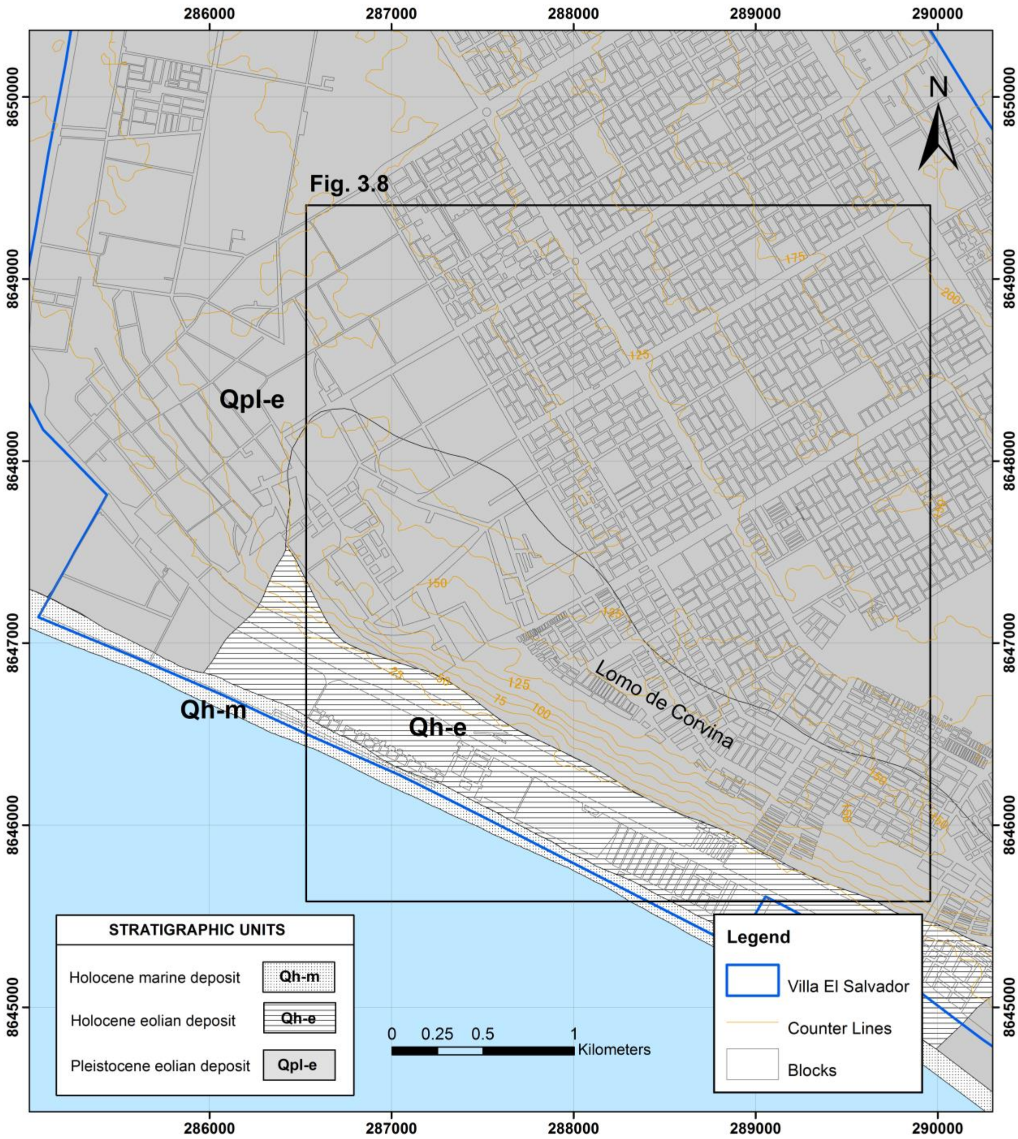

Fig. 2.6 Geological map of the area of study in Lomo de Corvina (Palacios et al., 1992)

2.5 Geotechnics and Dynamic Behavior

In general, the areas corresponding to Metropolitan Lima are located on the alluvial fan of the Rimac basin, and some sectors of the Chillon and Lurin basins, which mostly consist on alluvial gravels with good geomechanical behavior, surrounded by rock formations and weathered colluvial gravels (Fig. 2.7). However, there are urbanized areas built over places with particular characteristics, such as highly compressible swampy soils, poor-graded eolian sand deposits of variable thickness in the extremes of the city and soft clay and organic soils close to the Port of Callao (CISMID, 2005).

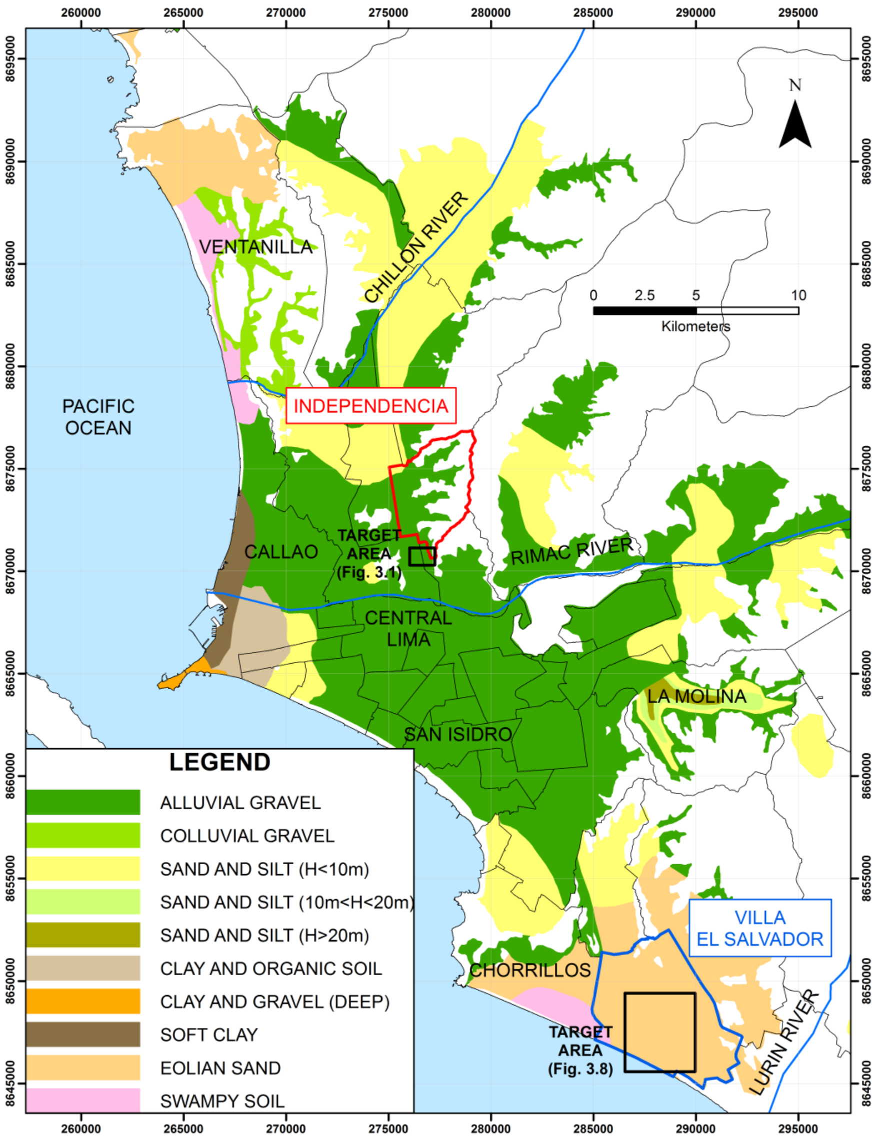

Fig. 2.7 Soil map of the city of Lima. (CISMID, 2005)

In case of the district of Independencia, new soil data were collected and additional tests were conducted (CISMID, 2013) in order to obtain a more precise characterization of the underlying material. Regarding the mechanical behavior, the analysis of soil pits allowed the identification of two different types of materials. The first one corresponds to rocky outcrops and alluvial gravel deposits, sub-rounded in the flat areas and sub-angular in the sloping zones, which can be found on the surface or at very shallow depths below medium compact to dense sandy layers. The second soil classification comprises medium compact to dense sand deposits with thickness of more than 3m and, to a lesser extent, thin layers of clays and silts of medium stiffness.

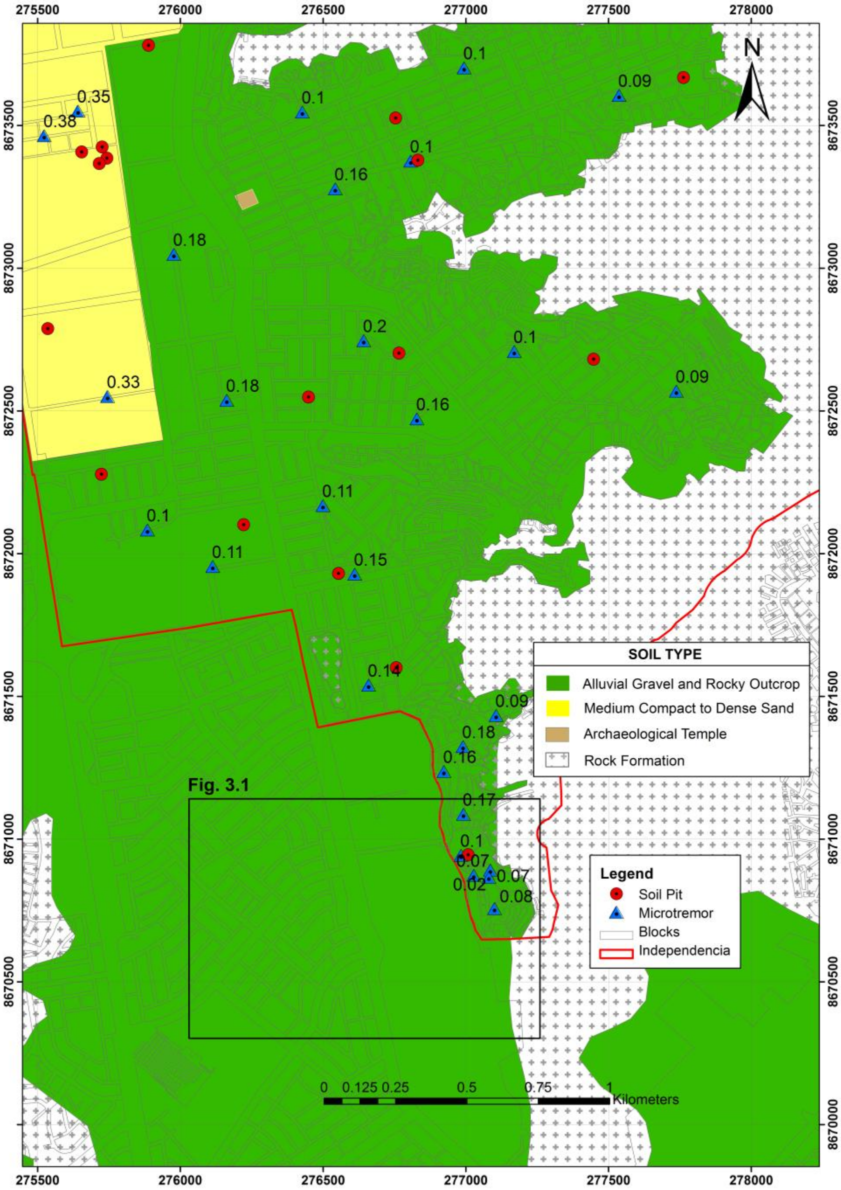

Fig. 2.8 Soil map, soil pit location and microtremor results for Villa El Carmen (CISMID, 2013a)

Concerning the dynamic characteristics, the analysis of single point microtremor measurements permitted the study of the variation of the natural period of the soil throughout the district. Values of less than 0.1s can be found in the vicinity of rock formations and are either associated to surficial gravels that overly stiffer materials or tests carried out directly on the outcrops. Period values increase while moving away from the foothills and vary within the range of 0.1s and 0.3s for dense gravels and sands to finally reach higher periods in the zones corresponding to thick sand deposits, as expected from the geotechnical classification. The above results can be observed, for the particular zone under study, in Fig. 2.8.

Similar updating study was conducted in the district of Villa El Salvador (CISMID, 2011). The analysis of soil pits, standard penetration tests (SPT) and visual inspections allowed the grouping of the underlying material into three categories. The first type includes the shallowly fractured rocky outcrops from the Pamplona Formation located in specific zones throughout the district with a matrix of silty sands. The second and third categories are comprised of deposits of eolian sands. The stratigraphic profiles of these areas indicate that a shallow layer of backfill soil with a thickness within the range of 0.3m-1m, that at some places reaches 2.5m, overlies these deposits. The main property of these sands is that their apparent density, given by the standard penetration resistance or N-value, rapidly increments, getting to values of more than 50 at a depth of 5m in average.

It is important to highlight that the Peruvian Building Code requires that areas which might be susceptible to liquefaction, slope stability and seismic amplification effects be given special treatment. Therefore, the soils in Lomo de Corvina and along the seashore were regarded as a different type although their mechanical properties do not differ so much from those in the rest of the district.

With respect to the dynamic properties, both Multichannel Analysis of Surface Waves (MASW) tests and single point microtremor measurements were collected and conducted (CISMID, 2011). The first set of tests allowed the exploration up to an average of 25m of depth and a shear-wave velocity of 500m/s. In case of the natural period of the soil, a wide range of values was identified. Low periods correspond only to the surroundings of the fractured rocky outcrops in limited places in the district, while higher values correlate with thick sand deposits that increment towards the sandy slope in Lomo de Corvina where they reach a maximum value of 1.2s.

The above information can be consulted, in the neighborhood of the analyzed slope, in Fig. 2.9.

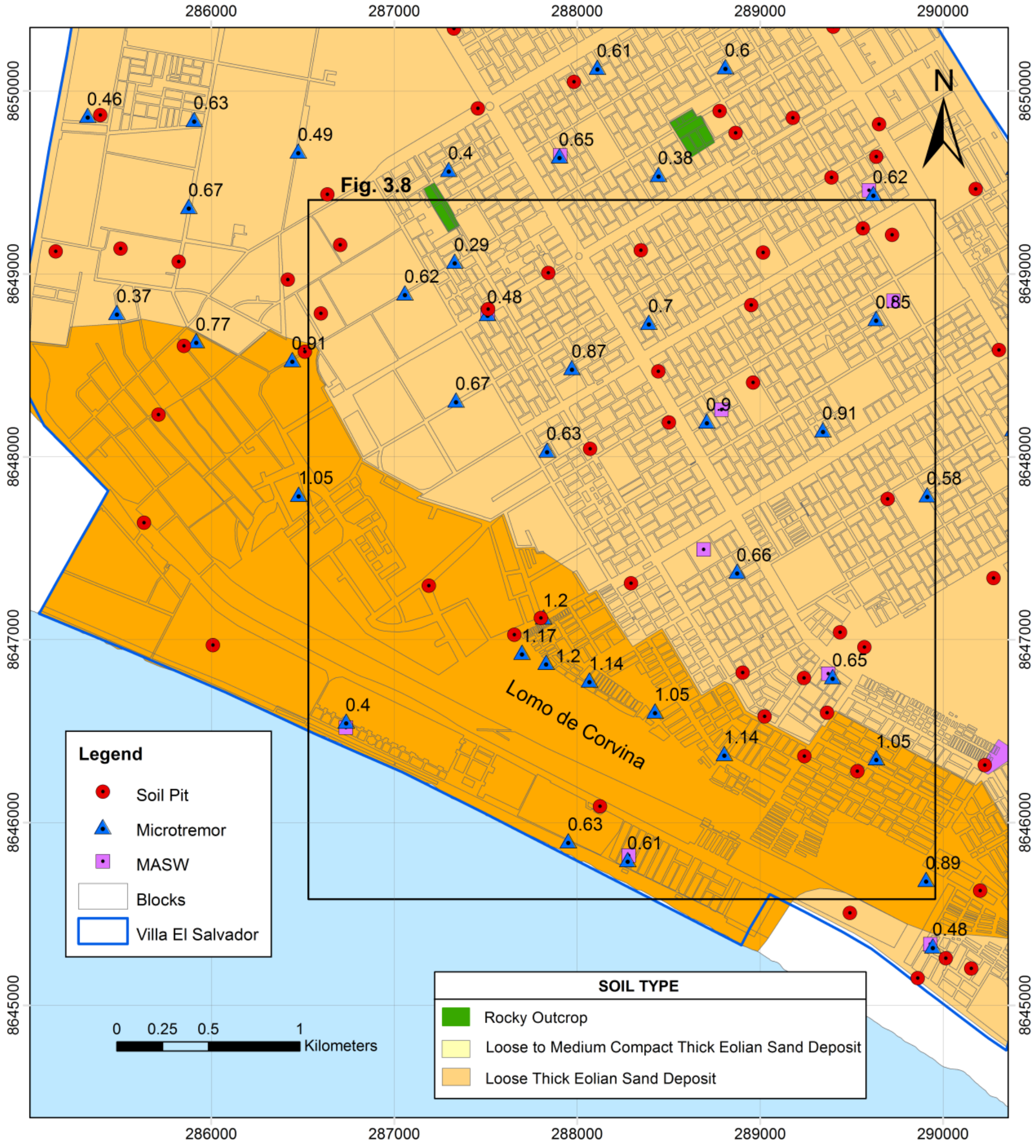

Fig. 2.9 Soil map, location of soil pits and MASW tests and natural period values in the surroundings of Lomo de Corvina (CISMID, 2011)

Chapter 3: Estimation of Shear-wave Velocity Profiles using Surface Wave Methods

3.1 Preface

This chapter schematically describes the general procedures adopted in the estimation of shear-wave velocity profiles at conveniently selected locations in the areas under study.

Overall, passive and active surface-wave methods were utilized in the representation of the dispersive characteristic of the underground structure in Villa El Carmen (Independencia) and Lomo de Corvina (Villa El Salvador), respectively, and, therefore, the distribution of the contents in the following sections was done based on that difference.

The first part of this chapter focuses on the microtremor campaign carried out at seven places in the flat and sloping areas of Villa El Carmen (Gonzales et al., 2014a). On the one hand, linear arrays, with varying sensor spacing distances, were conducted for the estimation of the shallowest part of the soil profile, whereas in the other hand, circular arrays, with varying radius, allowed the recording of longer wavelengths and the exploration to greater depths. The applicability of this type of tests in a ground with irregularities has been investigated by Nakagawa and Nakai (2008) and Nakai and Nakagawa (2009) through the study of Rayleigh wave propagation in a non-horizontally layered medium. They concluded that the influence of body and high-mode Rayleigh waves generated due to the irregularity is considerable only in the vicinity of the natural frequency of the vibrating soil system and, therefore, negligible for the rest of the wide frequency range of interest.

The second half of this chapter centers on the field survey in Lomo de Corvina. In this case, due to the limited availability of free spaces to conduct large circular arrays in this overcrowded area, only multichannel analysis of surface waves (MASW) tests were performed including the sloping parts and the seashore. These five tests were conducted in the transverse direction to the line under consideration in order to avoid unfavorable topographic variations. Reliability of the obtained shear-wave velocity profiles was ensured through the comparison with the H/V spectra of single point microtremor measurements. Nevertheless, unlike the profiles in Villa El Carmen, the assumption of a deep structure similar to a previously conducted test was required, in order to be able to represent the characteristic long natural periods in this area.

3.2 Villa El Carmen (Independencia)

The estimation of the soil substructure in the flat and sloping areas in Villa El Carmen was performed by means of a combination of the results of widespread passive surface-wave techniques, single point microtremor measurements and information of a deep shear-wave velocity profile previously conducted nearby.

3.2.1 Passive Surface-wave Techniques

The use of microtremors (also referred to as ambient noise, microseisms, etc.) has become a very efficient tool in the inference of soil subsurface structures. Recordings of this type of low amplitude vibrations, generated from a variety of sources, and their subsequent processing, are capable to reproduce dispersive characteristics by the identification of the phase velocity of surface waves. Most techniques make use of arrays of N vertical-component sensors placed in the vertices of a polygon in which, depending of the adopted methodology, the use of an additional sensor in the center is also required.

The applicability of microtremor arrays in urban areas, and their comparative performance with other geophysical tests, has been widely studied (Horike, 1985; Matsushima et al., 1992; Gabas et al. 2014; Bard et al., 2014). Particularly, Calderon et al. (2011, 2012a, 2013), Quispe et al. (2014) and Yamanaka et al. (2016) demonstrated the efficiency of the implementation of this kind of measurements in the extraction of reliable shear-wave velocity profiles that, in turn, allowed the adequate characterization of the seismic response and site effects in the cities of Lima and Tacna, in southern Peru.

The most popular techniques employed in the processing of microtremor data and the extraction of phase velocities are the high resolution frequency-wavenumber (F-k) method (Capon, 1969), that makes use of arrays of arbitrary shape, and the spectral autocorrelation (SPAC) method (Aki, 1957), that utilizes arrays deployed in an inscribed polygon in a circle. In recent times, two new approaches, applied to circular arrays and that permit the exploration of subsurface structures for longer wavelengths, were derived by the generalization of the SPAC method. These are known as the centerless circular array (CCA) analysis (Cho et al., 2004) and the noise-compensated centerless circular array (nc-CCA) analysis (Tada et al., 2007).

a) High Resolution Frequency-Wavenumber (F-k) Method

In general, a typical microtremor wave field can be considered as a stochastic process and consists of plane waves propagating horizontally. Then, according to Capon (1969), the stochastic process $u_{(t,\mathbf{r})}$ has an autocorrelation function which depends on time t and on the location vector $\mathbf{r}_{(x,y)}$ that is expressed as

$$R_{(\tau,\mathbf{d})} = \lim_{T,S\to\infty} \int_{-T/2}^{T/2} \int_{S} u_{(t,\mathbf{r})} . u_{(t+\tau,\mathbf{r}+\mathbf{d})} dt d\mathbf{r} \tag{3.1}$$

The above autocorrelation is Fourier-transformed with respect to time and space obtaining the frequency-wavenumber (F-k) spectrum

$$P_{(f,\mathbf{k})} = \int_{-\infty}^{+\infty} \int_{-\infty}^{+\infty} R_{(\tau,\mathbf{d})} e^{-j(2\pi f\tau + \boldsymbol{kd})} d\tau d\mathbf{d} = \int_{-\infty}^{+\infty} S_{(f,\mathbf{d})} e^{-j\mathbf{kd}} d\mathbf{d} \tag{3.2}$$

where f and $\mathbf{k}$ are frequency and wavenumber, respectively. The following expression applies

$$\mathbf{kd} = k_x x + k_y y \tag{3.3}$$

We assume microtremors observed at N stations. Then, the F-k spectrum can be expressed as

$$\hat{P}_{(f,\mathbf{k})} = \sum_{i=1}^{N} \sum_{j=1}^{N} S_{ij}(f)\, e^{-j\mathbf{k}(r_i - r_j)} \tag{3.4}$$

where $S_{ij}(f)$ is the coherency of records at sites i and j defined as

$$S_{ij}(f) = \frac{C_{ij}(f)}{\sqrt{C_{ii}(f) C_{jj}(f)}} \tag{3.5}$$

where $C_{ij}(f)$ is the cross spectrum for those stations. Then

$$S_{(f,\mathbf{k})} = E^*_{(\mathbf{k})} S_{(f)} E_{(\mathbf{k})} \tag{3.6}$$

where $S_{(f)}$ is the matrix whose elements are the coherency values and * denotes complex conjugate. $E_{(\mathbf{k})}$ is

$$E_{(\mathbf{k})} = [\exp(i\mathbf{kr_1}) \ \ \dots \ \ \exp(i\mathbf{kr_n})]^T \tag{3.7}$$

and determined only from relative station spacing of the array.

In this method, the phase velocity of the most dominant wave in the F-k spectrum is sought. Therefore, from the wave number vector $\mathbf{k_0}$, which is drawn at the peak of the F-k spectrum in wave number coordinates (k_{x0}, k_{y0}) for frequency f_0 (or period T_0), the phase velocity c_0 can be obtained as

$$c_0 = \frac{2\pi f_0}{|\mathbf{k_0}|} = \frac{2\pi}{T_0\sqrt{k_{x0}^2 + k_{y0}^2}} \tag{3.8}$$

b) Spatial Autocorrelation (SPAC) Method

The Spatial Autocorrelation method (SPAC) is based on the theory developed by Aki (1957) to determine the relationship between the temporal and spatial spectra of seismic waves, when the distribution of wavenumber vectors is complicated for phase analysis.

Theoretically, the SPAC method requires an array with multiple sensors deployed in a circumference. Theory demonstrates that the spatial autocorrelation coefficient in microtremor data observed by a circular array is a function of the frequency, phase velocity and the radius of the array.

The spatial autocorrelation (SPAC) function is defined as

$$C_{(x,r,\omega)} = \frac{1}{T} E\left[u_{(x,\omega,t)} . u_{(x+r,\omega,t)}\right] \tag{3.9}$$

This function, in polar coordinates, is averaged in azimuth

$$R_{(r,\omega)} = \frac{1}{2\pi}\int_0^{2\pi} C_{(r,\theta,\omega)} d\theta \tag{3.10}$$

The spatial autocorrelation (SPAC) coefficient is

$$\rho_{(r,\omega)} = \frac{R_{(r,\omega)}}{C_{(0,0,\omega)}} \tag{3.11}$$

For surface-wave propagation, the SPAC coefficient is expressed using the zero-order Bessel function of the first kind

$$\rho_{(r,\omega)} = J_0\left(\frac{\omega r}{c_{(\omega)}}\right) \tag{3.12}$$

The above coefficient is uniquely defined for a certain geometry and allows the estimation of the phase velocity, $c_{(\omega)}$, for frequency ω, from microtremor data recorded in a circular array of radius r.

c) Centerless Circular Array (CCA) and Noise-compensated Centerless Circular Array (nc-CCA) Methods

Cho et al. (2004) reformulated the general theory of microtremors obtained using circular arrays and developed the CCA method. Suppose we record the vertical component of N sensors equidistantly deployed on a circumference of radius r. The record at time t in the jth sensor is denoted as $d_j(t)$. Therefore, the waveform representing the directional averaging can be obtained from the records of each sensor as follows

$$d_{ave}(t) = \frac{1}{N}\sum_{j=1}^{N} d_j(t) \tag{3.13}$$

In order to derive the complex waveform, the weight of $\exp(i\theta)$ is added, where i is the imaginary unit and θ is the azimuth of the sensor

$$d_{wave}(t) = \frac{1}{N}\sum_{j=1}^{N} d_j(t)exp\left(\frac{2\pi i(j-1)}{N}\right) \tag{3.14}$$

The power spectral density functions of the above equations are calculated and the correspondent spectral ratio will be denoted as ρ_{cca} that, for each frequency, is associated to the wavenumber of Rayleigh waves as

$$\rho_{cca} = \frac{\sum_{l=0}^{M} \alpha_l J_0^2(rk_l) + \varepsilon/N}{\sum_{l=0}^{M} \alpha_l J_1^2(rk_l) + \varepsilon/N} \tag{3.15}$$

where $J_m(.)$ is the mth order Bessel function of the first kind, k_l is the wavenumber of the lth mode of Rayleigh waves, α_l is the power partition ratio of the lth mode to the total power of the Rayleigh waves, M is an order of the maximum mode for Rayleigh waves that exists in the wavefield (the fundamental mode is counted as 0th), and ε is the noise-to-signal (NS) ratio.

The following equation is obtained when a single mode is exceed, by setting $M = 0$

$$\rho_{cca} = \frac{J_0^2(rk) + \varepsilon/N}{J_1^2(rk) + \varepsilon/N} \equiv g(rk, \varepsilon, N) \tag{3.16}$$

The CCA method makes use of the ideal situation of $\varepsilon = 0$. Then

$$\rho_{cca} = \frac{J_0^2(rk)}{J_1^2(rk)} = g(rk, 0, N) \tag{3.17}$$

After replacing an observed value of ρ_{cca} in the above expression, it is possible to retrieve rk by means of an inverse analysis. Since r is known, phase velocity, c, for frequency f, can be estimated from $c = 2\pi fr/rk$. It is important to note that Eq. (3.17) holds in noise-free situations only. Therefore, there might be an overestimation of the value of rk, and thus an underestimation of the phase velocity, in long-wavelength ranges (small rk). For this reason, in the implementation of the CCA approach in real measurements, it is important to check that the observed NS ratio lies within the limits proposed by the method.

The formulation of the nc-CCA method was developed to eliminate the effect of noise in the calculation by adding a central sensor (Tada et al., 2007). In this method, the phase velocity is obtained by the adoption of the long-wavelength approximation of the Bessel function in Eq. (3.16), assuming that the wavelength is sufficiently longer than the radius of the array, r

$$c = \pi f r \sqrt{\frac{2 + \rho_{cca}}{1 + \frac{\varepsilon}{N} + \frac{\varepsilon \rho_{cca}}{N}}} \tag{3.18}$$

The estimation of the NS ratio, ε, is required and obtained from

$$\varepsilon = \frac{-B - \sqrt{B^2 - 4AC}}{2A} \tag{3.19}$$

$$\begin{cases} A = -\rho^2 \\ B = \dfrac{\rho^2}{coh^2} - 2\rho^2 - \dfrac{1}{N} \\ C = \rho^2 \left(\dfrac{1}{coh^2} - 1\right) \end{cases}$$

where coh^2 is the squared coherence between $d_{ave}(t)$ and the central point and ρ represents the SPAC coefficient in Aki (1957).

3.2.2 Microtremor Measurement Campaign

With the aim of evaluating the dynamic properties of the soil along the two-dimensional profile under study in Villa El Carmen (line A-A'), seven ambient vibration (microtremor) array measurements were carried out in places covering the flat and sloping areas of the foothill. Location of the tests and specific geographic coordinates can be observed in Fig. 3.1 and Table 3.1, respectively, where P stands for arrays conducted on the flat level and S for those along the slope.

The sensors employed in the observation of the vertical component of microtremors were the moving-coil velocimeters model CR 435-1S with a natural period of one second. The acquisition system utilized was the GEODAS 15HS portable logger, manufactured by Anet Co., Ltd. This system has the capability to set the sampling frequency at different values depending on the soil conditions encountered and the nature of the recorded waves.

The general geometrical arrangement consisted of six sensors placed on the vertices of a regular pentagon inscribed to a circumference and its center (Fig. 3.2a). Microtremor measurements were carried out for suitable combinations of varying radius and sampling frequencies that permit the recording of surface waves with longer wavelength, and therefore, the soil exploration at greater depths. Array size was constrained by the availability of open spaces, such as parks, soccer fields, etc. Consequently, circular arrays with a maximum radius of 30m were carried out in the flat areas, whereas in the sloping part, due to absence of open spaces, only miniature circular arrays were accomplished. Details of the array dimensions can be consulted in Table 3.2.

In the other hand, the analysis of the shallow substructure was conducted by means of additional recordings of the vertical components of surface waves generated by an active source (Fig. 3.2b). In this case, linear arrays with sensor spacing of 0.5m and 2m, and with a suitable high sampling frequency, recorded the vertical motion generated by human hops performed at distances conveniently far from one of the extremes to avoid signal saturation.

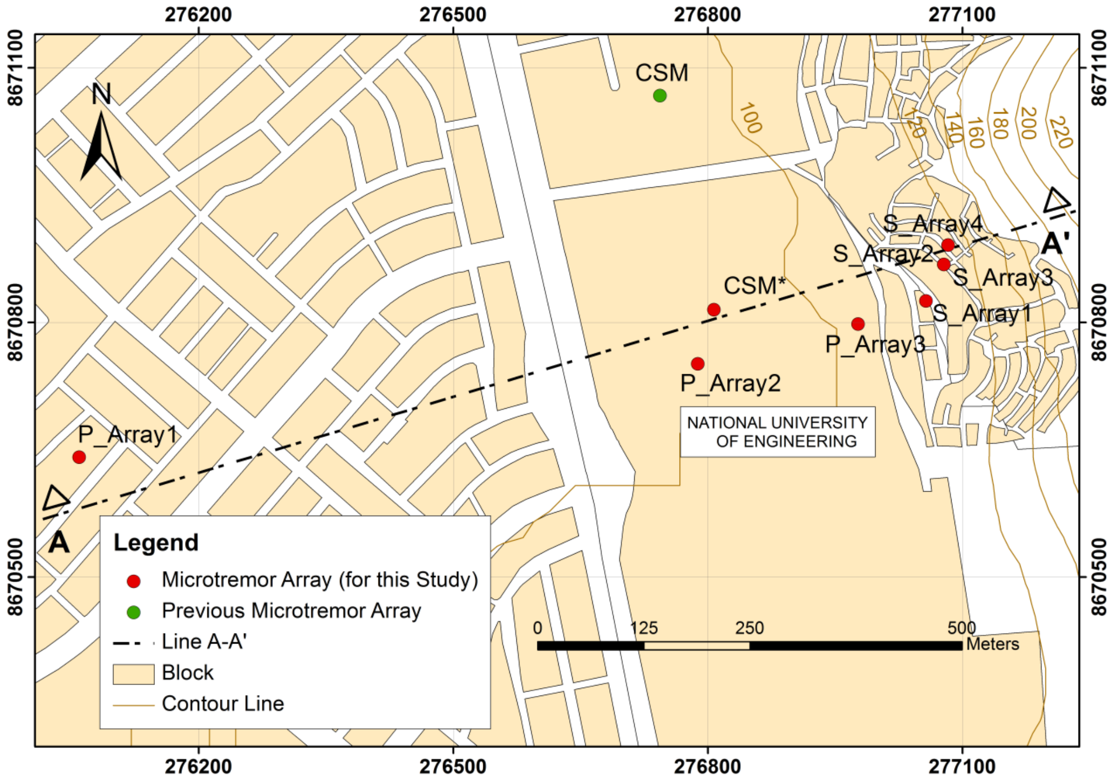

Fig. 3.1 Location of conducted microtremor arrays in Villa El Carmen

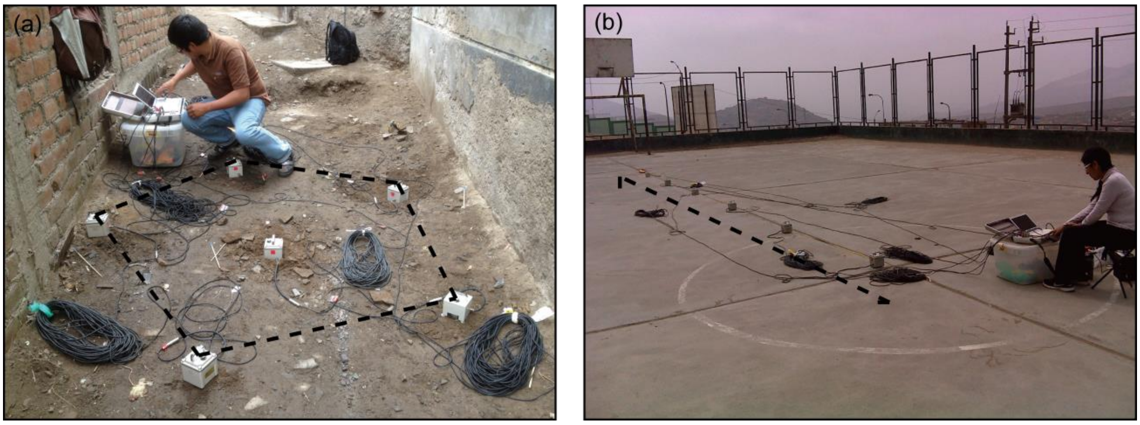

Fig. 3.2 (a) Microtremor circular array, (b) Microtremor linear array

Table 3.1 Geographical coordinates of the geophysical tests considered for Villa El Carmen

Test ID	**Latitude**	**Longitude**
P_Array1	-12.017799^{o}	-77.056893^{o}
P_Array2	-12.016854^{o}	-77.050192^{o}
P_Array3	-12.016442^{o}	-77.048454^{o}
S_Array1	-12.016203^{o}	-77.047718^{o}
S_Array2	-12.015816^{o}	-77.047522^{o}
S_Array3	-12.015844^{o}	-77.047490^{o}
S_Array4	-12.015608^{o}	-77.047474^{o}
CSM	-12.013995^{o}	-77.050580^{o}

Table 3.2 Array dimensions and processing methods

Test ID	**Dimension (m)**							
	Linear Sensor spacing		**Circular** Radius					
	0.5	**2.0**	**1**	**2.5**	**4**	**5 ~ 9**	**10 ~ 20**	**20 ~ 30**
P_Array1	○	○	○			Δ ◊	□	□
P_Array2	○	○				○ □	○ □ ◊	
P_Array3	○	○				Δ	□	○ ◊
S_Array1	○	○			○ ◊	○ ◊		
S_Array2	○	○	◊	◊				
S_Array3	○	○		Δ ◊				
S_Array4	○	○						

○ : Frequency-wavenumber (F-k) spectral method

□ : Spectral Autocorrelation (SPAC) method

Δ : Centerless Circular Array (CCA) method

◊ : Noise-compensated Centerless Circular Array (nc-CCA) method

3.2.3 Estimation of Shear-wave Velocity Profiles

Information regarding the extraction of reliable dispersion curves from microtremor data, the inversion procedure utilized and the final estimation of shear-wave velocity profiles at the selected seven places in Villa El Carmen will be explained in the following sections.

a) Dispersion Curves

Data obtained from recordings of the vertical component of microtremors were processed by means of the methods described in Section 3.2.1 in order to obtain dispersion curves at each site.

It is important to highlight that each of these processing methods has particular criteria to be fulfilled before considering the extracted dispersive information as reliable and representative for the soil substructure under consideration. Among these criteria, the most frequently used are: modal analysis, coherence values, peak spectral values and NS ratio. The final list of methods successfully applied to the conducted microtremor arrays can be found in Table 3.2.

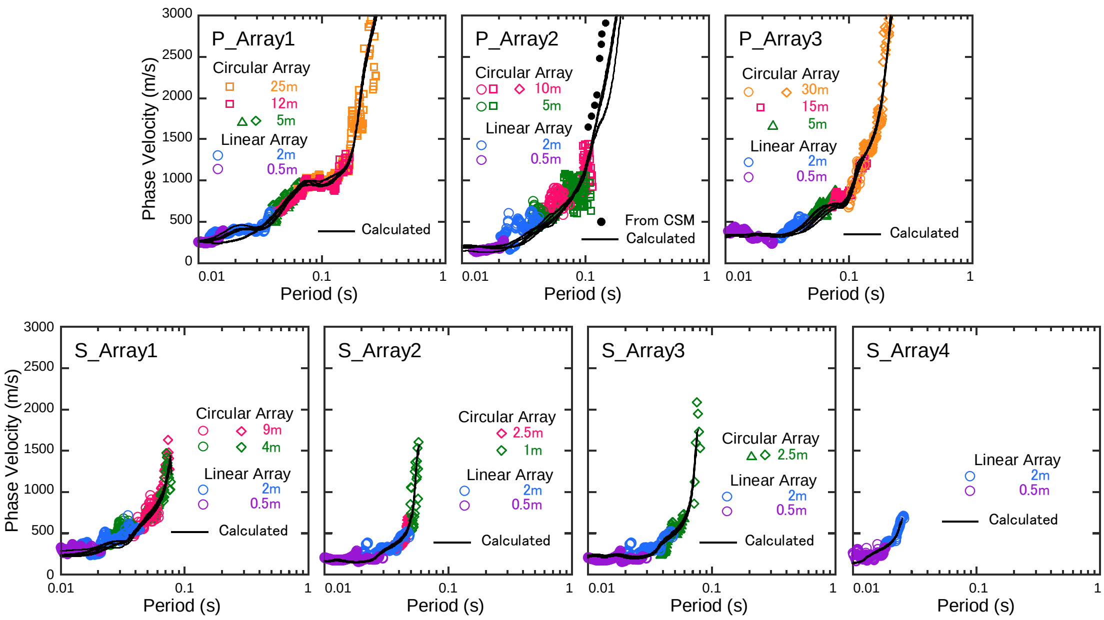

○: F-k method □: SPAC method Δ: CCA method ◊: nc-CCA method

Fig 3.3 Observed (from array measurements) and calculated (from GA) dispersion curves.

Fig. 3.3 shows the extracted dispersion curves at each site, in which the overlapping of partial curves obtained from different methods gives an evidence of their correct application. As it can be seen, a general rule of the applicability of a given method to a certain array size cannot be made. However, it can be stated that both CCA and nc-CCA methods are able to extract information for longer wavelengths in comparison with the conventional ones, in addition to the fact that, in all cases, linear arrays of varying sensor spacing are suitable to define the initial trend of the dispersive characteristics and, therefore, to accurately estimate the very shallow part of the soil profile in places where the space is very limited, such as in S_Array4.

b) Inversion Analysis – Genetic Algorithms (GA)

After the adequate extraction of dispersion curves from surface-wave tests, the next step in the accurate determination of their respective shear-wave velocity substructure involves a set of process called inversion analysis.

It is known that, in general, a typical dispersion curve is derived from a nonlinear formulation associated to particular properties of each of the layers forming the soil profile, such as shear- and compressional-wave velocities, density and thickness. Therefore, it is common practice to use a linearized approximation involving the above parameters, such as the least-squares method widely applied to MASW tests, as explained later in this chapter.

The problem with these linearized approaches is that the solution may fall into an erroneous local minimum due to their strong dependency on the initial adopted profile and hence, their use is limited to cases in which previous information of the soil is available or adequate initial assumptions can be made.

The nonlinear optimization method known as Genetic Algorithms (GA) (Goldberg, 1989) intended to overcome this difficulty and its application in the field of geophysics has been widely certified (Yamanaka and Ishida, 1996, Dal Moro et al., 2006). Overall, the method makes use of random processes that explore regions where the solution is most likely to be found in a way analogous to the evolutionary development of biological systems in nature.

In the surface-wave dispersion problem, it is necessary to define areas within which the solution would be located. This is called the search space and it is commonly assumed that only includes the shear-wave velocity and thickness of each layer, since the effect of compressional-wave velocity and density can be neglected due to their low influence in the calculation of dispersion curves (Xia et al., 1999).

By means of random numbers, an initial population of Q different models is generated. Typically, three genetic operations are consecutively applied through generations in order to produce future populations with the same size that adapt in a better way to the input conditions. These operations are: selection, crossover and mutation.

In the first operation, a new population is generated based on the value of a fitness function for each individual. A misfit function for the jth model is represented by

$$\Phi_j = \frac{1}{N}\sum_{i=1}^{N}\left[\frac{C_0(T_i) - C_c(T_i)}{\sigma(T_i)}\right]^2 \tag{3.20}$$

where N is the number of observed data, $C_0(T_i)$ and $C_c(T_i)$ are the observed and calculated phase velocities, respectively, and $\sigma(T_i)$ is the standard deviation at a period of T_i. With this into consideration, the fitness of the jth model is obtained from

$$f_j = \frac{1}{\Phi_j} \tag{3.21}$$

and for the jth model, the probability of reproduction, p_r^j, is determined by

$$p_r^j = \frac{f_j}{\sum_{k=1}^{Q} f_k} \tag{3.22}$$

By means of the above value of probability, Q models from the current generation are selected using the roulette rule and modified in order to obtain new models in the next generation.

In the crossover stage, the surviving models are paired through the use of the crossover probability, p_c, which represents the probability of a pair to exchange parts or to remain as they are into the next generation.

Finally, when mutation takes place, each model is randomly changed depending on its mutation probability, p_m. By performing all the above procedures, the initial population may be able to approach to the global optimal solution.

c) Estimated Shear-wave Profiles

In the estimation of the seven shear-wave velocity profiles along line A-A' in Villa El Carmen, due to the non-uniqueness of their solutions, the inversion of the surface-wave dispersion data was performed five times for each profile. In the GA formulation, the number of models per population, generations and preliminary parallel runs was fifty and also the effect of higher modes of Rayleigh waves was taken into consideration. Fig. 3.3 shows the effectiveness of the adopted optimization method through the comparison of the observed and calculated dispersion curves.

Additionally, reliability of the obtained profiles was ensured by the good agreement between the H/V spectra of Rayleigh waves for the fundamental mode of the inverted profiles and their respective H/V spectral ratio of a single microtremor point (Fig. 3.4), that corresponds either to the center of the circular sensor deployment or a location in the neighboring areas of the array.

Finally, the estimated shear-wave velocity (V_S) profiles for each of the performed runs, as well as their average, are shown in Fig. 3.5.

With regard to the tests carried out in the flat region, the bedrock in P_Array1, i.e. materials with a V_S value higher than 3000m/s, is reached at a depth of about 150m. As expected, while approaching to the foothill, the depth to the bedrock decreases, e.g. to a value of 100m for P_Array2 and P_Array3, as well as the natural period of the soil. It is noteworthy to mention that in case of P_Array2, it was not possible to obtain information of its dispersion curve for the long period range due to the limited available space for the array deployment and, therefore, this part was adopted from results of CSM array (Calderon, 2012b), since it showed a similar trend and it is almost located at the same distance from the foot of the slope (Fig. 3.1).

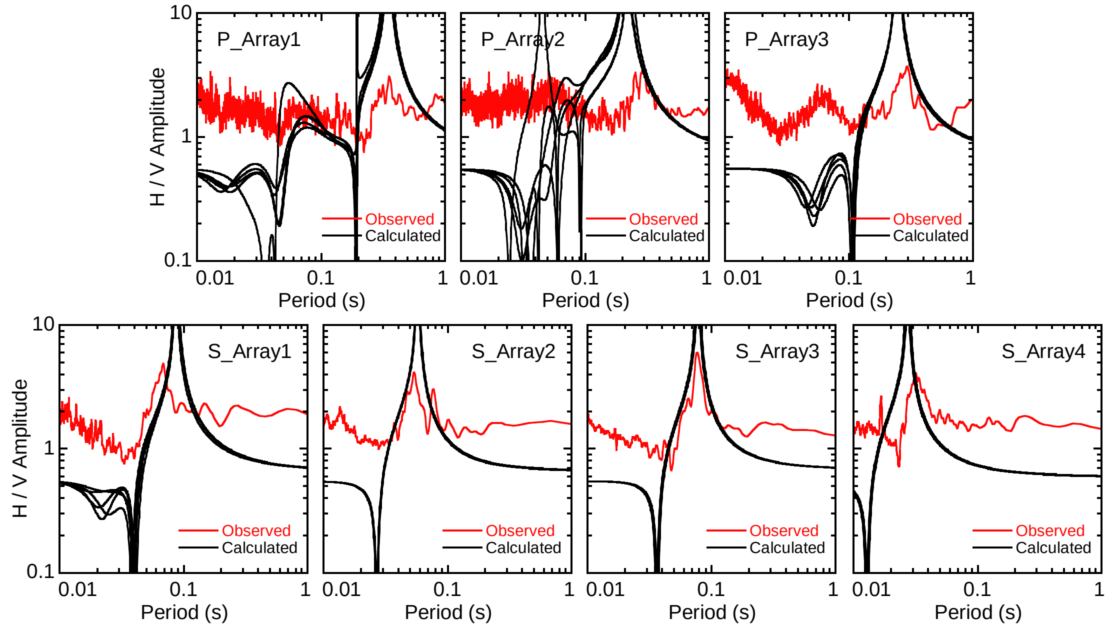

Fig. 3.4 Observed and theoretical H/V spectra

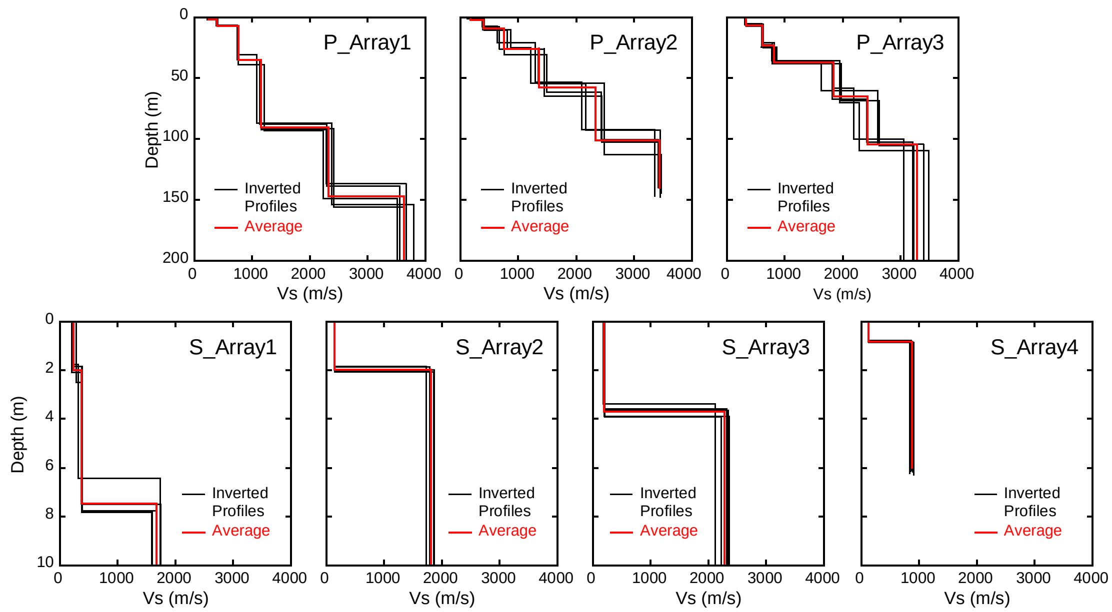

Fig. 3.5 Calculated shear-wave velocity profiles along line A-A' (Villa El Carmen)

On the other hand, when analyzing the shear-wave velocity profiles along the slope, a drastic reduction of the depth of materials of intermediate stiffness, with V_S of around 1700m/s, is evident in the foot of the slope (S_Array1). Another characteristic of this group of soil profiles is the presence of a soft shallow layer with a value of V_S lower than 200m/s. This can be explained by the fact that most of the flat areas in the slope are generated by the widely used technique known as “cut and fill”. In this earthmoving method, superficial natural rocky materials are removed and utilized for building retaining walls, whereas materials borrowed from landfills, with poor dynamic properties, are used to fill the generated spaces and to produce flat areas, such as those required for the construction of houses and roads.

3.3 Lomo de Corvina (Villa El Salvador)

Unlike Villa El Carmen, areas sufficiently large that allow the execution of microtremor circular arrays are very scarce in the vicinities of Lomo de Corvina. Therefore, information regarding the dynamic properties of the underground structure along the slope was obtained by means of a combination of active surface-wave tests (MASW), single point microtremor measurements and a reliable estimation of the deep shear-wave substructure in the central part of the district.

3.3.1 Multichannel Analysis of Surface Waves (MASW)

The use of surface seismic surveys in the geotechnical engineering field started back in the early 1950s. The convenience of this class of method relies on the fact that for a compressional impact source, as in general used in active tests, almost two-thirds of the generated energy is transmitted in the form of horizontally-travelling plane Rayleigh waves that can be considered as the main component of a typical recorded ground roll. Therefore, the dispersive characteristics of surface waves, i.e. waves of different frequencies propagate at different phase velocities, can be appropriately adopted to accurately identify the dynamic properties of a layered soil substructure.

The Multichannel Analysis of Surface Waves (MASW) test is one of the most conventional non-invasive seismic exploration methods and started to be widely used in the early 2000s (Park et al., 1999).

The common procedure will be explained in the following subsections and includes the acquisition of reliable data, the generation of an appropriate dispersion curve and its respective inversion. It is important to mention that the above steps were performed by means of the software package called SeisImager/SW, developed by OYO Corporation.

a) Data Acquisition

In general, the field equipment required for an MASW test consists of an adequate impact source, a series of vertical-motion receivers, a multichannel seismograph device and a portable computer controller. Fig. 3.6a shows the overall setup for a typical MASW active survey and Fig. 3.6b presents the deployment of the equipment for tests conducted in Villa El Salvador.

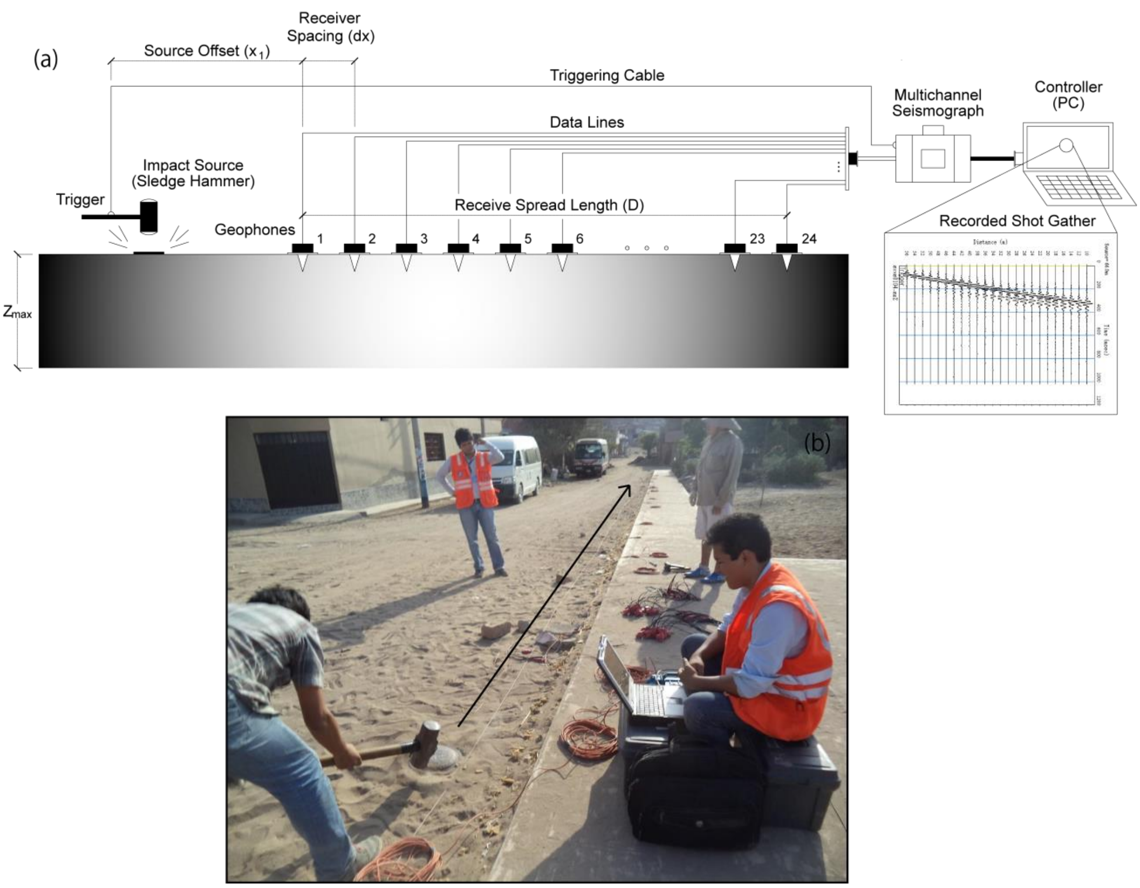

Fig. 3.6 (a) General equipment distribution of a MASW field survey, (b) MASW test conducted in Villa El Salvador

Normally, the optimal efficiency for certain equipment geometry is reflected in the maximum investigation depth (Z_{max}) determined by the longest wavelength of surface waves in the analysis (L_{max}). Typically, the assumption $Z_{max} \approx 0.5L_{max}$ is used, being L_{max} basically controlled by the amount of energy that the impact source provides to the system. As a general rule, a longer L_{max} is achieved with a greater source power and the impact of a fairly heavy sledge hammer against a metallic base plate is normally utilized.

MASW equipment geometry basically consists of a number of equally spaced receivers deployed along a line. In order to explore greater depths, low-frequency devices are always preferable and it is common practice to use 4.5Hz vertical geophones due to their good cost-performance ratio. When looking for the optimal geometry, several parameters have to be carefully chosen (Park et al., 2002), but, as stated before, since surface waves contain the highest signal-to-noise (SN) ratio due to their strong energy, the selection criteria has greater tolerance compared to other seismic methods.

To begin with, the receiver spread length (D) is, to some extent, linked to L_{max}, which is in turn related to Z_{max} and, as a general rule, the expression $D = m{\cdot}Z_{max}$ ($1 \leq m \leq 3$) is adopted, being its maximum value limited by the undesirable dominance of body and higher mode Rayleigh waves at far offsets (far-field effects). In the other hand, the receiver spacing (dx) has to be chosen not as wide that provokes the attenuation of high-frequency components since it is associated to the resolution for shallow layers.

Considering that it is essential for this type of tests to record horizontally-travelling plane Rayleigh waves, preferably of the fundamental mode, it is important to adopt a source offset (x_1) that guarantees the fully formation of this kind of waves and avoids the recording of either body or ambient noise wave fronts (near-field effects). Therefore, it is common practice to perform a set of shots at two different distances appropriately chosen from each extreme of the linear array.

b) Dispersion Analysis

An accurate estimation of the dispersion characteristics of the stratification under study is crucial in any type of surface-wave approach. In this particular method, the obtained dispersion curve is representative of the dynamic properties of the soil directly below the central point of the receiver spread.

Basically, a typical dispersion curve can be estimated from the linear slope of each component in the shot gather after an adequate isolation approach is applied to remove the effect of noise in the recorded waveforms (Park et al., 1998). This approach essentially includes the implementation of the Fourier transformation to the time series *(x,t)* and its representation as

$$U_{(x,w)} = P_{(x,w)} A_{(x,w)} \tag{3.23}$$

where $U_{(x,w)}$ is the Fourier transform separated into its phase spectrum $P_{(x,w)}$and its amplitude spectrum $A_{(x,w)}$.

The first one contains the information about the dispersion properties and is normally expressed in terms of frequency and its respective phase velocity. Finally, the effects of attenuation and spherical divergence, contained in $A_{(x,w)}$, are removed in order to be able to choose the points with maximum SN ratio for each desirable frequency

An archetypal dispersion curve obtained from MASW data, after applying the above scheme, is showed in Fig. 3.7. Regions in blue represent the areas of high energy and the red dots stand for points with the highest SN ratio for each frequency. It is important to note that the results represent a trend that can be manually changed by the user, if for example a high-mode effect is required to be removed before proceeding with the inversion process. Additionally, in order to assure reliable results, the assumed dispersion curve has to fall within the region delimited by the maximum and minimum wavelengths considered (expressed by the continuous black lines close to each axis) which were obtained from the geophones geometry particularly adopted.

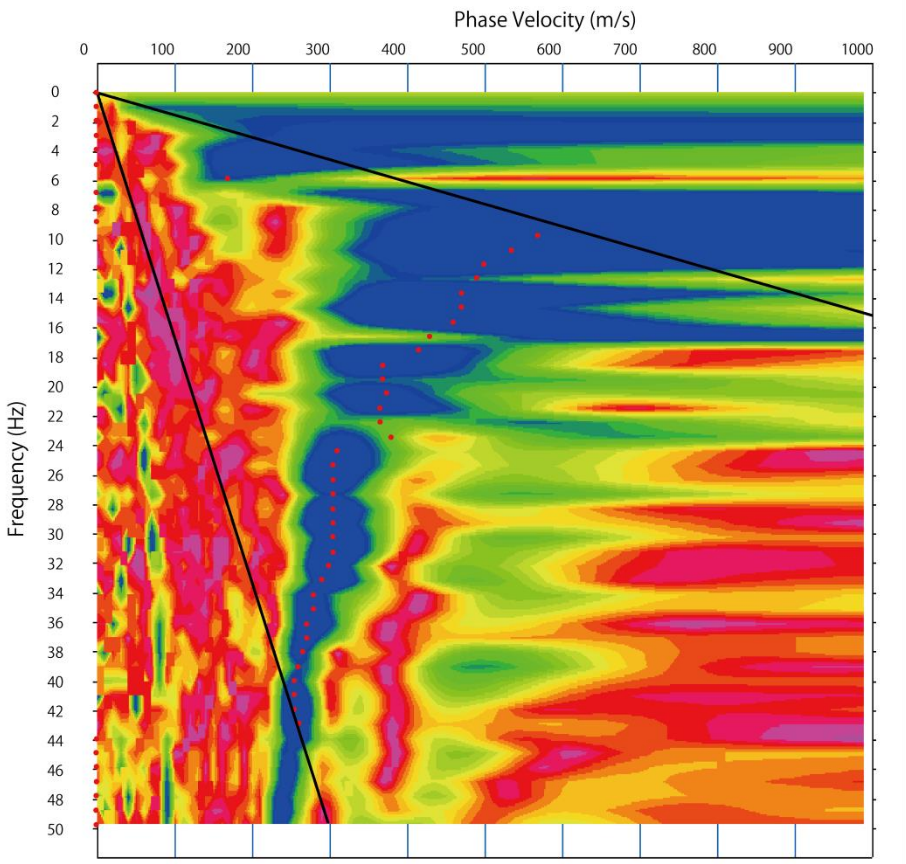

Fig. 3.7 Typical dispersion curve extracted from MASW data

c) Inversion Procedure

Shear-wave velocity profiles are obtained from calculated dispersion curves by means of an iterative inversion process. For the MASW tests in this work, the widespread weighted least-squares technique (Xia et al., 1999) was adopted for the calculation of the initial estimations.

As it was stated in a previous section, the Rayleigh-wave velocity, c_{Rj}, for a particular frequency, f_j, can be derived from the roots of a nonlinear formulation that include four dynamic properties of each of the layers forming the soil profile. Given the fact that, among other dynamic properties, shear-wave velocities mainly control the variation of Rayleigh-wave phase velocities, the number of unknowns reduces from $4n$-1 to n, causing the inversion procedure to be more efficient and stable.

Therefore, the nonlinear formulation can be linearized for m frequencies ignoring higher order term, as

$$\mathbf{J}\Delta\mathbf{x} = \Delta\mathbf{b} \tag{3.24}$$

where $\mathbf{x} = (v_{S1}, v_{S2}, \dots, v_{Sn})^T$, $\mathbf{b} = (b_1, b_2, \dots, b_m)^T$ represents the Rayleigh-wave phase velocities at m different frequencies and therefore $\Delta\mathbf{b} = \mathbf{b} - \mathbf{c}_R(\mathbf{x}_0)$ is the difference between the measured data and the initial estimation, $\Delta\mathbf{x}$ is the correction vector to be considered for the next step and $\mathbf{J}$ is the mxn Jacobian matrix.

The weighted objective function to minimize is set as follows

$$\varphi = \|\mathbf{J}\Delta\mathbf{x} - \Delta\mathbf{b}\|_2 \mathbf{W} \|\mathbf{J}\Delta\mathbf{x} - \Delta\mathbf{b}\|_2 + \alpha\|\Delta\mathbf{x}\|_2^2 \tag{3.25}$$

where $\| \quad \|_2$ is the ℓ_2-norm length of a vector, α is the damping factor that controls the speed of convergence and **W** the diagonal weighting matrix.

The minimization procedure is performed iteratively until it eventually converges to an acceptable solution or reaches a specific number of iterations, in order to produce a shear-wave velocity model by means of the updated $\Delta\mathbf{x}$. It is important to notice that also an initial model has to be determined at the beginning of the inversion process that is essentially given as

$$v_{Si} = c_R(f_i)/\beta \qquad (i = 1, 2, \dots, n) \tag{3.26}$$

where β is a constant in the vicinity of 0.88. v_{S1} (first layer) and v_{Sn} (half-space) are calculated using the c_R values corresponding to the highest and lowest frequency encountered in the dispersion curve, respectively.

3.3.2 Field Survey in Lomo de Corvina

With the objective of estimating the soil substructure in Lomo de Corvina, a set of active and passive surface-wave tests were considered in this study.

First, MASW tests were performed at five locations in places along the slope, including the top of the sandy dune, and the seashore. The information of these MASW was either gathered from a previous study (CISMID, 2011) or obtained from tests carried out in the framework of this work (CISMID, 2014). Information regarding the utilized equipment as well as the geometric constants in the sensor deployment for the two groups of tests considered can be consulted in Table 3.3.

Additionally, single point microtremor measurements were also performed in places nearby the MASW locations. In a similar way to MASW tests, the information for this type of analysis was either collected (CISMID, 2011) or obtained for this study. Analogous to the field survey in Villa El Carmen, a single point consisted of the measurement recorded by three CR 435-1S moving coil velocimeters connected to the GEODAS 15HS logger.

Fig. 3.8 shows the distribution of the analyzed tests along the two-dimensional profile under study (line B-B'), as well as deep V_S information in the central part of the district that will be mentioned in a future section. Exact locations of the above listed tests can be retrieved from the geographical coordinates in Table 3.4.

Table 3.3 Equipment and geometrical specifications for the MASW tests in Lomo de Corvina

	Gathered Tests (CISMID, 2011)	**For this Study (CISMID, 2014)**
Seismograph	12-channel ES 3000	24-channel McSeis-SW
Manufacturer	Geometrics	OYO Corporation
Receivers (number)	4.5Hz geophones (12)	4.5Hz geophones (24)
Impact Source	11kg sledge hammer	9kg sledge hammer
***D* (m)**	33	46
***dx* (m)**	3	2
x_1 (m)	5, 10	5, 10
Exploration Depth (m)	22	35

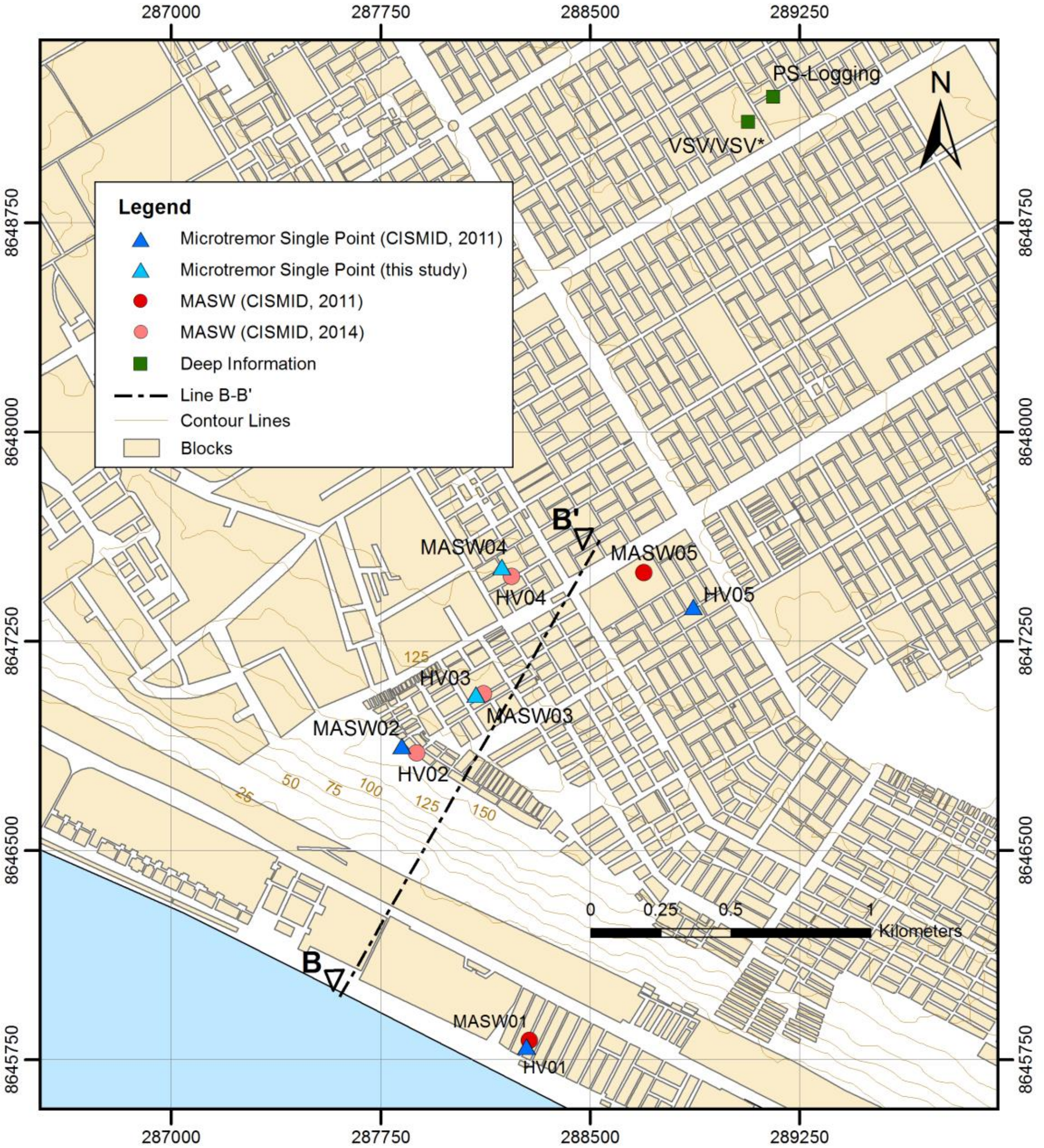

Fig. 3.8 Location of the conducted single microtremor points and MASW tests (CISMID, 2011 and for this study) along line B-B’

Table 3.4 Geographical coordinates of the geophysical tests considered for Lomo de Corvina

Test ID	Latitude	Longitude
MASW01	-12.242954^{o}	-76.946290^{o}
MASW02	-12.233609^{o}	-76.949943 ^{o}
MASW03	-12.231718^{o}	-76.947733^{o}
MASW04	-12.227920^{o}	-76.946777^{o}
MASW05	-12.227824^{o}	-76.942411^{o}
HV01	-12.243134^{o}	-76.946383^{o}
HV02	-12.233371^{o}	-76.950410^{o}
HV03	-12.231734^{o}	-76.947972^{o}
HV04	-12.227601^{o}	-76.947087^{o}
HV05	-12.228938^{o}	-76.940784^{o}
VSV/VSV*	-12.213252^{o}	-76.938887^{o}
PS-logging	-12.212435^{o}	-76.938045^{o}

3.3.3 Obtained Shear-Wave Velocity Profiles

As mentioned before, the least-squares approach was originally used as the inversion method for the fundamental-mode dispersion curves extracted from MASW data. These results served as the basis of the definition of search spaces for subsequent estimations of shear-wave velocity profiles by means of Genetic Algorithms (GA). Fig. 3.9 shows the comparison between the observed dispersion curves and those obtained for five runs of GA, whereas in Fig. 3.10 the inverted profiles and averages are plotted up to a reliable depth of 30m.

Additional useful information concerning the dynamic properties of the soil in Villa El Salvador includes a deep shear-wave velocity profile in the central part of the district, hereinafter to be referred to as VSV, up to the maximum V_S value of around 3000m/s, obtained from a set of linear and circular microtremor arrays with varying sensor spacing and radius, in each case (Calderon et al., 2012b). Moreover, a PS-logging test (OYO, 2012) was carried out years later on a site nearby and allowed the examination of diverse mechanical and dynamic properties up to a penetration depth of 50m. Consequently, the combination of these two surveys resulted in a representative deep V_S profile for the entire district. Location of the above information can also be examined in Fig. 3.8 and Table 3.4.

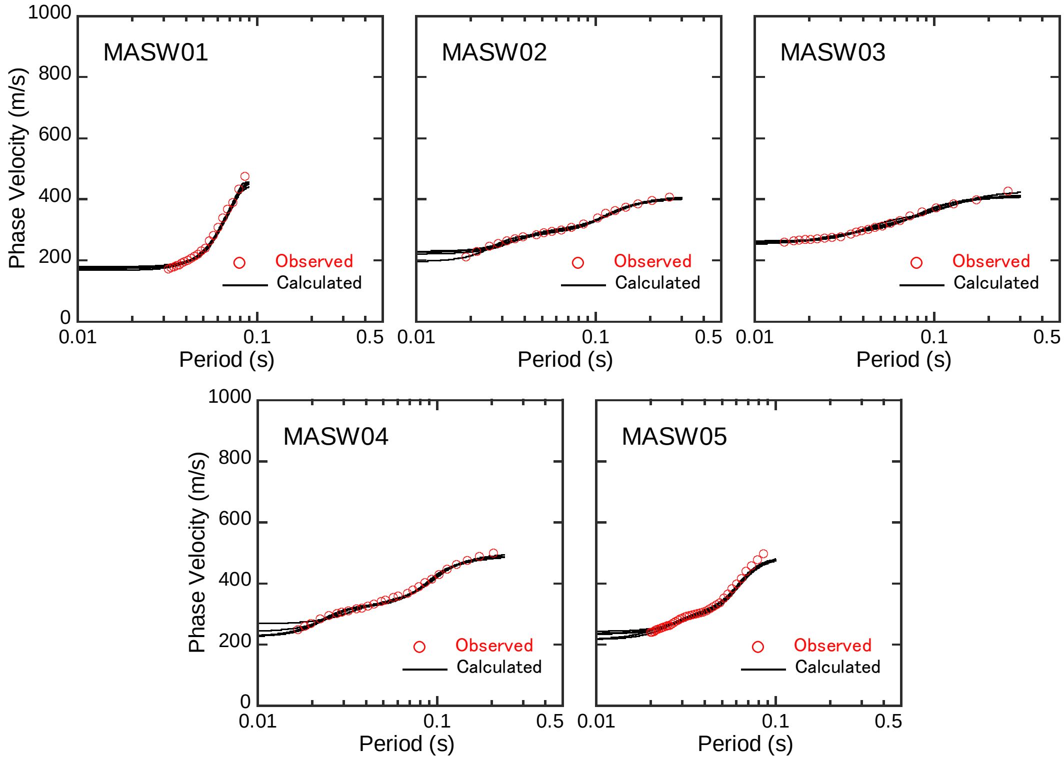

Fig. 3.9 Observed dispersion curves from MASW tests and those inverted from GA

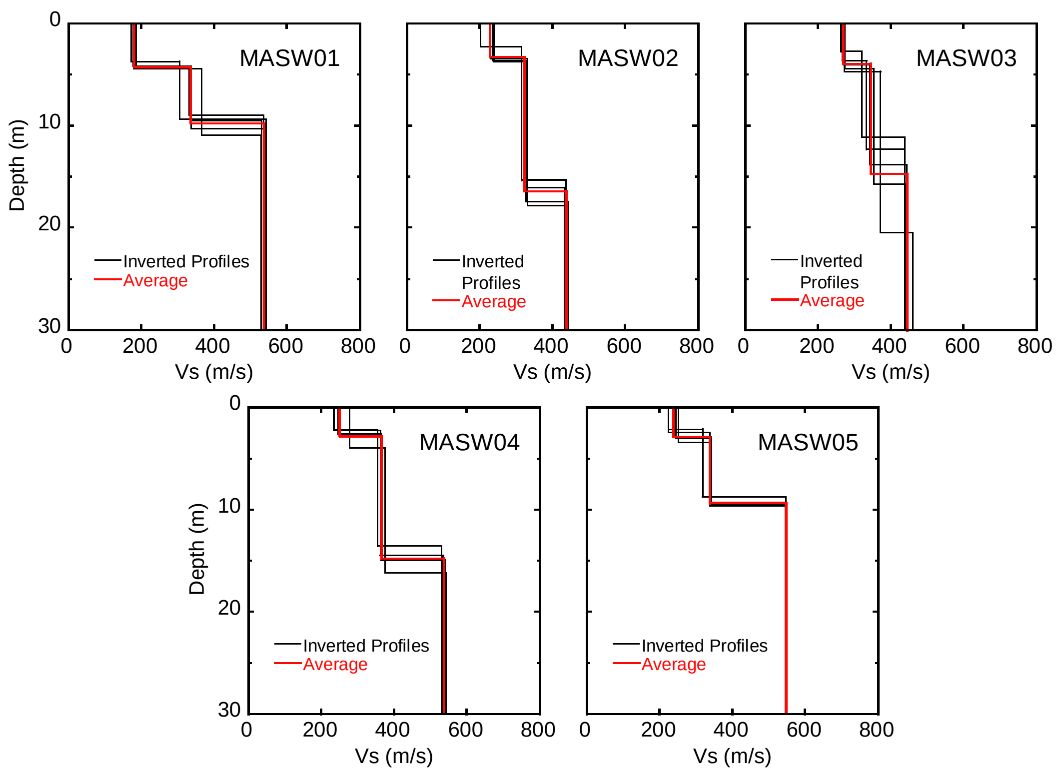

Fig. 3.10 Inverted V_S profiles from GA and their respective average

Regarding results from microtremor tests, as expected, increasing values of the soil natural period were obtained towards the top of the slope. This information was used as complementary data in order to assure reliability of the V_S profiles generated from the MASW tests since each of the single point microtremor measurements was conducted in a place nearby (Fig. 3.8).

It is well-known that, in case of Villa El Salvador, the long natural periods of the substructure are mainly caused by the impedance contrast of deep soil layers. Unfortunately, as it can be examined in Table 3.3 and Fig. 3.10, the exploration depths of the MASW tests were very limited and only considered the very shallow part of the soil substructure, so periods within the characteristic long period range could be hardly represented by using this information alone. Therefore, the decision of assuming a deep structure similar to that for VSV was taken, even if it is located 1.5km far from the sloping area under study, since most areas in Villa El Salvador can be considered as former dunes of identical geological origin, with the only difference that the materials facing the sea were deposited in the Holocene, whereas those in the opposite side were carried in the Pleistocene (Palacios et al., 1992).

After the deep regions of the five MASW profiles were completed, discrepancy in the peak value and shape between the H/V spectra of single point microtremor measurements (observed) and their correspondent H/V spectra of Rayleigh waves for the fundamental mode (theoretical) was still detected. Consequently, thickness of deep layers was adjusted taking into account the variation of the topography along line B-B’ and searching for a better fit between the theoretical and observed H/V spectra for all five profiles and VSV also (whose modification, henceforth will be referred to as VSV*). This procedure resulted in the completed V_S profiles shown in Fig. 3.11 which, in turn, generated analogous H/V spectra at each location (Fig. 3.12).

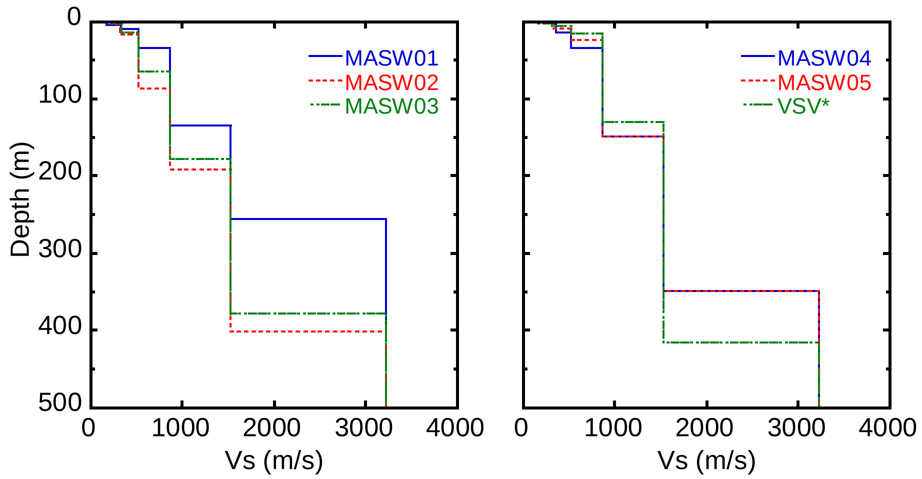

Fig. 3.11 V_S profiles from completed MASW tests and VSV*

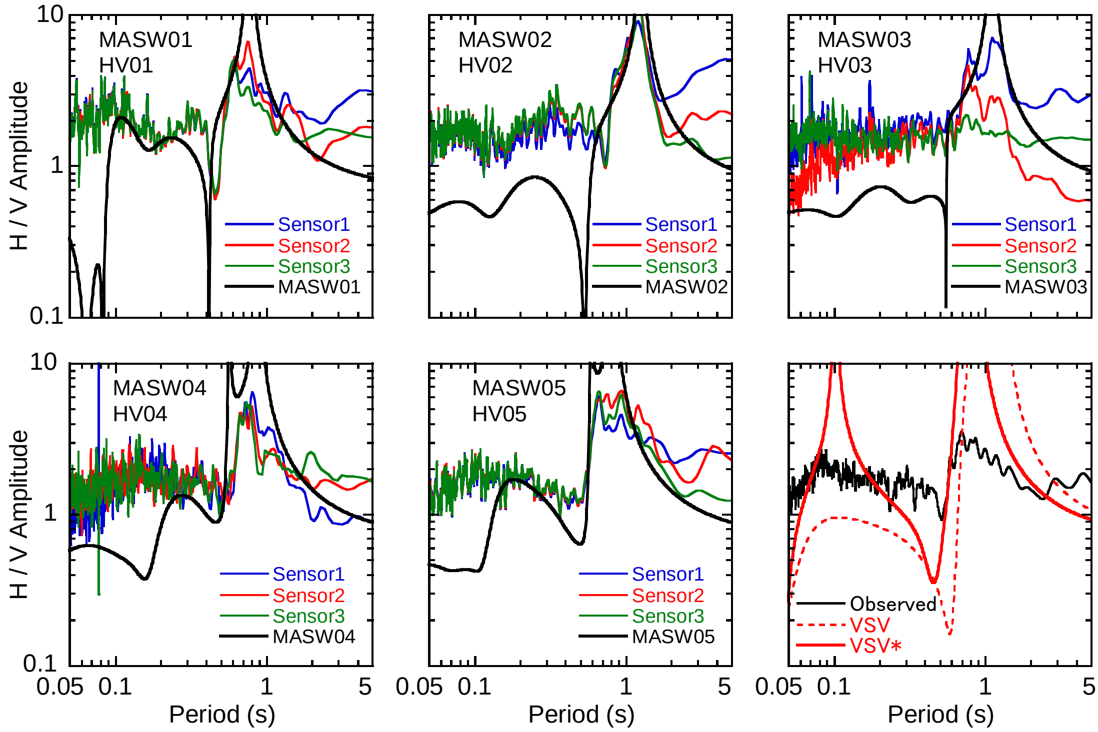

Fig. 3.12 Observed and theoretical H/V spectra at each test location and for VSV/VSV* profile

Chapter 4: Dynamic and Finite Element Modeling

4.1 Preface

This chapter presents relevant information regarding the geometric and simplified dynamic properties of the areas under study, as well as the methodologies and major assumptions utilized in their subsequent finite element modeling.

First, geometric characterization of the considered populated slopes was conducted. This includes the manipulation of the satellite images available for each of the places with the objective of extracting the stored altitude information. This step is of vital importance since the topographic idealization of the slope has significant impact in the propagation pattern for each of the input motions considered.

Previous chapters have dealt with the collection and extraction of dynamic characteristics, in the form of shear-wave velocity profiles and natural periods of vibration, at discrete points along the slopes under consideration. Within the limitations due to the scarce number of tests available, ground substructures, consisting of continuous soil layers with well-defined boundaries and properties, were still possible to be generated throughout the domains of the adopted models as presented in this chapter.

Two distinct methodologies were adopted in the mesh generation: the advancing frontal technique and the convex polygon approach. The aforementioned techniques were separately applied to the two-dimensional geometric regions resulting in finite element meshes with adequate element size for the transmission frequencies and dynamic properties considered.

Last part of the chapter presents the concepts concerning the finite element approach utilized for the solution of systems in the time domain. Special attention is given to the type of elements adopted, the solution algorithm and the form of idealization of an unbounded media with a geometric irregularity. Finally, a numerical application is presented which highlights the advantage and drawbacks of the adopted techniques.

4.2 Slope Geometry

With the objective of obtaining a reliable representation of the geometry of the populated slopes under analysis, altitude information was extracted from two different imagery sources: whereas for Villa El Carmen, data from ALOS satellite were available; for Lomo de Covina, ASTER information was utilized.

4.2.1 ALOS Data

The Advanced Land Observing Satellite "Daichi" (ALOS) is a multi-purpose observation instrument launched by the Japan Aerospace Exploration Agency (JAXA) in January, 2006. The satellite mainly consists of three devices: the Panchromatic Remote-sensing Instrument for Stereo Mapping (PRISM) for cartographic and urban planning purposes, the Advanced Visible and Near Infrared Radiometer type 2 (AVNIR-2) for acquisition of more precise spatial land-coverage information, and the Phased Array type L-band Synthetic Aperture Radar (PALSAR) for the extraction of topography through interferometry, among other functions.

In turn, PRISM is comprised of three sensors: forward, nadir and backward, from which the information of the Digital Surface Model (DSM) utilized for this study was extracted. Detailed explanation of the adopted stereo-matching process carried out by the Remote Sensing Technology Center of Japan (RESTEC) can be found in Matsuoka et al. (2013).

The available ALOS image for Lima (Fig. 4.1) was taken on October 15th, 2008 and has a pixel resolution of 5m. It is important to highlight that the presence of unfavorable observation conditions, such as clouds that might interfere in the extraction of reliable altitude information, is limited to areas towards the coastline and, therefore, did not affect the central part of the city where the area corresponding to Villa El Carmen is located.

4.2.2 ASTER Data

The Advanced Spaceborne Thermal Emission and Reflection Radiometer (ASTER) is one of the four instruments attached to the Terra satellite and essentially is a large digital camera composed of three telescopes. The set was launched in December, 1999 as a result of a joint effort between the Ministry of

Economy, Trade and Industry (METI) of Japan and the United States National Aeronautics and Space Administration (NASA) and acquires 600 high-resolution images a day, in average.

One of the main outputs of ASTER is its highly accurate Global Digital Elevation Model (GDEM) that covers almost all land on earth. For the extraction of the geometry of Lomo de Corvina, ASTER GDEM version 2 (METI and NASA, 2011) was utilized. This information is available in a GeoTIFF format with geographic latitude/longitude coordinates, a 1 arc-second (approximately 30m) grid and spatially adjusted and georeferenced to the WGS84/EGM96 geoid (Tachikawa et al., 2011).

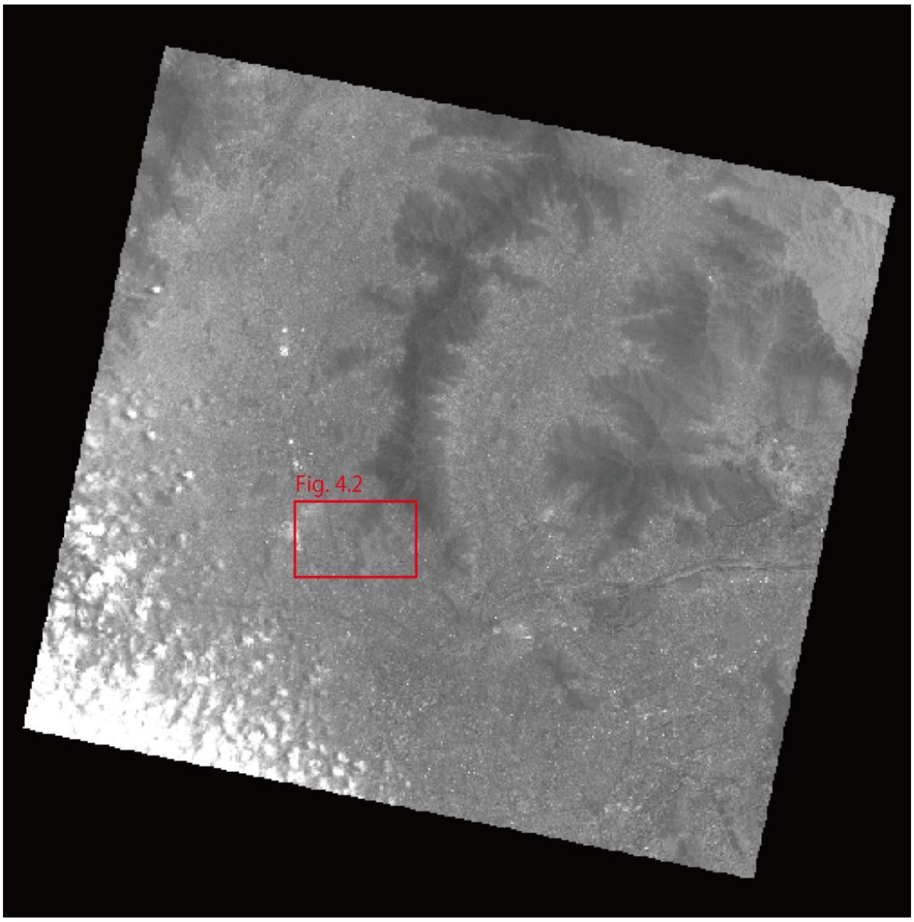

Fig. 4.1 ALOS/PRISM image shot on 2008/10/15 for the north part of Lima

4.2.3 Generation of Two-dimensional Profiles

The Geographical Information System (GIS) package known as ArcGIS was used to manipulate both the ALOS-DSM and ASTER-GDEM images due to its capability to project diverse imagery information, as well as other geometrical features, onto the same coordinate system, being in this case the WGS84. The general procedure includes:

- Plotting a line, representing the two-dimensional profile along which altitude information is required, over the specific satellite image.
- Dividing the aforementioned line into segments of certain length and creating control points at each vertex. In case of Villa El Carmen each segment was of 20m length and the endpoints are represented by the red circles in Fig. 4.2; whereas for Lomo de Corvina, the node spacing was 50m as it can be seen in the blue circles in Fig. 4.3.
- Extracting the altitude information at each control point by means of the bilinear interpolation of the information stored in the centers of the four nearest pixels. This estimation is made by a weighted average that takes into consideration the distance of each pixel center to the specific point.

It is important to note that in case of the considered models, not only the altitude information of the terrain was included but also the height of buildings and vegetation. Hence, the selection of the output points was carefully conducted to take into account only those lying entirely over the ground surface.

Another aspect to contemplate is that, in order to avoid the generation of unnecessarily large finite element models, the final utilized information does not include the entire lengths shown in Fig. 4.2 and Fig. 4.3. Thus, the two-dimensional profile for Villa El Carmen was restricted to the central third (section C-C’), whereas for Lomo de Corvina, the original region along which geophysical tests were conducted, B-B’, was considered.

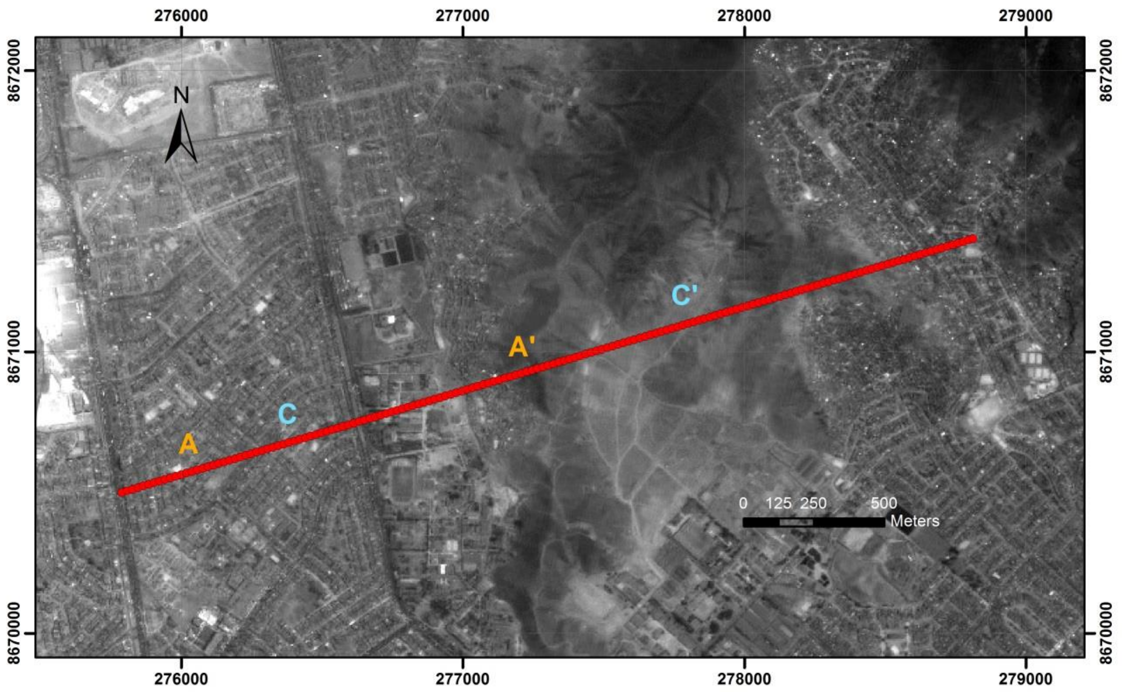

Fig. 4.2 Line A-A' along which field survey was conducted and line C-C' used for the slope modeling in Villa El Carmen

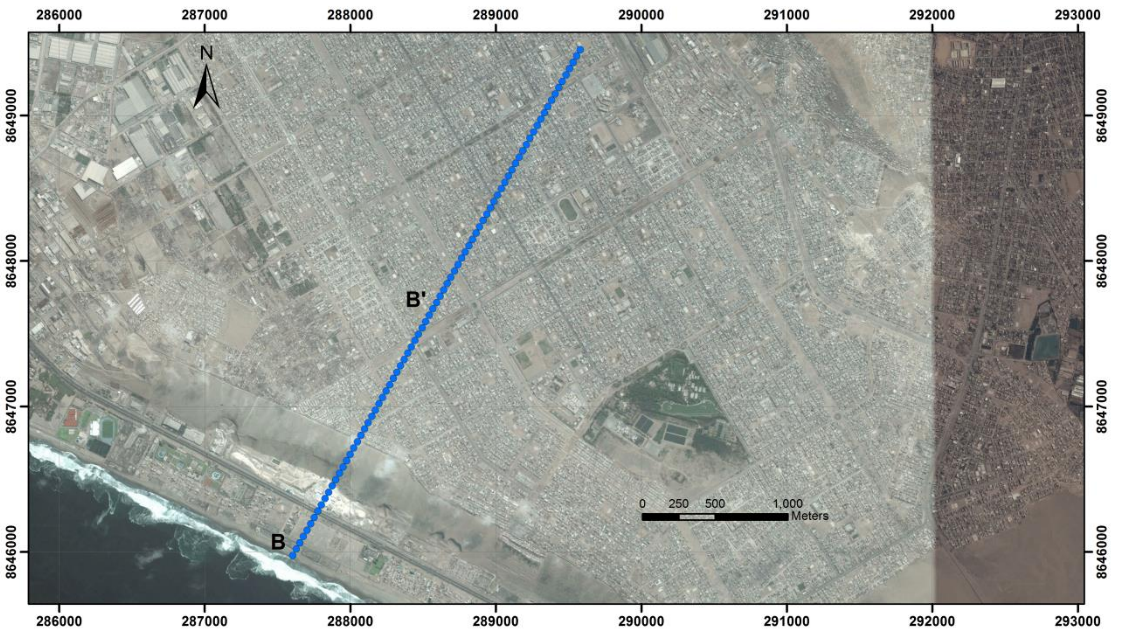

Fig. 4.3 Line B-B' considered for the slope modeling in Lomo de Corvina

4.3 Dynamic Properties

Chapter 3 explained in detail the process of obtaining shear-wave velocity (V_S) profiles at selected sites in the areas under study, independently. However, when constructing two-dimensional substructure soil models, consistency in the assumed stratification, i.e. for a certain layer, its value of V_S remains constant throughout the entire model, is required. The following sections provide information of the adopted strata for each of the considered study cases.

4.3.1 Villa El Carmen

In case of Villa El Carmen, the three microtremor array sets performed in the flat area allow the deep penetration of the underlying soil up to a value of V_S of around 3000m/s. Therefore, and due to their proximity to the rocky outcrops, a pattern substructure was obtained from the average of their respective V_S and adopted for the unexplored deep parts from the arrays conducted entirely along the slope.

Soil strata transition was assumed based on the fact that surface layers in the flat part gradually disappear towards the slope to eventually find complete rocky outcrops beyond the areas where houses are constructed. An approximate location of this outcropping was decided by visual inspection during the microtremor fieldworks.

Additionally, original CSM V_S profile (Calderon, 2012b) was also taken into consideration for the two-dimensional substructure. Its location was projected onto line A-A', resulting in point CSM* (Fig. 3.1), and while the thickness of each layer remained unaltered, their correspondent values of V_S were slightly modified to those from the aforementioned average pattern.

On the other hand, the thickness of the layer consisting of borrowed materials in the foothill (V_S = 176m/s) was assumed to be 2m, as it was the average obtained from linear and miniature circular arrays. Final values of V_S for the adopted soil substructure are listed in Table 4.1, as well as the variation of their respective thicknesses at the eight locations along A-A' in Villa El Carmen. In the following table, NE stands for the nonexistence of certain layer at a particular location.

Table 4.1 Values of V_S and thickness of the adopted stratification in Villa El Carmen at each test location

	Thickness (m)							
V_S (m/s)	**P_Array1**	**P_Array2**	**CSM***	**P_Array3**	**S_Array1**	**S_Array2**	**S_Array3**	**S_Array4**
176	NE	NE	NE	NE	2.0	2.0	2.0	2.0
212	2.0	2.0	NE	NE	NE	NE	NE	NE
384	5.4	7.5	6.5	8.0	5.5	NE	NE	NE
733	43.0	16.6	15.8	26.3	NE	NE	NE	NE
1623	59.5	32.0	25.5	28.5	28.5	NE	NE	NE
2405	55.0	42.3	51.6	41.0	41.0	41.0	41.0	37.0
3504	---	---	---	---	---	---	---	---

Table 4.2 shows the dynamic properties of each of the seven types of soil adopted and that corresponding to the half-space layer.

In case of the shallow layers, typical values of density (ρ), Poisson's ratio (υ) and damping ratio (ξ) for stiff soils, and borrowed materials in the slope, were adopted; whereas for the deep rocky layers, appropriated values according to their apparent type of rock, either quartz sandstone from the Herradura formation or quartzite from the Marcavilca formation, were considered (Zhao, 2005).

Table 4.2 Dynamic properties of the adopted stratification in Villa El Carmen

	ρ (kg/m^3)	V_S (m/s)	G (MPa)	υ	V_P (m/s)	ξ
Stratum-1	1500	176	47	0.35	367	0.040
Stratum-2	1700	212	77	0.25	368	0.030
Stratum-3	1800	384	265	0.25	664	0.020
Stratum-4	1800	733	967	0.20	1197	0.010
Stratum-5	2200	1623	5794	0.14	2508	0.004
Stratum-6	2200	2405	12720	0.14	3716	0.003
Stratum-7	2600	3504	31916	0.17	5556	0.002
Half-space	2600	3504	31916	0.17	5556	0.002

In the previous table, shear modulus and compressional-wave velocity were obtained from

$$G = \rho V_S^2 \tag{4.1}$$

$$V_P = \sqrt{\frac{2(1-\upsilon)}{(1-2\upsilon)}}V_S \tag{4.2}$$

Finally, Fig. 4.4 shows the assumed stratification of the soil substructure in Villa El Carmen within line C-C' as well as the location of the performed tests.

4.3.2 Lomo de Corvina

As explained in Section 3.3.3, shear-wave velocity (V_S) profiles were estimated at five locations in Lomo de Corvina and completed by the deep information of a profile previously obtained (VSV) in the central part of Villa El Salvador (Calderon, 2012b).

Even though materials on both sides of the slope were deposited at different geological ages, they correspond to the same type of quartzite sands. Therefore, for the ease of further modeling, a unique pattern of the soil substructure, obtained from the average of the V_S values from the completed MASW profiles, can be assumed along B-B'.

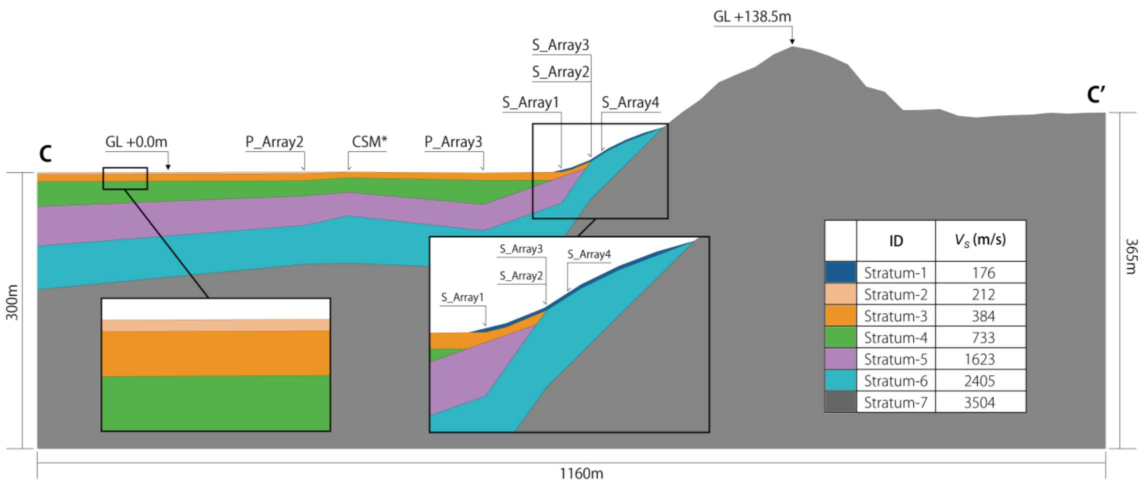

Fig. 4.4 Stratification of the soil substructure for Villa El Carmen

Table 4.3 Values of V_S and thickness of the adopted stratification in Lomo de Corvina at each test location

	Thickness (m)					
V_S (m/s)	**MASW01**	**MASW02**	**MASW03**	**MASW04**	**MASW05**	**VSV***
234	4.3	3.3	4.0	2.8	2.9	3.0 (150)
341	5.6	13.1	10.8	11.9	6.5	3.0 (320)
527	25.0	70.0	50.0	20.0	15.0	10.0 (530)
870	100.0	105.0	114.0	115.0	125.0	115.0
1535	122.0	210.0	200.0	200.0	200.0	285.0
3225	---	---	---	---	---	---

Table 4.3 shows the pattern V_S substructure adopted and the variation of the thickness at each of the MASW sites. It is important to emphasize that the original VSV was slightly modified based on the topographic variation along B-B’ and a PS-logging test (OYO, 2012). This information is referred to as VSV* in Table 4.3, in which the numbers in parenthesis represent the particular values of V_S for this soil profile.

The adopted stratification consists of six different types of soil, including the semi-infinite bottom layer. Values of ρ and υ listed in Table 4.4 were, to a large extent, adopted from the results of the extracted soil samples in the PS-logging test. Both, G and V_P were obtained from Eq. (4.1) and Eq. (4.2), respectively, whereas, frequency-independent damping ratios (ξ) are consistent with the values encountered in Lanzo and Vucetic (1999).

Table 4.4 Dynamic properties of the adopted stratification in Lomo de Corvina

	ρ (kg/m^3)	V_S (m/s)	G (MPa)	υ	V_P (m/s)	ξ
Stratum-1	1700	234	93	0.35	487	0.030
Stratum-2	1800	341	209	0.30	638	0.025
Stratum-3	1800	527	500	0.24	901	0.020
Stratum-4	1800	870	1362	0.14	1345	0.010
Stratum-5	2200	1535	5184	0.14	2373	0.004
Half-space	2600	3225	27043	0.14	4985	0.002

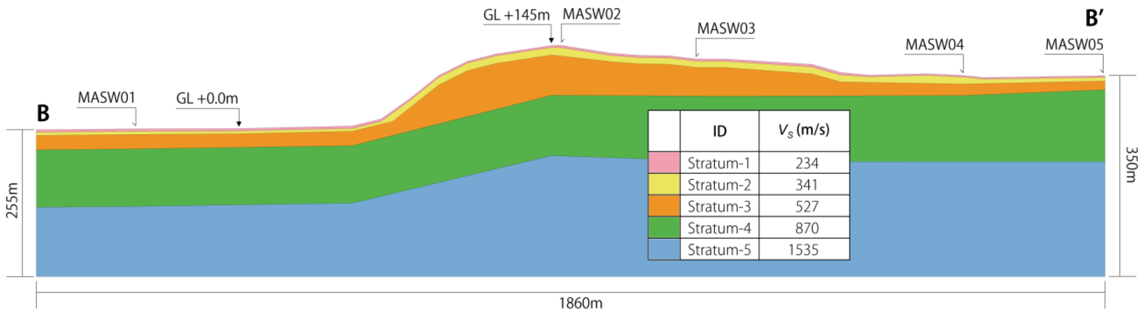

Fig. 4.5 Stratification of the soil substructure for Lomo de Corvina

Given the variations in height and the information of the materials comprising the underground within line B-B’, the adopted stratification for the populated slope in Lomo de Corvina is presented in Fig. 4.5. Additional information with regard to the location of tests can be also observed.

4.4 Mesh Generation

Adequate generation of the finite element meshes, consisting of quadratic quadrilateral elements, was conducted by means of the code package called Geompack++ which is an update of its predecessors Geompack90 and GEOMPACK (Joe, 1991). The name stands for Generation Of two-and three-dimensional finite element Meshes using efficient GEOMetric algorithms. For this study, a different type of mesh generation approach was adopted for each of the areas under study, as explained in the following sections.

4.4.1 Advancing Front Technique

The simplicity of this automatic quadrilateral mesh method relies in the fact that it only requires, among other considerations for each particular case, information of the geometric boundary and a local feature size factor to determine the mesh spacing for each edge (Zhu et al., 1991). The overall procedure involves heuristic techniques that allow the search from an initial grid towards an optimal steady state solution. The improvement of the elements is obtained through continuous cell refinement of the so-called front, in which element sides are activated or removed depending on the element formation sequence, in an equivalent updating process to that in the finite element solution technique explained in Section 4.5.4.

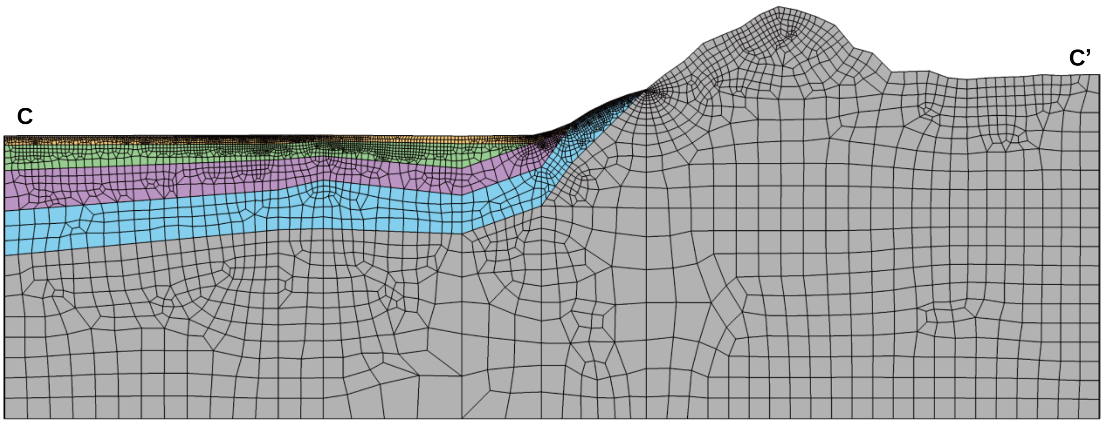

Fig. 4.6 Finite element mesh generated for Villa El Carmen

This method permits a larger local variability in the size of elements when compared to the mesh generated through other methods, such as the convex polygon approach, and sometimes leads to the formation of undesirable poor quality elements that has to be carefully controlled. On the other hand, one of the main disadvantages is the computation time, mainly due to the existence of additional internal operations.

The mesh which corresponds to Villa El Carmen was generated by means of the advancing front technique. In total, the model consists of 5379 elements and 16814 nodes whose distribution can be observed in Fig. 4.6. As it can be noticed, smaller elements are concentrated on the surface and size gradually increases towards the bottom of the model. This is an efficient common practice in finite element modeling that avoids the unpractical generation of additional degrees of freedom in areas of stiffer soil properties and that, in this particular case, allowed a maximum transmission frequency higher than the value normally adopted for engineering purposes.

4.4.2 Convex Polygon Approach

Mesh generation trough the convex polygon approach requires the polygonal boundary curves of the target region to be input in addition to, unlike the advancing front technique, the desired number of elements to be created. Supplementary parameters for a particular case, such as uniformness, improvement and smoothing iterations, etc., can also be specified.

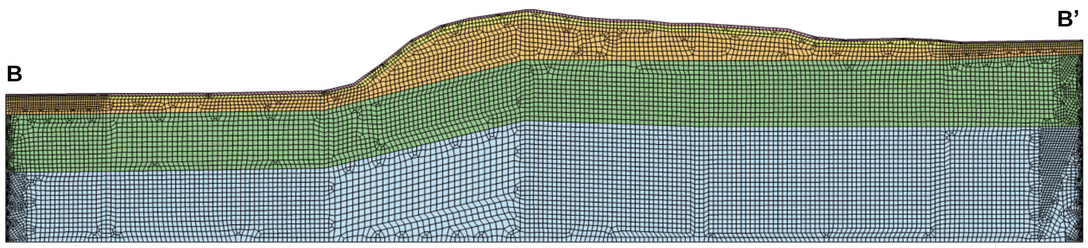

Fig. 4.7 Finite element mesh generated for Lomo de Corvina

The general scheme involves three stages (Joe, 1995): The first one decomposes the target region into convex polygons with the objective of avoiding small angles. The second step automatically estimates a mesh distribution function from the length scales of the subregions created in the previous step and, based on this function, divides them into smaller convex polygons where uniform elements can be constructed. Finally, in the third stage, mesh vertices are established along the edges of each convex polygon and quadrilaterals elements are generated. The last stage involves the estimation of a shrunken interior version of each subregion within which quadrilaterals are first created. Then, the strip between the boundary of the subregion and its respective shrunken polygon is tiled with additional quadrilateral elements.

The generation of the finite element mesh for Lomo de Corvina was performed by the above procedure. For the soil stratification within line B-B’, 36605 elements and 11970 nodes were created in an overall uniform mesh as shown in Fig. 4.7. Moreover, the mesh is affected by the concentration of elements on the sides due to the requirement of constrained nodes for the correct transfer of driving forces and the existence of slightly larger elements in the center of the bottom layer. From the above mentioned aspects, mesh uniformity may be the one with the greatest impact in solving the wave propagation problem, since it is well-known that uniform meshes are not desirable in cases when the V_S gradually changes through the model. Hence, a validation of the assumed mesh was made through the comparison of the results from the current mesh with those obtained by a commercial software with a varying mesh of linear elements. Only minor differences were found between both computations, mainly because of the adoption of quadratic elements in this study that allowed a maximum transmission frequency of about 18Hz; thus, the reliability of the proposed mesh is assured.

4.5 Finite Element Method

When dealing with dynamic equilibrium problems, such as in this study, the finite element method arises as one of the most widespread methodologies adopted to obtain an accurate approximate solution (Zienkiewicz et. al, 2013).

4.5.1 Basic Concepts

Essentially, the continuum domain considered, with a theoretical infinite number of degrees of freedom, is idealized as a series of elements connected at a finite number of points where the final solution, being in this case the displacement field, will be estimated and from which it can be interpolated at any position within the discretized domain.

One of the most well-known approaches in obtaining the governing equilibrium equations of the system is through the minimization of the total potential energy, π, which in its general form is expressed as

$$\pi = \frac{1}{2}\int_{V} [\boldsymbol{\sigma}]^{\mathrm{T}}\boldsymbol{\varepsilon} dV - \int_{V} [\mathbf{u}]^{\mathrm{T}}\mathbf{p} dV - \int_{S} [\mathbf{u}]^{\mathrm{T}}\mathbf{q} dS \tag{4.3}$$

where $\boldsymbol{\sigma}$, $\boldsymbol{\varepsilon}$ and $\mathbf{u}$ are the stress, strain and displacement vectors, respectively. The body forces are expressed by $\mathbf{p}$ whereas the applied surface tractions are represented by $\mathbf{q}$ and their respective integrations are taken over the volume V and surface area S, respectively.

In a discretized domain, contributions from each element are considered in the computation of the total potential energy. Then

$$\pi = \sum_{e} \pi_e \tag{4.4}$$

where π_e represents the potential energy of the element e.

As stated before, the displacement field can be represented from the values obtained at the discretized points, hereafter referred to as nodal points. This estimation is conducted within each element by means of interpolations. Thus

$$\mathbf{u} = \mathbf{N}\mathbf{u}^e \tag{4.5}$$

where $\mathbf{u}^e$ is the nodal displacement vector of the element and $\mathbf{N}$ is the matrix of the so-called shape interpolation functions. Hence

$$\mathbf{N} = [\mathbf{N}_1, \quad \cdots, \quad \mathbf{N}_m], \quad \mathbf{N}_i = N_i\mathbf{I} \tag{4.6}$$

$\mathbf{I}$ is an n x n identity matrix, n is the number of degrees of freedom per node and m is the number of nodes per element. It is important to highlight that the formulation of each N_i function strictly depends on the type of element adopted.

Additional quantities required for the computation of Eq. (4.3) are the strain and stress vectors, which are respectively obtained from

$$\boldsymbol{\varepsilon} = \mathbf{B}\mathbf{u}^e \tag{4.7}$$

$$\boldsymbol{\sigma} = \mathbf{D}\boldsymbol{\varepsilon} \tag{4.8}$$

where $\mathbf{B}$ is the element strain matrix calculated from derivatives of the adopted shape interpolation functions with respect to the global coordinate system

$$\mathbf{B} = [\mathbf{B}_1, \quad \cdots, \quad \mathbf{B}_m] \tag{4.9}$$

$$\mathbf{B}_i = \begin{bmatrix} \frac{\partial N_i}{\partial x} & 0 \\ 0 & \frac{\partial N_i}{\partial y} \\ \frac{\partial N_i}{\partial y} & \frac{\partial N_i}{\partial x} \end{bmatrix} \tag{4.10}$$

and $\mathbf{D}$ is the elasticity matrix defined depending on the type of problem to solve.

For plane stress situations

$$\mathbf{D} = \frac{E}{1-\upsilon^2}\begin{bmatrix} 1 & \upsilon & 0 \\ \upsilon & 1 & 0 \\ 0 & 0 & \dfrac{1-\upsilon}{2} \end{bmatrix} \tag{4.11}$$

whereas for plane strain conditions (such as for this study)

$$\mathbf{D} = \frac{E(1-\upsilon)}{(1+\upsilon)(1-2\upsilon)}\begin{bmatrix} 1 & \dfrac{\upsilon}{1-\upsilon} & 0 \\ \dfrac{\upsilon}{1-\upsilon} & 1 & 0 \\ 0 & 0 & \dfrac{1-2\upsilon}{2(1-\upsilon)} \end{bmatrix} \tag{4.12}$$

where E is the Young's modulus and υ represents the Poisson's ratio.

With the definition of the above expressions, the potential energy of a certain element, π_e, can be expressed as

$$\pi_e = \frac{1}{2}\int_{V_e} [\mathbf{u}^e]^{\mathrm{T}}[\mathbf{B}]^{\mathrm{T}}\mathbf{D}\mathbf{B}\mathbf{u}^e dV - \int_{V_e} [\mathbf{u}^e]^{\mathrm{T}}[\mathbf{N}]^{\mathrm{T}}\mathbf{p} dV - \int_{S_e} [\mathbf{u}^e]^{\mathrm{T}}[\mathbf{N}]^{\mathrm{T}}\mathbf{q} dS \tag{4.13}$$

where V_e and S_e are the element volume and element loaded surface area, respectively. The minimization of Eq. (4.13) with respect to the nodal displacement vector, $\mathbf{u}^e$, derives in

$$\frac{\partial \pi_e}{\partial \mathbf{u}^e} = \int_{V_e} ([\mathbf{B}]^{\mathrm{T}}\mathbf{D}\mathbf{B})\mathbf{u}^e dV - \int_{V_e} [\mathbf{N}]^{\mathrm{T}}\mathbf{p} dV - \int_{S_e} [\mathbf{N}]^{\mathrm{T}}\mathbf{q} dS = \mathbf{K}^e\mathbf{u}^e - \mathbf{F}^e \tag{4.14}$$

where $\mathbf{F}^e$ is the equivalent nodal forces vector and

$$\mathbf{K}^e = \int_{V_e} ([\mathbf{B}]^{\mathrm{T}}\mathbf{D}\mathbf{B})\mathbf{u}^e dV \tag{4.15}$$

is the so-called element stiffness matrix.

The equilibrium state of the system is reached when each element contribution in Eq. (4.14) is added and the result equated to zero. In case of static elastic problems, the equilibrium formulation can be simply expressed as

$$\mathbf{Ku} = \mathbf{F} \tag{4.16}$$

where $\mathbf{K}$ and $\mathbf{F}$ are the overall stiffness matrix and load vector of the system, respectively. In a structural dynamic problem, the resultant force is equated to the inertial forces and the equilibrium equation takes the form of the Newton's second law. Thus

$$\mathbf{F} - \mathbf{Ku} = \mathbf{M\ddot{u}} \tag{4.17}$$

When damping is included, the equation of motion is typically written as

$$\mathbf{M\ddot{u}} + \mathbf{C\dot{u}} + \mathbf{Ku} = \mathbf{F} \tag{4.18}$$

where $\mathbf{M}$, mass matrix; $\mathbf{C}$, viscous damping matrix; $\mathbf{K}$, stiffness matrix; $\mathbf{F}$, external force, $\mathbf{\ddot{u}}$, acceleration vector; $\mathbf{\dot{u}}$, velocity vector; and $\mathbf{u}$, displacement vector.

In a similar way, the overall mass matrix, $\mathbf{M}$, is obtained from the contributions of the element mass matrix, $\mathbf{M}^e$, which is obtained from

$$\mathbf{M}^e = \int_{V_e} [\mathbf{N}]^{\mathrm{T}} \rho \mathbf{N} dV \tag{4.19}$$

where ρ is the density of the element under consideration.

Finally, the formulation of the viscous damping matrix, $\mathbf{C}$, depends on the attenuation type adopted, as explained in Section 5.3.

4.5.2 Quadratic Isoparametric Elements

In finite element analysis, the simplest element possibly adopted is that with nodal points defined at the vertices only. This type of element merely allows a linear variation of a required field within its domain and is considered to be the lowest possible form of approximation with limited accuracy.

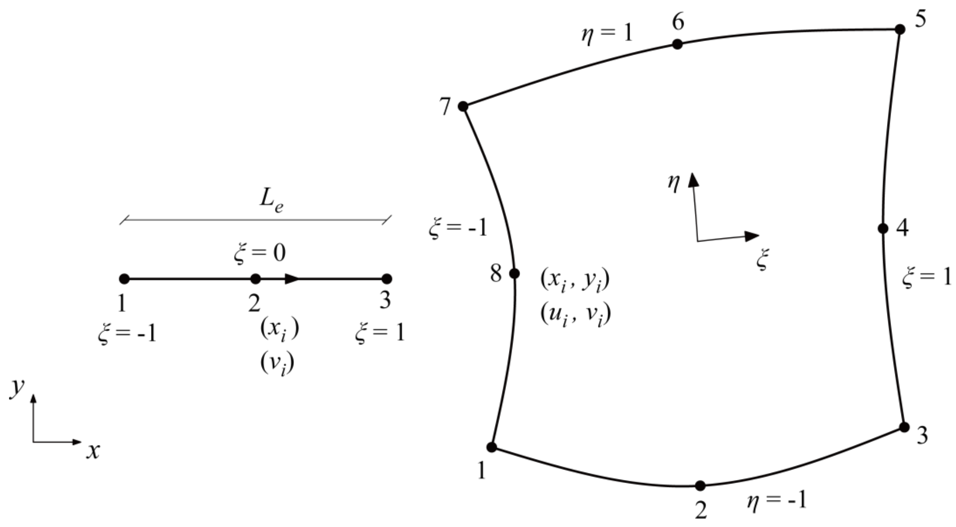

Fig. 4.8 One and two-dimensional quadratic isoparametric elements

In order to overcome this difficulty, the use of higher-order elements of arbitrary shape, called quadratic isoparametric elements, has been implemented (Ergatoudis et al., 1968). The improvement was reached by considering an additional middle node in each side that permits the element to be distorted following a curvilinear path. Fig. 4.8 shows typical one and two-dimensional quadratic elements with their respective natural coordinate system, (ξ, η) or ξ, in which constant values of ± 1 are defined in each edge node/side.

The adoption of quadratic elements is strictly linked with the definition of their respective shape interpolation functions. These functions must guarantee continuity between elements and have the capacity of reproducing constant strain conditions. Thus, for one-dimensional, shape functions are defined as

$$N_{1(\xi)} = -\frac{1}{2}\xi(1-\xi) \tag{4.20}$$
$$N_{2(\xi)} = (1-\xi)(1+\xi)$$
$$N_{3(\xi)} = \frac{1}{2}\xi(1+\xi)$$

whereas for two-dimensional elements,

$$N_{1(\xi,\eta)} = -\frac{1}{4}(1-\xi)(1-\eta)(1+\xi+\eta) \tag{4.21}$$

$$N_{2(\xi,\eta)} = \frac{1}{2}(1-\xi^2)(1-\eta)$$

$$N_{3(\xi,\eta)} = \frac{1}{4}(1+\xi)(1-\eta)(\xi-\eta-1)$$

$$N_{4(\xi,\eta)} = \frac{1}{2}(1+\xi)(1-\eta^2)$$

$$N_{5(\xi,\eta)} = \frac{1}{4}(1+\xi)(1+\eta)(\xi+\eta-1)$$

$$N_{6(\xi,\eta)} = \frac{1}{2}(1-\xi^2)(1+\eta)$$

$$N_{7(\xi,\eta)} = \frac{1}{4}(1-\xi)(1+\eta)(-\xi+\eta-1)$$

$$N_{8(\xi,\eta)} = \frac{1}{2}(1-\xi)(1-\eta^2)$$

The term ‘isoparametric’ refers to the capability of the above shape interpolation functions characteristic to a given type of element, $N_{i(\xi,\eta)}$, to describe both the Cartesian coordinates and the solution (displacement) field. Therefore, the geometry within an element, $x_{(\xi,\eta)}$ and $y_{(\xi,\eta)}$, is defined by

$$x_{(\xi,\eta)} = \sum_{i=1}^{m} N_{i(\xi,\eta)} \,.\, x_i \tag{4.22}$$

$$y_{(\xi,\eta)} = \sum_{i=1}^{m} N_{i(\xi,\eta)} \,.\, y_i$$

where (x_i, y_i) are the coordinates of node i. In the other hand, the displacement field, $u_{(\xi,\eta)}$ and $v_{(\xi,\eta)}$ is obtained as

$$u_{(\xi,\eta)} = \sum_{i=1}^{m} N_{i(\xi,\eta)} \,.\, u_i \tag{4.23}$$

$$v_{(\xi,\eta)} = \sum_{i=1}^{m} N_{i(\xi,\eta)} \,.\, v_i$$

where $(u_i, v_i)$are the displacements of node i.

In Eq. (4.22) and Eq. (4.23), m stands for the number of nodes that define an element, being 3 or 8 for quadratic elements, as all those adopted throughout this study.

4.5.3 Time Domain Analysis

The second order differential equation, Eq. (4.18), is solved numerically in the time domain at each time step Δt by direct integration (Newmark, 1959). Then, it is convenient to express it in its incremental form as

$$\mathbf{M}\Delta\ddot{\mathbf{u}} + \mathbf{C}\Delta\dot{\mathbf{u}} + \mathbf{K}\Delta\mathbf{u} = \Delta\mathbf{F} \tag{4.24}$$

The Newmark-β approximations of the velocity, $\dot{\mathbf{u}}_{(t+\Delta t)}$, and displacement, $\mathbf{u}_{(t+\Delta t)}$, vectors, at the instant value of time $(t + \Delta t)$, are expressed as follows

$$\begin{gathered} \dot{\mathbf{u}}_{(t+\Delta t)} \approx \dot{\mathbf{u}}_{(t)} + \frac{\Delta t}{2}\left(\ddot{\mathbf{u}}_{(t)} + \ddot{\mathbf{u}}_{(t+\Delta t)}\right) \\ \mathbf{u}_{(t+\Delta t)} \approx \mathbf{u}_{(t)} + \Delta t\dot{\mathbf{u}}_{(t)} + \left(\frac{1}{2} - \beta\right)\Delta t^2\ddot{\mathbf{u}}_{(\mathrm{t})} + \beta\Delta t^2\ddot{\mathbf{u}}_{(t+\Delta t)} \end{gathered} \tag{4.25}$$

where β and γ are the Newmark's parameters.

By rearranging Eq. (4.25), it is possible to retrieve the incremental vectors for velocity and acceleration, respectively

$$\begin{gathered} \Delta\dot{\mathbf{u}} = \left(\ddot{\mathbf{u}}_{(t)}\gamma\Delta\ddot{\mathbf{u}}\right)\Delta t \\ \Delta\ddot{\mathbf{u}} = \frac{1}{\beta\Delta t^2}\left(\Delta\mathbf{u} - \dot{\mathbf{u}}_{(t)}\Delta t - \frac{\Delta t^2}{2}\ddot{\mathbf{u}}_{(t)}\right) \end{gathered} \tag{4.26}$$

Replacing Eq. (4.26) in Eq. (4.24)

$$\left(\frac{1}{\beta\Delta t^2}\mathbf{M} + \frac{\gamma}{\beta\Delta t}\mathbf{C} + \mathbf{K}\right)\Delta\mathbf{u} \tag{4.27}$$

$$= \Delta\mathbf{F} + \mathbf{M}\left(\frac{1}{\beta\Delta t}\dot{\mathbf{u}}_{(t)} + \frac{1}{2\beta}\ddot{\mathbf{u}}_{(t)}\right) + \mathbf{C}\left(\frac{\gamma}{\beta}\dot{\mathbf{u}}_{(t)} + \left(\frac{\gamma}{2\beta} - 1\right)\Delta t\ddot{\mathbf{u}}_{(t)}\right)$$

Adopting $\beta = 0.25$ and $\gamma = 0.5$ for implicit and unconditional stability, the following expression is finally obtained

$$\left(\frac{4\mathbf{M}}{\Delta t^2} + \frac{2}{\Delta t}\mathbf{C} + \mathbf{K}\right)\Delta\mathbf{u} = \Delta\mathbf{F} + \mathbf{M}\left(\frac{4}{\Delta t}\dot{\mathbf{u}}_{(t)} + 2\ddot{\mathbf{u}}_{(t)}\right) + 2\mathbf{C}\dot{\mathbf{u}}_{(t)} \tag{4.28}$$

Once Eq. (4.28) is solved for $\Delta\mathbf{u}$, it is possible to obtain the displacement, velocity and acceleration vectors of the system for time $(t + \Delta t)$ through their respective incremental vectors, as in Eq. (4.26).

4.5.4 Frontal Solution Method

Special attention has to be paid in the adoption of the solving technique of a system of linear algebraic equations of the form $\mathbf{Ax} = \mathbf{b}$, such as in Eq. (4.28), in which $\mathbf{A}$ is symmetric and positive-definite. Several approaches are extensively available, ranging from iterative methods in which the solution is sought until a convergence condition is reached, to direct elimination techniques. Due to its proved efficiency when compared to other direct techniques, such as banded equation methods, the frontal equation solution algorithm (Irons, 1970) was employed in this study.

In general, the solution process is divided into three main stages: assembly, elimination and backsubstitution. The key feature is built on the fact that assembly and elimination of variables in equations are conducted simultaneously, meaning that, once all the contributions coming from elements containing certain degree of freedom (DOF) are taken into account, that DOF is ready to be eliminated and therefore, global matrices are never completely assembled (Hinton and Owen, 1977).

From the aforementioned, the concept of the ‘front’ follows. This is related to the correspondent ‘active’ variables stored at a particular time and its length, referred to as the ‘frontwidth’, constantly changes and depends mostly on the order element numbering, unlike other direct techniques. In addition, the maximum size of a problem to be solved is controlled by the ‘maximum frontwidth’ which is conveniently calculated prior the frontal solution initiates since large percentage of the computation time is intrinsically associated to its value. Thus, due to symmetry, only the upper triangle part of the stiffness matrix is required to be stored, being its maximum permissible value obtained from

$$\mathrm{MSTIF} = \frac{\mathrm{MFRON}(\mathrm{MFRON}+1)}{2} \tag{4.29}$$

where, MFRON is the maximum frontwidth calculated.

Efficiency of the frontal solution method also relies in its resolution facility for multiple load cases i.e., for second and subsequent solutions, only the right hand load term of Eq. (4.28) is required to be updated and reduced from the information stored in the first load step, avoiding also the recomputation of the element stiffness.

4.5.5 Substructure Method

With the objective of conducting the finite element analysis of a system with a geometric irregularity, the substructure method (Nakai, 1985; Wada et al., 2014) was adopted.

The substructure method deals with this type of problem in the same form as the soil-structure interaction dynamics; so in this case, the soil with irregularity will be termed as the ‘structure’. Essentially, this methodology is based on the principle of superposition from the elasticity theory and, consequently, the effects in the soil-‘structure’ system caused by vertical incident waves (Fig. 4.9a) can be divided into (Nakai, 2012):

1. The soil subsystem (Fig. 4.9b), representing the far field, with fixed null displacements due to a reaction force along the surface in contact with the structure.
2. The ‘structure’ subsystem (Fig. 4.9c) containing the irregularity (near field), in which the reaction force is released.

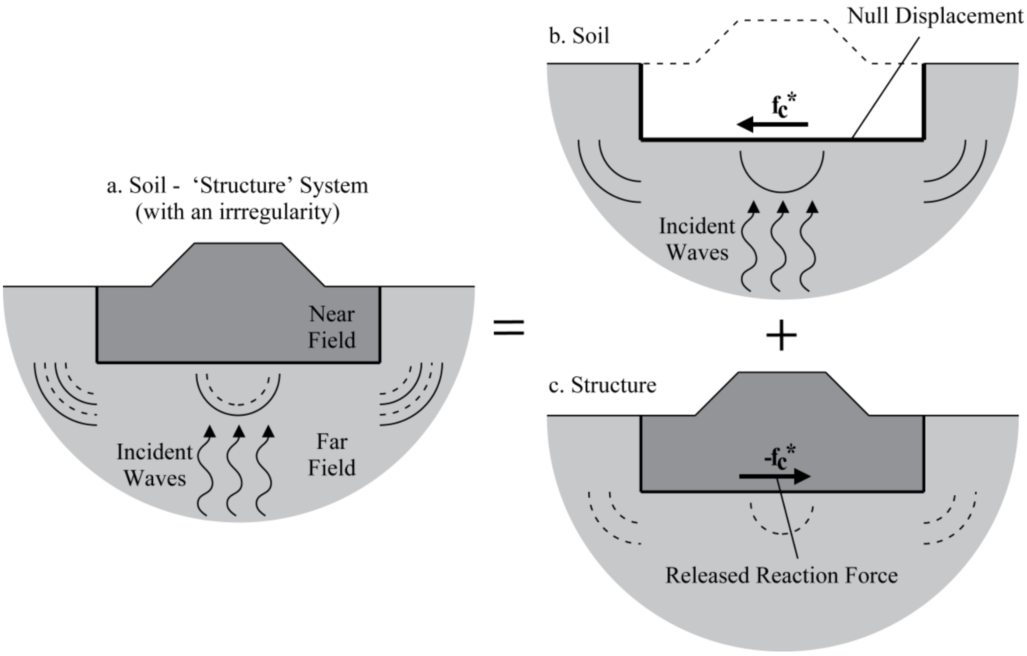

Fig. 4.9 Superposition principle in a soil-'structure' system with irregularity

In turn, the fixed condition in the contact surface of the soil subsystem can be conceived as a result of the effect of forced displacements applied in the opposite direction to those produced by incident waves (Fig. 4.10). Thus, the reaction force describing the influence of the far field over the near one, $\mathbf{f}_\mathbf{c}^*$, hereinafter called driving force, can be calculated from

$$\mathbf{f}_\mathbf{c}^* = \mathbf{K}_\mathbf{c}^* \mathbf{u}_\mathbf{c}^* \tag{4.30}$$

where, $\mathbf{K}_\mathbf{c}^*$ is the soil stiffness (force-displacement relationship) and $\mathbf{u}_\mathbf{c}^*$ the aforementioned displacements, both in the excavated ground along the contact surface. It is worth mentioning that for all formulations within the scope of the substructure method, superscript ***** represents a soil with excavation whereas subscript **c** refers to its contact surface.

Theoretically, $\mathbf{K}_\mathbf{c}^*$, which in fact describes an impedance matrix, can be obtained as the inverse of the flexibility matrix when applying unit forces along the contact surface. However, this is not a straightforward task and an alternative procedure based on the evaluation of the force states before and after the excavation is preferred. Thus, from the well-known relationship: change in force is equal to the impedance multiplied by the change in displacement, the following is obtained

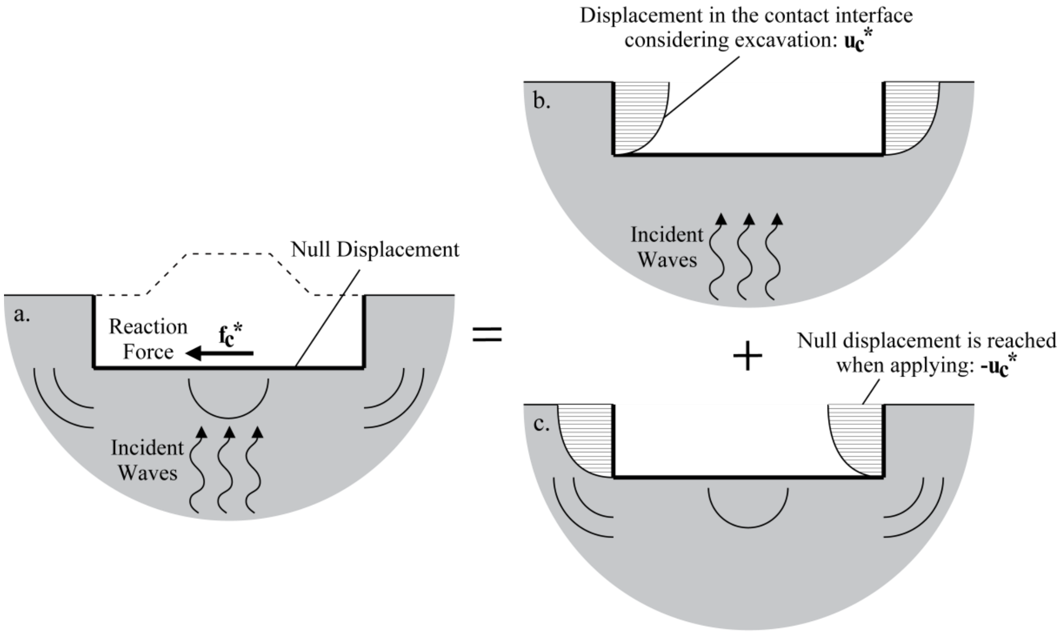

Fig. 4.10 Idealization of the soil-subsystem

$$\mathbf{0} - \mathbf{p_c} = \mathbf{K_c^*}(\mathbf{u_c} - \mathbf{u_c^*}) \tag{4.31}$$

where $\mathbf{p_c}$ and $\mathbf{u_c}$ are the force and displacement vectors before excavation in the contact surface. After isolating the term $\mathbf{K_c^*u_c^*}$ from the above expression and replacing it in Eq. (4.30), the driving force can be expressed as

$$\mathbf{f_c^*} = \mathbf{K_c^*u_c} + \mathbf{p_c} \tag{4.32}$$

In the time domain, Eq. (4.32) can be conveniently approximated as

$$\mathbf{f_c^*} \approx \mathbf{C_c\dot{u}_c} + \mathbf{p_c} \tag{4.33}$$

where $\mathbf{C_c}$ is the impedance matrix function when damper elements are placed along the virtual boundary. Thus, a typical element damper matrix, $\mathbf{C_c^{\mathit{e}}}$, is obtained from

$$\mathbf{C_c^{\mathit{e}}} = \int_{L_e} [\mathbf{N}]^{\mathrm{T}} \rho \begin{bmatrix} V_{\text{shear}} & 0 \\ 0 & V_{\text{comp}} \end{bmatrix} \mathbf{N} dL \tag{4.34}$$

where integration is taken over a quadratic one-dimensional element of length L_e as shown in Fig. 4.8 and, therefore, the corresponding shape interpolation functions are those listed in Eq. (4.20). V_{shear} and V_{comp} are either the shear-wave velocity, V_S, or the compressional-wave velocity, V_P, depending on the type of element under consideration, either placed along the sides or at the bottom of the model.

For the current work, the formulation in Eq. (4.33) was adopted, and $\dot{\mathbf{u}}_{\mathbf{c}}$ and $\mathbf{p}_{\mathbf{c}}$ were obtained after the computation of one-dimensional finite element analyses of soil columns with the same dynamic properties as of the side boundaries, with horizontal rollers for all nodes and dampers at the bottom, and then transferred to the global model to compute the driving forces.

Specifically, with respect to the term $\dot{\mathbf{u}}_{\mathbf{c}}$ in Eq. (4.33), it corresponds to the nodal velocities of the boundary elements transferred to the near field. It has to be noted that in case of the sides, $\dot{\mathbf{u}}_{\mathbf{c}}$ takes its correspondent value from the solution of the one-dimensional soil columns idealized to behave as free ground elements, whereas for the bottom, it adopts the values from the horizontal applied excitation.

Finally, the equivalent nodal forces vector, $\mathbf{p}_{\mathbf{c}}$, is calculated from the shear stresses generated at the boundary sides and in its element form is expressed as

$$\boldsymbol{p}_{\mathbf{c}}^{\boldsymbol{e}} = \int_{L_e} [\boldsymbol{N}]^{\mathrm{T}} \boldsymbol{\tau}^{\boldsymbol{e}} dL \tag{4.35}$$

where $\boldsymbol{\tau}^{\boldsymbol{e}}$ is the vector of shear stress computed from the nodal displacements after the one-dimensional solution of the side boundaries. It is important to underline that the correct estimation of the driving forces, $\mathbf{f}_{\mathbf{c}}^{*}$, permits the adequate estimation of the global response and avoids the rocking motion in non-symmetric models where the properties of the side soil columns on each side are different, such as the populated slopes in this study, but since it preserves the approximation stated in Eq. (4.33), the models are likely to generate parasitic vertical motions of very low amplitude along the sides, as discussed in the following section.

4.5.6 Numerical Application

With the objective of evaluating the suitability and accuracy of the substructure method in the finite element (FE) formulation, the analysis of three horizontally-layered soil models was conducted. Each of these analyses consisted in the computation of the response of a square-shaped two-dimensional model subjected to vertically propagating horizontal bottom excitation and the comparison with the results of its equivalent one-dimensional column for the same motion of complex frequency content of amplitude equal to 313cm/s^2. In theory, results must be identical and comparable with the target solution calculated in the frequency domain (FD).

Table 4.5 summarizes the dynamic properties of the materials comprising each of the adopted strata whereas Table 4.6 shows the layering information for the three soil models considered.

Table 4.5 Dynamic properties of the materials considered in the analysis of accuracy

	ρ (kg/m^3)	V_S (m/s)	V_P (m/s)	ξ
Stratum-1	1700	250	430	0.030
Stratum-2	1800	500	860	0.025
Stratum-3	2000	1000	1700	0.010
Stratum-4	2200	1750	3000	0.005

Table 4.6 Layering information and size of the analyzed soil models

	Model 1	**Model 2**	**Model3**
Size (m)	10	20	30
Overlying Layers	Stratum-1	Stratum-1 Stratum-2	Stratum-1 Stratum-2 Stratum-3
Half-space	Stratum -2	Stratum-3	Stratum-4

It has to be mentioned that the thickness of each layer is 10m. In addition, Rayleigh damping formulation, explained in Section 5.3, was adopted with the target frequencies being 3.33Hz and 25Hz for all the models, as well as a constant value of Poisson's ratio, υ, of 0.25.

Distribution of the absolute values of acceleration both in the horizontal and vertical directions are presented for Model 1, 2 and 3 in Fig. 4.11, Fig. 4.12

and Fig. 4.13, respectively.

As mentioned before, since the excitation applied is of the form of horizontal motion only, theoretically, all two-dimensional models considered must reflect the characteristic behavior of a one-dimensional soil column with the absence of vertical acceleration. Nevertheless, parasitic vertical components are still observed in the vicinities of the side boundaries.

Table 4.7 shows the comparison between the acceleration at the surface of the models for the type of analysis conducted. Differences between the results in the frequency and time domain are related to the adoption of frequency-dependent Rayleigh damping. As it is shown in Section 5.3, this discrepancy can be reduced by choosing a set of target frequencies which fit the desire value of surface acceleration, among other factors.

Divergences between results for one and two-dimensional finite element analyses are attributed to the formulation utilized in the computation of the driving force in the substructure method (Eq. (4.33)). Even though, results for two-dimensional models present vertical components on the edges, their magnitude is in the order of less than 1% of the maximum calculated horizontal motion and their effect in a soil-'structure' system could be reduced if the side boundaries are conveniently placed far from the geometric irregularity.

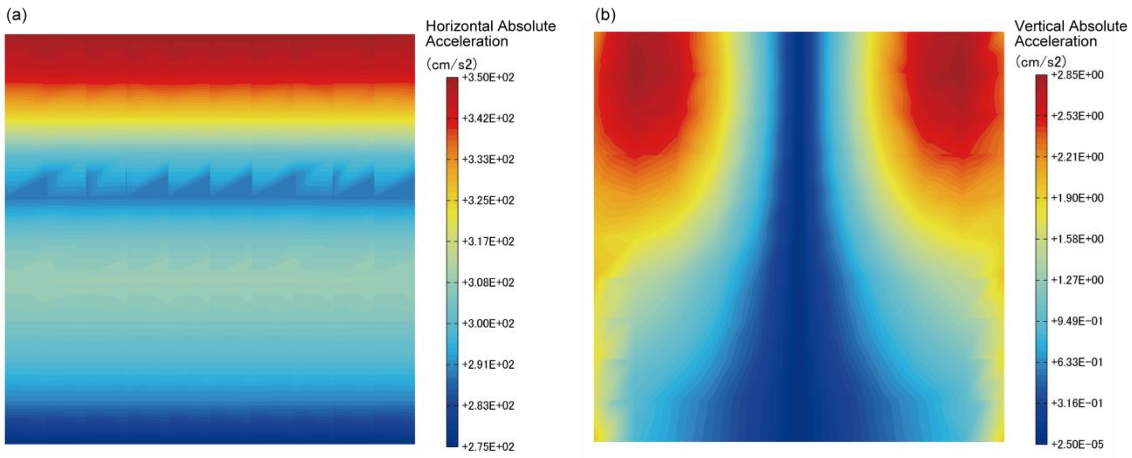

Fig. 4.11 Distribution of the absolute values of acceleration in (a) the horizontal and (b) vertical directions for soil model 1 (10mx10m)

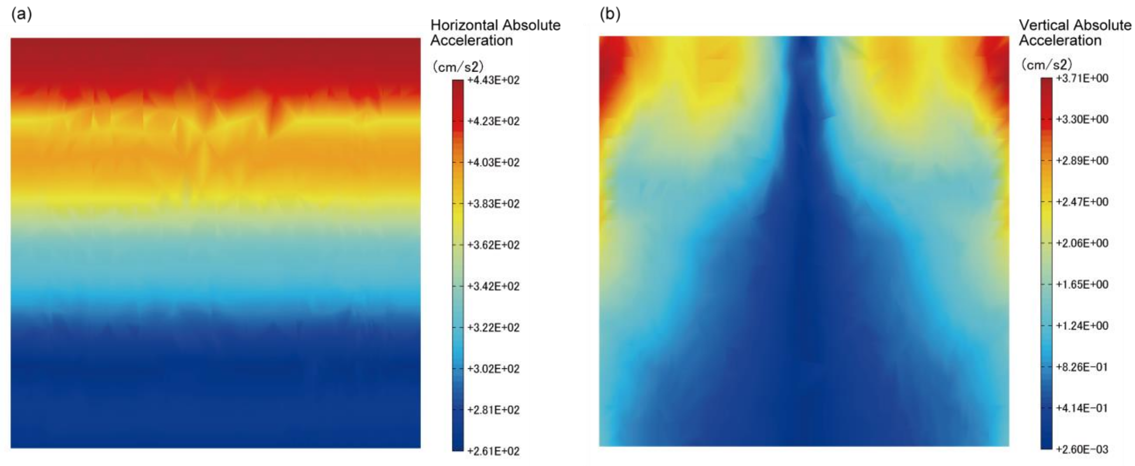

Fig. 4.12 Distribution of the absolute values of acceleration in (a) the horizontal and (b) vertical directions for soil model 2 (20mx20m)

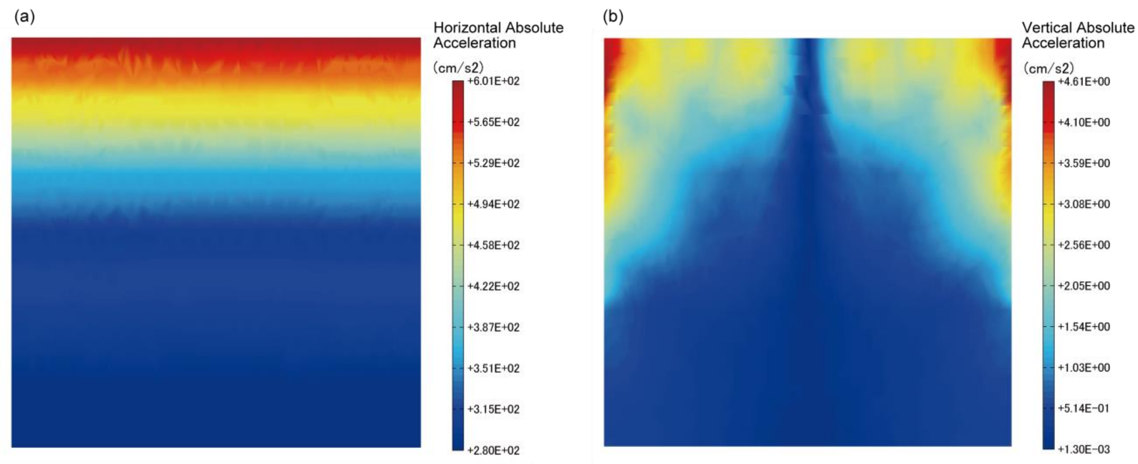

Fig. 4.13 Distribution of the absolute values of acceleration in (a) the horizontal and (b) vertical directions for soil model 3 (30mx30m)

Table 4.7 Absolute values of surface acceleration obtained for the three models in the frequency and time domain

	Surface Acceleration (cm/s^2)			
	FD Analysis	**1D FE Analysis**	**2D FE Analysis**	
			Horizontal	Vertical (max.)
Model 1	348.63	349.25	350.12	2.85
Model 2	435.87	442.05	443.17	3.71
Model 3	611.47	597.73	600.36	4.61

Chapter 5: Seismic Response and Behavior Comprehension

5.1 Preface

This chapter discusses the factors governing the dynamic response of the populated slopes in Villa El Carmen and Lomo de Corvina.

To begin with, a general description of the input motions applied to the developed finite element models is presented. It is important to consider not only waveforms of complex frequency content, such as synthetic motions, but also prescribed-frequency single and cyclic time-histories which might give a clue of the impact of the predominant frequency and its particular influence in the seismic behavior in each case.

Material damping considerations are also introduced with the objective of calibrating the response of representative one-dimensional soil columns with their correspondent theoretical correct answer given in the frequency domain.

It is known that the overall seismic behavior of soil systems with geometric irregularities corresponds to a combination of several factors which make it difficult to differentiate their degree of impact. Therefore, it is important to simplify the superimposed behavior into simpler cases in order to isolate and understand their influence.

It has to be emphasized that the areas under study were deliberately chosen to represent slopes in the opposite ends of the geological and geotechnical spectrum in the city of Lima and, hence, unique response is expected in each case. The cases studied involve the predominant frequency of single- and multiple-wave input motions, generation of surface waves and their correspondent impact, restriction of vibration at specific locations and the analysis of simplified problems, such as basin-shaped models and approximated step-like slopes with homogeneous dynamic properties.

Finally, the sensitivity of the model’s size is also discussed and compared with the resulting trends of the surface response obtained from the originally adopted models.

5.2 Input Motions

Previous studies (Gonzales et al., 2014b, 2017) have dealt with the response of slopes under the effect of synthetic motions of complex frequency content. However, with the objective of separating the effects of frequency, the analysis of Ricker wavelets is additionally included.

5.2.1 Synthetic Accelerogram

Within the framework of the Peru Science and Technology Research Partnership for Sustainable Development (SATREPS) project (Yamazaki and Zavala, 2013), the analysis of a model of interseismic coupling for the Central Andes concluded that the regions in front of the coast of Lima have the potential of being struck by a megathrust earthquake with moment magnitude (M_w) of 8.9. Estimations were performed based on geodetic data and information of historical earthquakes.

Among other factors, the overall procedure included 12 broadband slip models, each of which considered 9 probable starting points of rupture, resulting in a total of 108 slip scenarios for simulations (Pulido et al., 2015). Additionally, synthetic broadcast strong motions were calculated up to the surface at the 8 sites where deep one-dimensional shear-wave velocity profiles are available (Calderon et al., 2012a).

In a subsequent work (CISMID, 2013b), the set of accelerograms obtained for the most critical slip was manipulated with the aim of generating a database whose response spectra, for 5% damping, were compatible with both the expected peak ground acceleration (PGA) and design spectra specified in the Peruvian Building Code for each site.

The matching methodology used an iterative procedure based on the correction of the amplitudes of the Fourier spectrum, in such a way that their spectral amplitudes were congruent with those of the design spectrum and, at the same time, remained the phase information and duration of the original signal unaltered. Shallow site effects were included by means of the amplification factors, with respect to the engineering bedrock ($V_S \approx 500$m/s), calculated in Sekiguchi et al. (2013).

Matched synthetic accelerograms were available at the surface of both CSM and VSV profiles and were considered in this analysis due to their closeness to the areas under study (two-dimensional profiles C-C' and B-B', respectively). Deconvolution of the surface motions corresponding to the east-west components at each site was performed down to the semi-infinite bottom layer using the V_S information of the modified CSM* and VSV* profiles. This resulted in motions with PGA of about 200cm/s^2, as observed in Fig. 5.1 and Fig. 5.2 for Villa El Carmen and Lomo de Corvina, respectively.

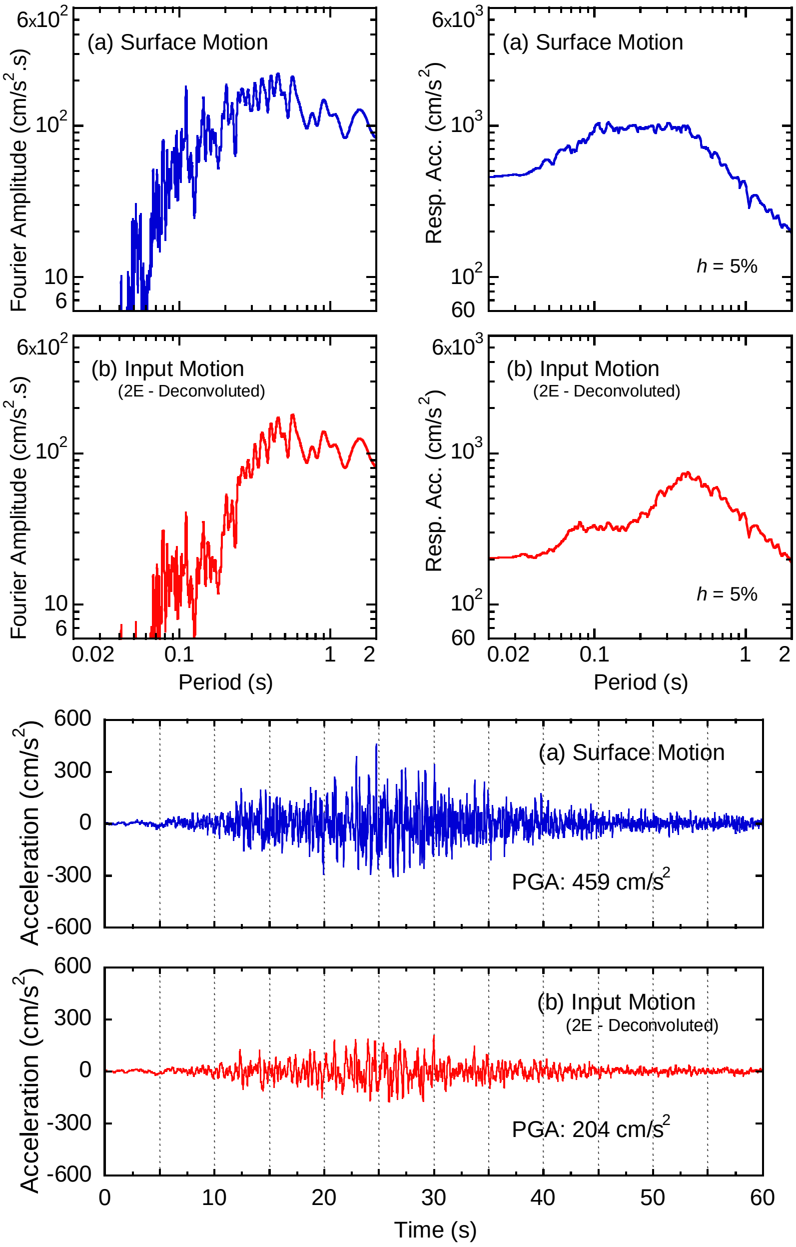

Fig. 5.1 Fourier spectrum, response spectrum and acceleration waveforms for (a) surface motion and (b) deconvoluted bottom (input) motion for Villa El Carmen (CSM*)

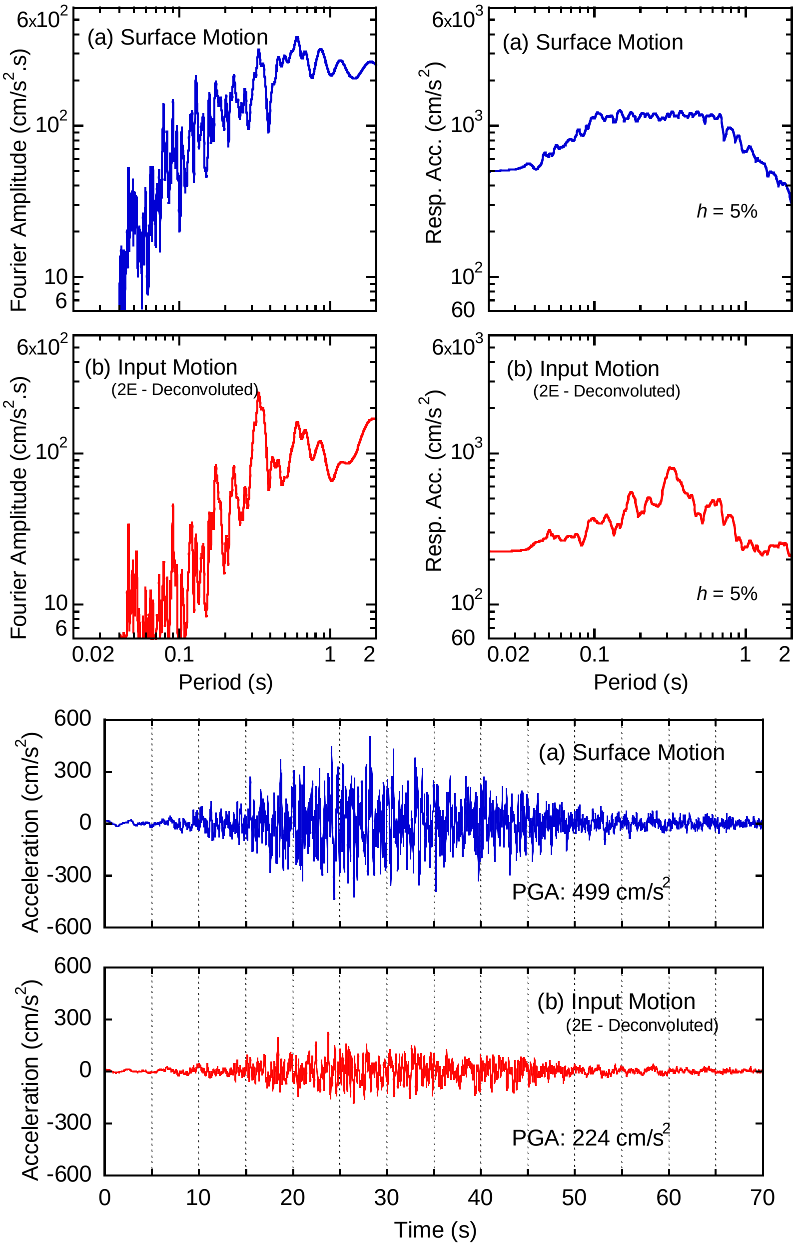

Fig. 5.2 Fourier spectrum, response spectrum and acceleration waveforms for (a) surface motion and (b) deconvoluted bottom (input) motion for Lomo de Corvina (VSV*)

5.2.2 Ricker Wavelets

With the objective of a deep understanding of the propagation mechanism in the target areas, the generated finite element models were additionally subjected to input motions of well-defined frequencies in the form of Ricker wavelets (Ricker, 1952), whose formulation in the time domain is defined as

$$r_{(t)} = \left(1 - \frac{1}{2}\omega_P^2 t^2\right) \exp\left(-\frac{1}{4}\omega_P^2 t^2\right) \tag{5.1}$$

where ω_P is the most energetic circular frequency.

In addition, in the circular frequency domain, the Fourier transform of certain Ricker wavelet can be expressed as (Wang, 2015)

$$R_{(\omega)} = \frac{2\omega^2}{\sqrt{\pi}\omega_P^3} exp\left(-\frac{\omega^2}{\omega_P^2}\right) \tag{5.2}$$

Ricker wavelets of unit amplitude were used in this study. Table 5.1 lists the most energetic ordinary frequencies, as well as their respective time shift, of the chosen wavelets whose waveforms are presented in Fig. 5.3.

Table 5.1 Most energetic frequencies and time shifts for the utilized Ricker wavelets

Most Energetic Frequency (Hz)	**Time Shift (s)**
1	2.0
2	1.0
4	0.60
10	0.40

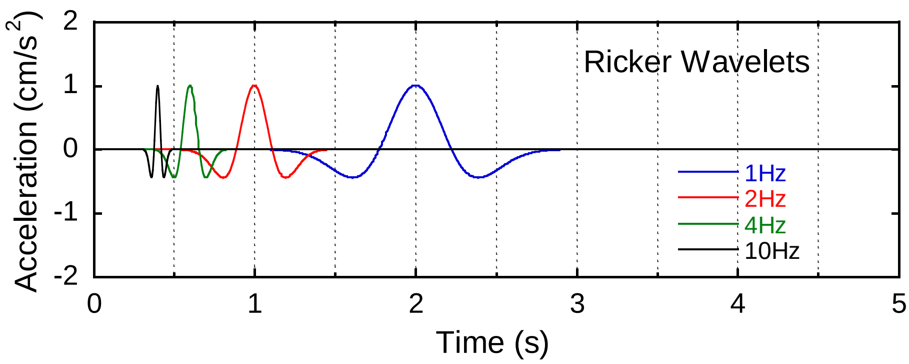

Fig. 5.3 Ricker wavelets used as horizontal acceleration input motions (SV-waves) in this study

5.2.3 Cyclic Motion

The analysis of the effects of input motions consisting of single waves of prescribed frequency, such Ricker wavelets, allows the understanding of the propagation phenomenon only. In a real complex motion, it is typical to observe interference between the generated body and surface waves along the slope surface which might lead to a substantial variation in the response and, therefore, the study of cyclic motions with characteristic frequencies is included in this work.

In order to accomplish the mentioned above, a typical sinusoidal wave of unit amplitude and well-defined eight cycles was adopted as a vertically propagating SV-wave. Subsequently, the waveform was modulated in its amplitude with the objective of avoiding the generation of appreciable high-frequency content due to the abrupt change at the beginning of the time-history representation. Thus, a pattern cyclic motion is represented as

$$f_{(t)} = A_{(t)} \sin(\omega t) \tag{5.3}$$

where $\omega = 2\pi f$ contains the characteristic frequency of the adopted sinusoidal wave and $A_{(t)}$ is called the message function, which in turn is formulated as

$$A_{(t)} = \frac{1 - \cos(\omega_m t)}{2} \tag{5.4}$$

An appropriate relationship between the circular frequency of the message function, ω_m, and that for the modulated waveform, ω, defines the number of cycles that the signal requires to be fully stabilized. In this case, a number of four cycles was adopted as it can be seen in the typical cyclic waveform represented in Fig. 5.4.

The analyses were performed at frequency values similar to those adopted in the case of Ricker wavelets, i.e. 1, 2, 4 and 10Hz, with the time shift fixed at 1s for all signals and variable duration that guarantees the fully formation of surface waves. Finally, Fig. 5.4 also shows that the coda part of the sinusoidal wave was kept unaltered since, as it will be seen in the following sections, it does not have a strong impact in the overall generation of surface waves.

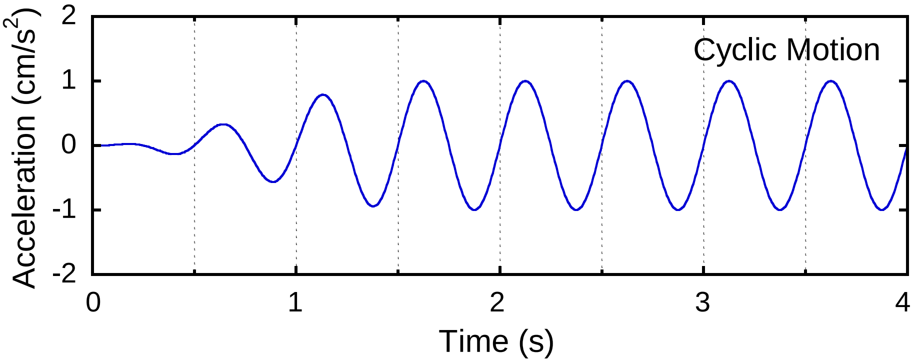

Fig. 5.4 Typical cyclic motion utilized throughout this study

5.3 Material Damping

It is well-known that in linear analysis, viscous damping can be considered as the main source of the total material damping. Thus, in the general time-domain expression (Eq. 4.18), damping matrix, $\mathbf{C}$, is derived from the formulation proposed by Rayleigh and Lindsay (1945) which considers contributions of the mass, $\mathbf{M}$, and stiffness, $\mathbf{K}$, matrices and that, expressed in terms of element variables, is written as

$$\mathbf{C}^e = \alpha_R \mathbf{M}^e + \beta_R \mathbf{K}^e \tag{5.5}$$

where α_R and β_R are the Rayleigh coefficients.

It is common practice to simplify the damping matrix formulation to be only stiffness proportional since it was encountered that, in most cases, the value of $\alpha_R \mathbf{M}^e$ is small compared to $\beta_R \mathbf{K}^e$. Therefore,

$$\mathbf{C}^e = \beta_R \mathbf{K}^e \tag{5.6}$$

and

$$\mathbf{C}^e = \frac{2\xi}{\omega_1} \tag{5.7}$$

where ξ is the viscous damping ratio and ω_1 is the natural circular frequency of the soil system considered.

However, it was found that the above simplified formulation adds excessive unrealistic damping that may filter out high-frequency components of the motion utilized (Hashash and Park, 2002). This effect increases with the depth of the soil model considered since the influence of higher modes in the computation rises as well as the contribution of the α_R term. Therefore, in the current analysis, the so-called full Rayleigh damping in Eq. (5.5) was adopted.

Values of α_R and β_R can be computed using the frequencies and damping ratios for two significant modes *m* and *n* (Clough and Penzien, 2003) by means of

$$\begin{bmatrix} \xi_m \\ \xi_n \end{bmatrix} = \frac{1}{2} \begin{bmatrix} \dfrac{1}{\omega_m} & \omega_m \\ \dfrac{1}{\omega_n} & \omega_n \end{bmatrix} \begin{Bmatrix} \alpha_R \\ \beta_R \end{Bmatrix} = \frac{1}{2} \begin{bmatrix} \dfrac{1}{2\pi f_m} & 2\pi f_m \\ \dfrac{1}{2\pi f_n} & 2\pi f_n \end{bmatrix} \begin{Bmatrix} \alpha_R \\ \beta_R \end{Bmatrix} \tag{5.8}$$

After solving the above system of equations, the following is obtained

$$\alpha_R = 4\pi f_m f_n \left(\frac{\xi_n f_m - \xi_m f_n}{f_m^2 - f_n^2} \right) \tag{5.9}$$

$$\beta_R = \frac{1}{\pi} \left(\frac{\xi_m f_m - \xi_n f_n}{f_m^2 - f_n^2} \right) \tag{5.10}$$

Since the damping ratio for certain soil layer, ξ_i, can be treated as a quantity independent of the frequency, an identical value, ξ, can be assumed for the two considered frequencies. Therefore,

$$\alpha_R = \frac{4\pi f_m f_n \xi}{(f_m + f_n)} \tag{5.11}$$

$$\beta_R = \frac{\xi}{\pi(f_m + f_n)} \tag{5.12}$$

Frequency dependency of the above Rayleigh formulation is sensitive to the selection of the frequencies that define the damping function. A series of iterative one-dimensional linear wave propagation analyses are recommended to be performed in order to help in the election of the optimum values of frequencies f_m and f_n (Park and Hashash, 2004). Thus, results obtained from finite element analysis in the time domain are sought to match those in the frequency domain that are considered as the correct answers since this type of analysis is based on a closed-form solution (Kramer, 1996).

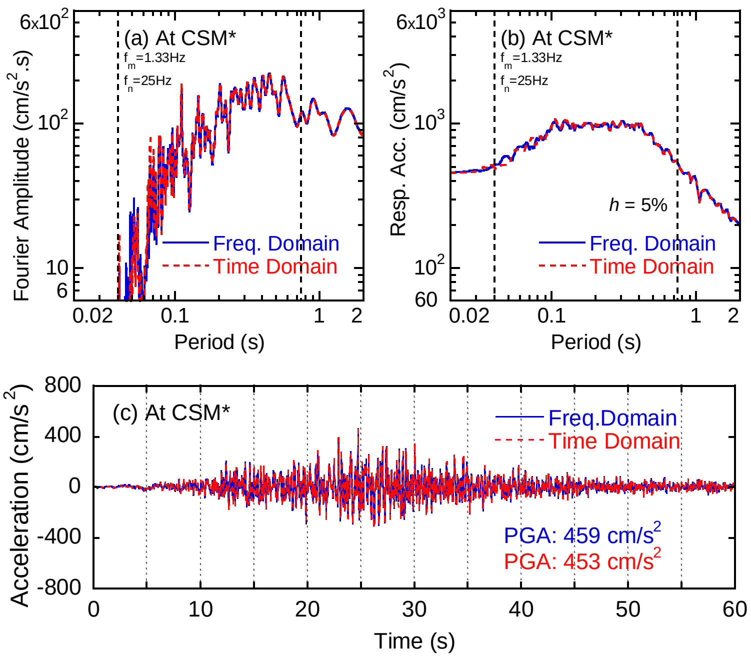

Fig. 5.5 (a) Fourier spectra, (b) acceleration response spectra and (c) acceleration waveforms obtained from frequency and time domain analyses at Villa El Carmen (CSM*)

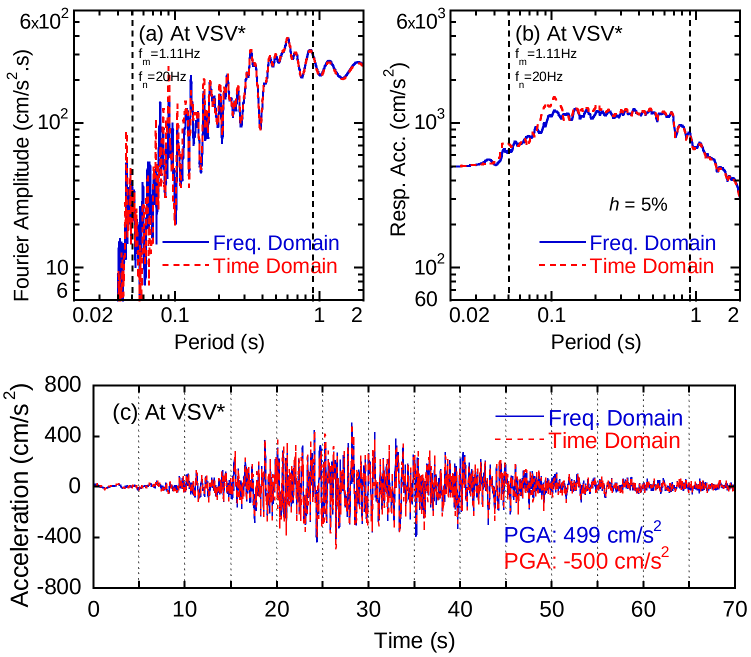

Fig. 5.6 (a) Fourier spectra, (b) acceleration response spectra and (c) acceleration waveforms obtained from frequency and time domain analyses at Lomo de Corvina (VSV*)

The procedure was performed in the soil columns corresponding to CSM* and VSV*, whose properties are listed in Table 4.1–4.2 and Table 4.3–4.4, respectively, and includes the comparison of the peak ground acceleration (PGA), Fourier and acceleration response spectra, for 5% damping, of the original synthetic motions with those obtained at the surface for their respective deconvoluted motions as input. After several trials, the most suitable values of frequencies f_m and f_n were found at 1.33Hz and 25Hz for CSM* (Fig. 5.5), whereas for VSV*, values of 1.11Hz and 20Hz were adopted (Fig. 5.6).

5.4 Dynamic Response of Villa El Carmen

A preliminary analysis of the response of the slope in Villa El Carmen was conducted in Gonzales et al. (2014b) for the synthetic accelerogram prior the matching to the Peruvian Building Code mentioned in Section 5.2.1. Complementary computations are presented which aim to understand the complex seismic behavior of the typical rocky slope adopted.

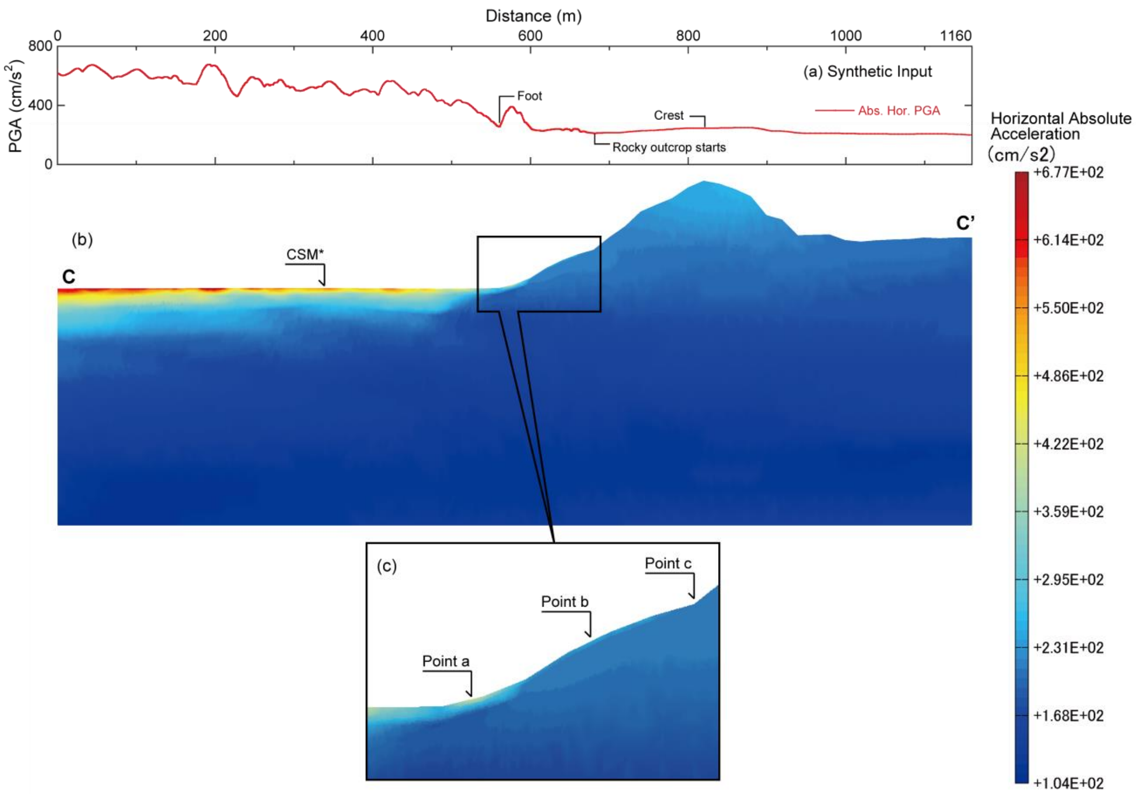

Fig. 5.7 (a) Absolute horizontal PGA, (b) distribution of the horizontal absolute acceleration and (c) zoom view close to the foot of the slope in Villa El Carmen

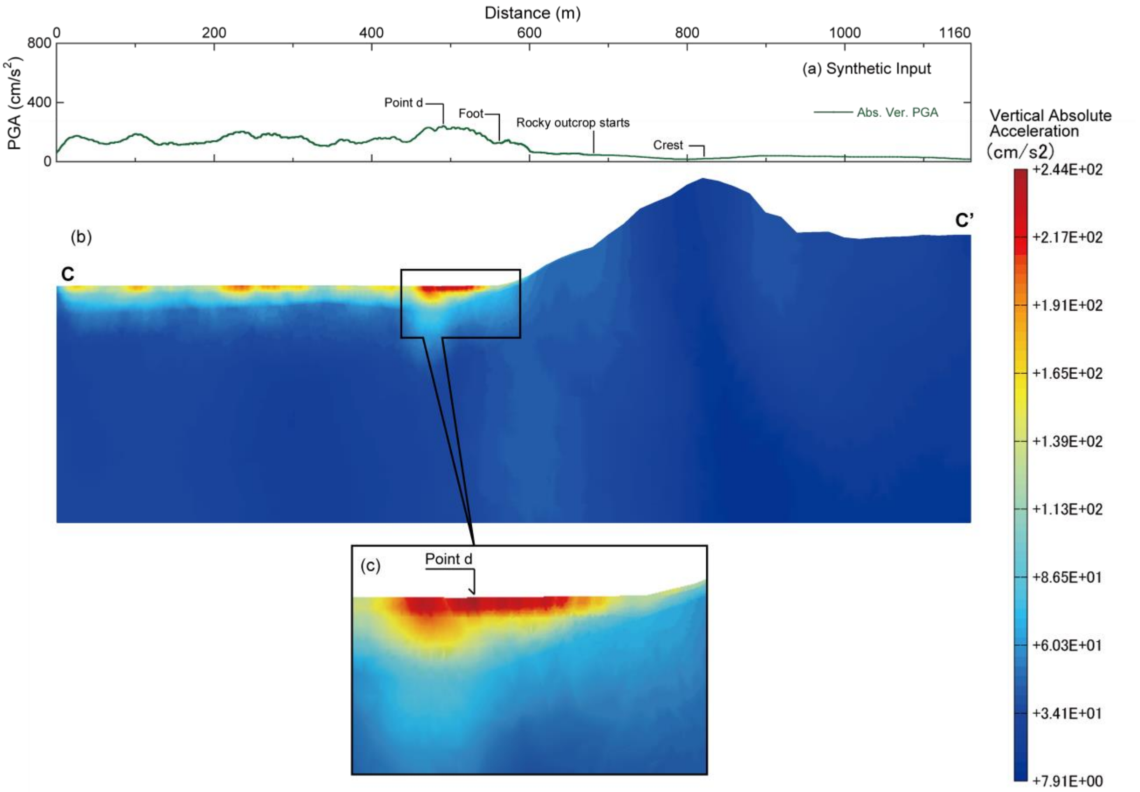

Fig. 5.8 (a) Absolute vertical PGA, (b) distribution of the vertical absolute acceleration and (c) zoom view of the area of maximum values close to the foot of the slope in Villa El Carmen

5.4.1 Synthetic Response

Results of the absolute values of both horizontal and vertical accelerations are shown in Fig. 5.7 and Fig. 5.8, respectively, for the case in which the deconvoluted accelerogram shown in Fig. 5.1 was applied as input motion, in the horizontal direction (SV-wave), at the bottom of the finite element model generated for the foothill in Villa El Carmen.

Values of absolute horizontal peak ground acceleration (PGA) in Fig. 5.7a evidence an irregular increment towards the left boundary of the model, whereas lower values tend to stabilize for the areas in which full rocky outcrop was assumed.

From the information given in Fig. 5.7b, it can be observed that at first glance, the overall distribution pattern of horizontal acceleration is mainly affected by the fact that most parts of the model are composed of very stiff materials and that the large values close to the left boundary can be attributed to the shallow soft materials deposited there.

The above aspect is also evident when analyzing the lower region of the populated slope, such those shown in the zoom view in Fig. 5.7c. In this area, slightly larger values are found in the vicinities of the foot due to the impedance contrast between soft layers, corresponding to borrowed soils (V_S = 176m/s) and the shallow layer in flat areas (V_S = 384m/s), and stiffer materials (V_S = 1623m/s). This effect becomes almost negligible on the direction to the top of the slope due to the disappearance of the intermediate layer resulting in borrowed materials directly overlying fractured rock.

Complementary computations to corroborate the aforementioned were performed. That included the extraction of waveforms in three points where low-quality housing was massively developed: Point a, with the largest absolute value of horizontal PGA for regions close to the foot of the slope; Point b, in the center of the areas covered by borrowed soil and Point c, where it was assumed that full outcropping of fresh rock starts. In addition, one-dimensional amplification analyses were conducted for each of the three points previously mentioned, in which a soil column with the same mechanical and dynamic properties was analyzed and solved in the time domain as well.

Comparison of the results obtained for both type of analyses (Fig. 5.9) indicate a minor decrease in the response for Points a and b, when considering the influence of the geometric irregularity, whereas a slight increment was found for Point c only. Similar trend was detected when the system was solved for the original synthetic waveform as input motion (Gonzales et al., 2014b). This behavior appears as a result of the apparent restricted vibration close to the foot of the slope caused by the massive stiff rocky hill next to the flat area.

On the other hand, Quiroz (2014) have concluded that both PGA and response acceleration can be adopted as key factors in the estimation of the structural damage in Peru. Therefore, comparisons of the acceleration response spectra are also shown (Fig. 5.9b), in which a peak could be observed for Point a in the vicinity of a period value of 0.075s. Since one-story masonry houses and other essential structures (schools, community centers, etc.) are extensively constructed in that area, an increase in their seismic response is expected due to the similarity of their natural periods of vibration (Proaño and Zavala, 2003) with the value mentioned above.

The effect of the inclusion of the topographical irregularity in computations was also evaluated for the flat area next to Villa El Carmen. Concentrated zones with the highest horizontal and vertical PGA (Fig. 5.7b,

Fig. 5.8b) suggest the joint influence of body and surface waves. Two types of interference are likely to exist: the first one, referred to as positive interference, might occur when waves which are in-phase build up their combined amplitudes and the second one, called destructive interference, may appear in out-of-phase waves deamplifying their global response.

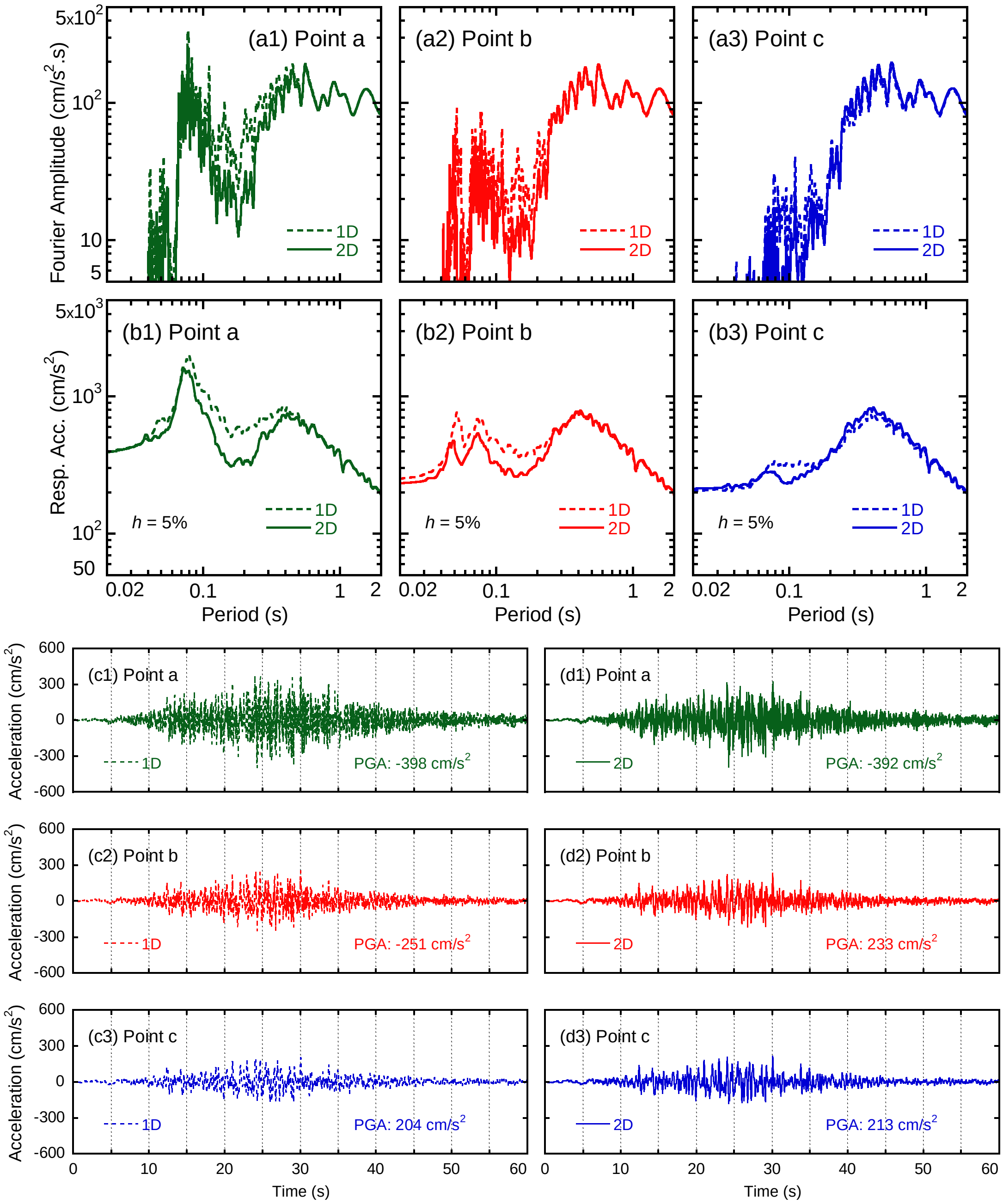

Fig. 5.9 Comparison of the Fourier spectra (a1-3), acceleration response spectra (b1-3) for 1D and 2D FE analyses. Acceleration waveforms for 1D (c1-3) and 2D (d1-3) FE analyses for three points in the populated sloping area of Villa El Carmen

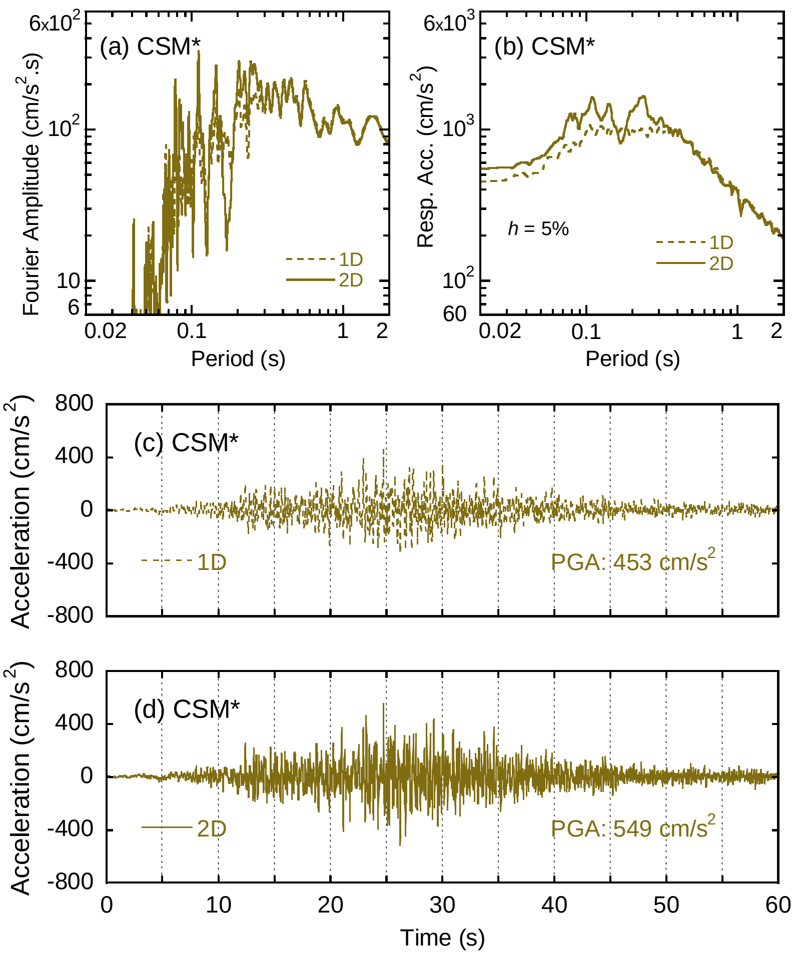

Fig. 5.10 Fourier spectra, acceleration response spectra and horizontal acceleration waveforms obtained from one and two-dimensional analyses at CSM*

A representative point in the flat area, corresponding to CSM*, was chosen and a similar procedure to that for points in the slope was done. In this case (Fig. 5.10), increment of about 20% in the horizontal PGA was encountered for the two-dimensional analysis, as well as the values of Fourier amplitude and in the response spectrum for short periods, evidencing a constructive interference in this particular location. The foregoing effect of the stiff rocky body seems to decrease towards the flat areas and surface waves coming from the irregularity are likely to affect the response. Analysis of the generation of surface waves for the model under consideration will be conducted for simpler prescribed-frequency input motions in Section 5.4.2.

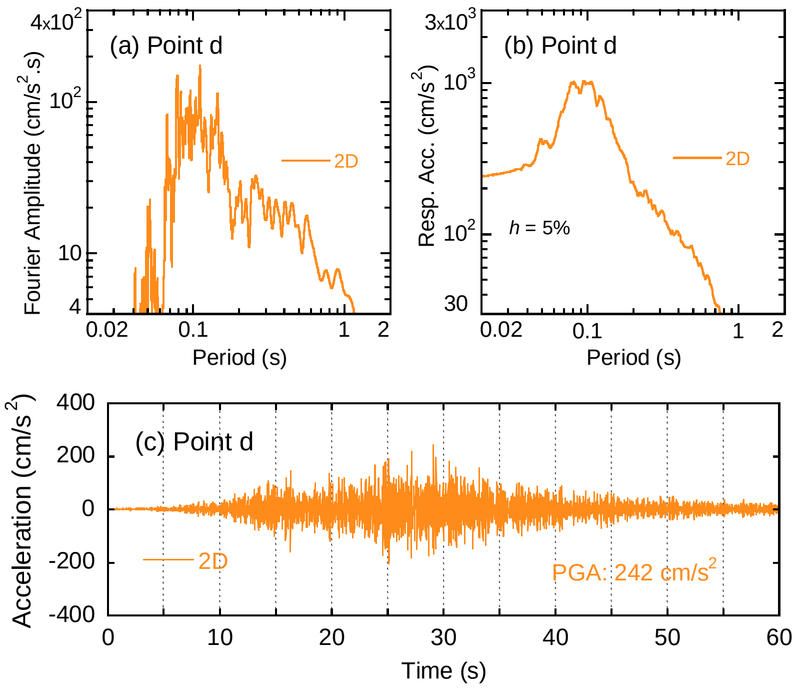

Fig. 5.11 (a) Fourier spectrum, (b) acceleration response spectrum and (c) waveform of the maximum surface vertical acceleration (Point d) obtained by two-dimensional analysis in Villa El Carmen

Finally, in case of the distribution of the vertical absolute acceleration (Fig. 5.8b), as expected, low values are observed in the rocky areas which increase on the left side of the model. Surficial values of acceleration follow an irregular punctual pattern that may suggest an influence of surface waves in their generation. Results for the extracted waveform at the point of maximum vertical surficial acceleration (Point d) can be observed in Fig. 5.11, which mostly concentrates its components within a short period range and reaches a considerable value of about 240cm/s^2.

5.4.2 Effect of the Most Energetic Frequency

In order to isolate the effect of the predominant frequency of the input motion in the response of the slope in Villa El Carmen, its corresponding finite element model was horizontally subjected to Ricker wavelets of unit amplitude whose prescribed frequencies are detailed in Section 5.2.2.

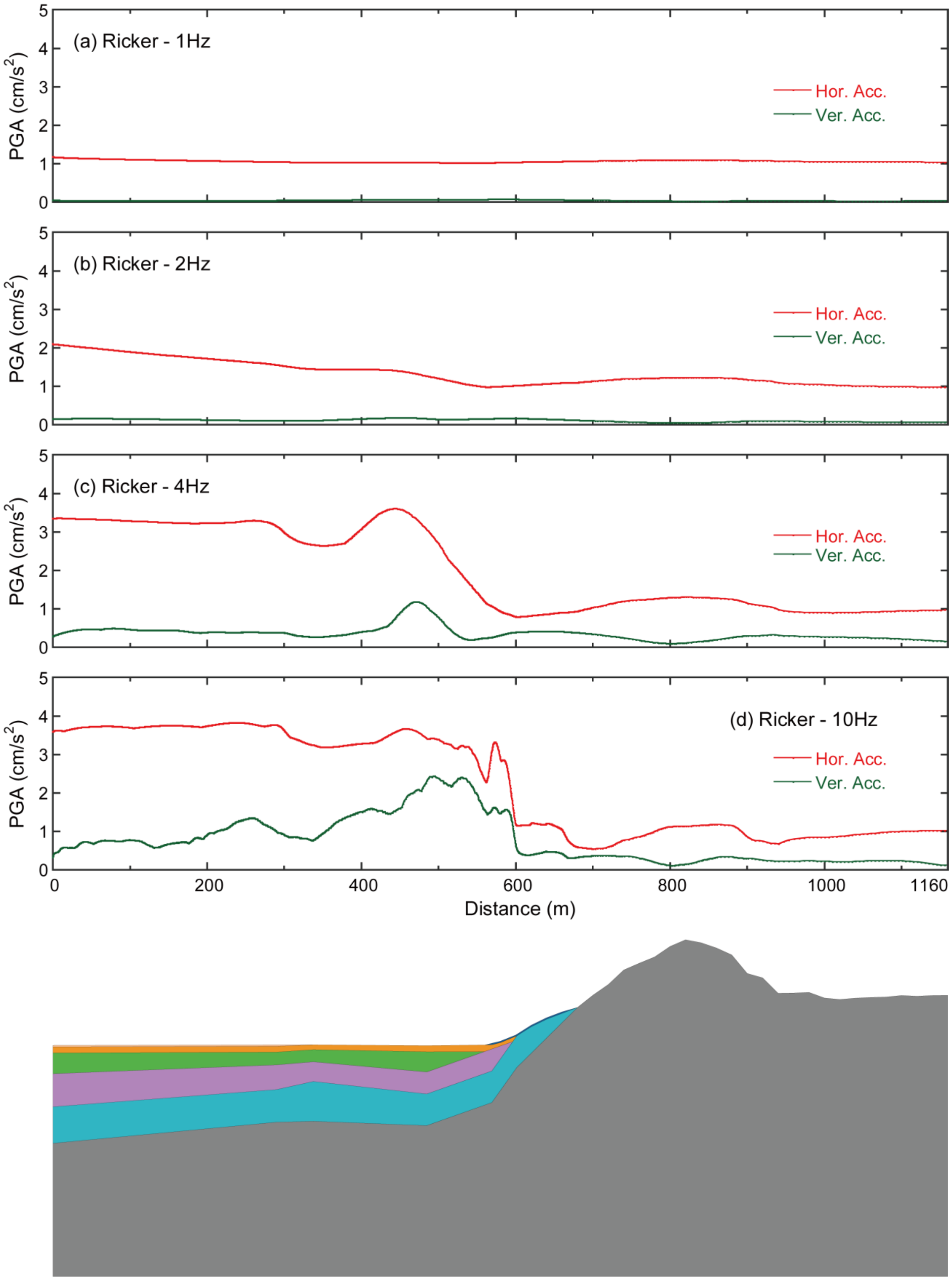

Fig. 5.12 Variation of the peak ground acceleration for different input motions (Ricker wavelets) in Villa El Carmen

Results of the peak ground acceleration (PGA) along the flat and sloping areas are presented in Fig. 5.12. In particular, the horizontal motion of 1Hz is not amplified throughout the surface and only negligible vertical components are generated (Fig. 5.12a). The effect slightly intensifies in case of a Ricker wavelet of 2Hz with an increment of the horizontal motion towards the left boundary of the model (Fig. 5.12b).

A drastic change in the PGA distribution appears when considering high-frequency motions. In relation to 4Hz (Fig. 5.12c), alterations in the trend for horizontal and vertical components appears close the foot of the slope with a maximum value formed at the surface point corresponding to the start of the slope change in the underground structure.

Finally, for the highest frequency considered (10Hz), an abrupt sharper increment in the acceleration distribution was encountered (Fig. 5.12d), with a local peak occurring for the horizontal component in a similar location to that in the case of synthetic motion (Fig. 5.7a).

From the above discussion, it is evident that high-frequency motions can explain in a better way the surface acceleration tendencies when dealing with input motions of more complex frequency content and, therefore, have a greater impact in the overall behavior of the populated areas in Villa El Carmen.

5.4.3 Surface Wave Generation

Acceleration distributions for 4Hz and 10Hz input Ricker waves are presented in Fig. 5.13 and Fig.5.14, respectively. It is clearly seen that irregular soil layering affects the horizontal motion in the flat areas for both frequencies aggravating the one-dimensional response, such as for CSM* (Fig. 5.7b, Fig. 5.10). This type of ‘basin effect’ is made manifest through the appearance of considerable values of vertical acceleration which suggests the generation of surface waves travelling from the basin edge at the foot of the slope.

Another way to address the surface wave problem is through the vibration properties of the soil under analysis. It is known that, for the same exciting energy, high-frequency surface waves present larger amplitudes when compared to those of low frequency which are affected by stiff deep layers, being the boundary frequency to start considering this effect the soil natural frequency.

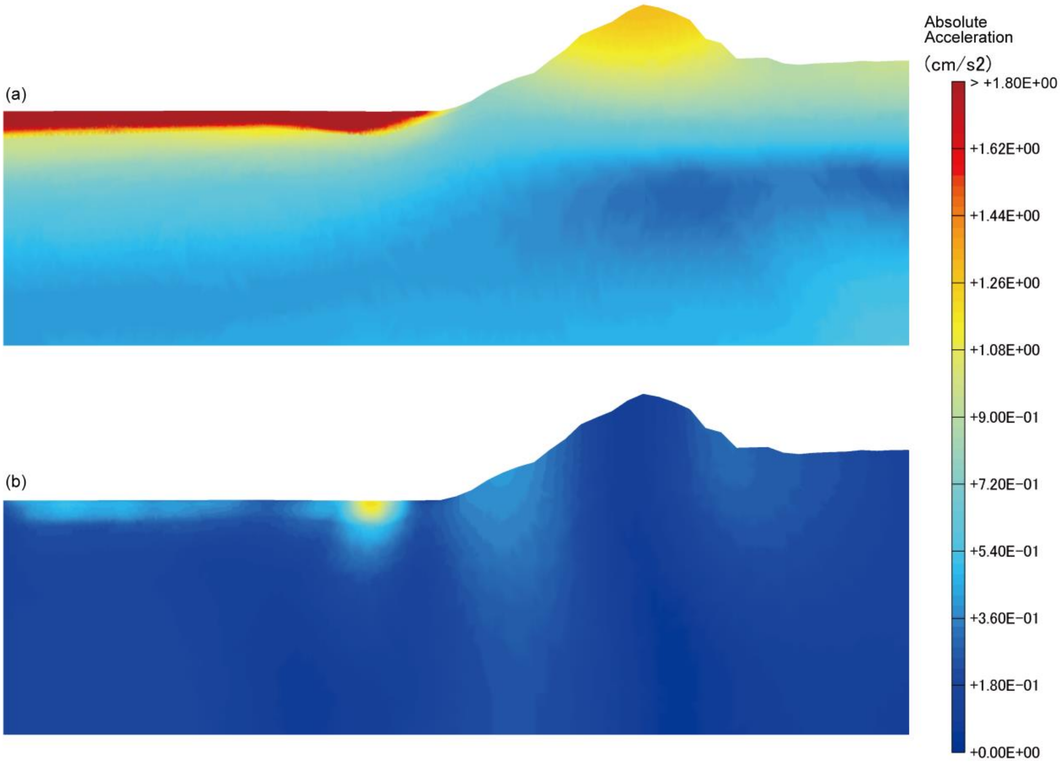

Fig. 5.13 Distribution of absolute (a) horizontal and (b) vertical acceleration (4Hz Ricker motion)

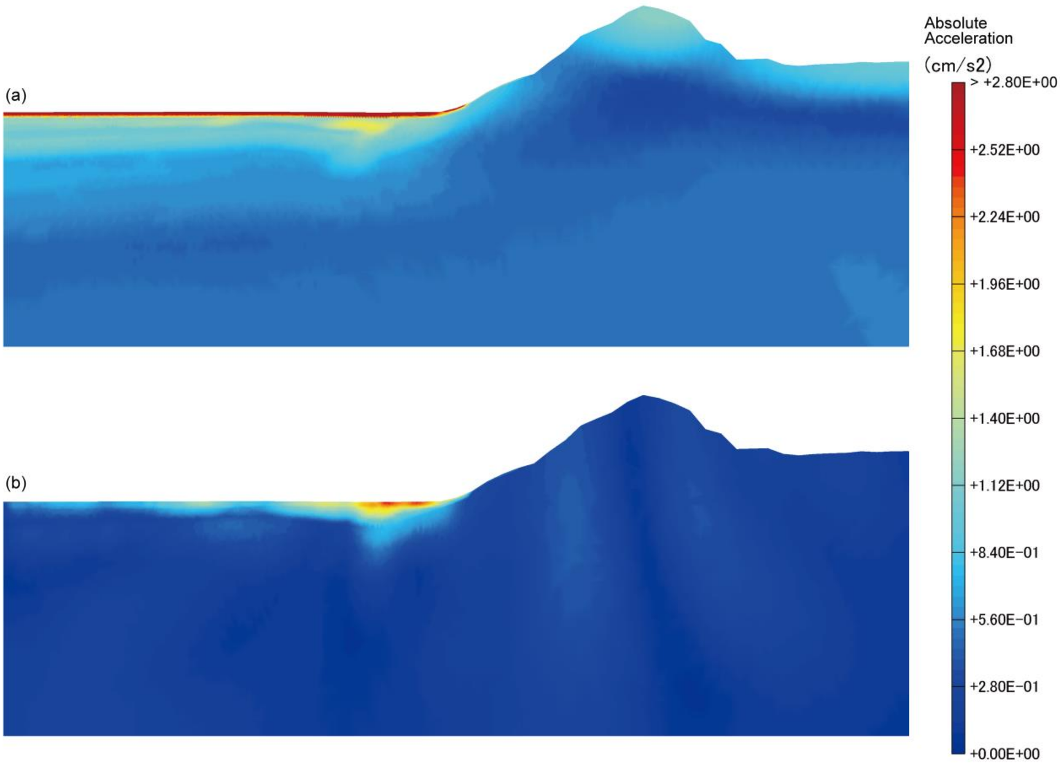

Fig. 5.14 Distribution of absolute (a) horizontal and (b) vertical acceleration (10Hz Ricker motion)

The transfer function which corresponds to the soil column at the left boundary of the model is shown in Fig. 5.15a. In accordance with the aforementioned, surface waves of considerable amplitude are generated for frequencies higher than 4Hz, as it can be observed in the coda of the extracted waveforms for 4Hz (Fig. 5.15b) and 10Hz (Fig. 5.15c).

A more general perspective of surface waves can be reached through the analysis of the vertical wavefield for 10Hz input illustrated in Fig. 5.16. While the response in the rocky foothill remains almost unaltered, the areas in the flat part are affected by a combination of vertically propagated body waves and surface waves generated at the irregular edges of the soil substructure travelling towards the left boundary.

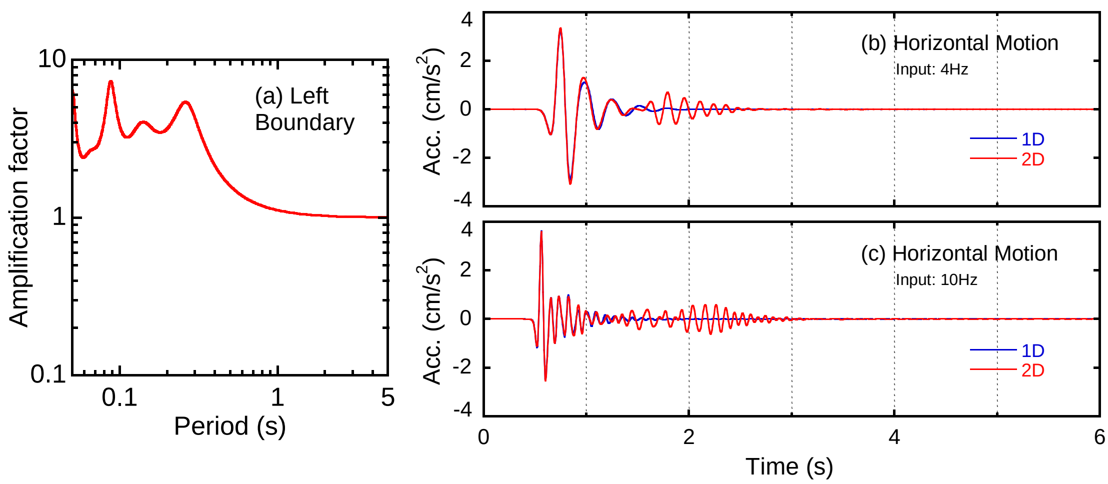

Fig. 5.15 (a) Transfer function, (b) waveforms for 4Hz input and (c) waveforms for 10Hz input at the surface point of the left boundary

5.4.4 Restrained Motion

Generation of surface waves and their subsequent interaction with body waves, in the form of positive and destructive interference, is of significant impact when an input motion consisting of several cycles is studied, such as in the results for synthetic motion presented in Section 5.4.1.

In case of Ricker wavelets of a single cycle, the degree of motion control due to the inclusion of a topographical irregularity can be evaluated. Crucial zones to be considered are those corresponding to the foot and crest of the slope, as their boundary conditions are altered by the addition or exclusion of surrounding soil areas, which might lead to appreciable response differences when compared with the results for a vertical propagating wave in one-dimensional soil columns.

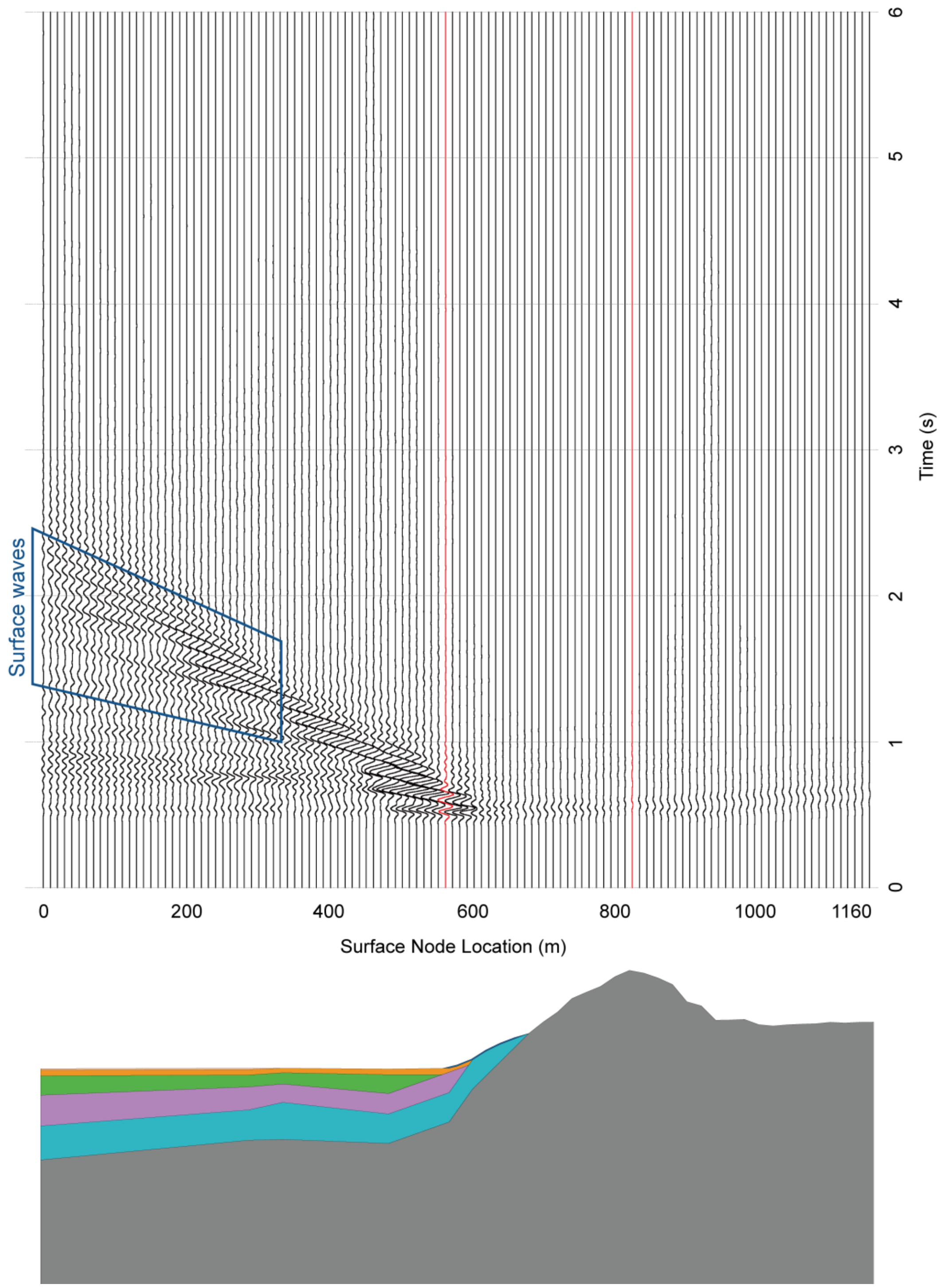

Fig. 5.16 Surface vertical acceleration wavefield corresponding to a 10Hz Ricker wavelet input for Villa El Carmen (red lines correspond to the foot and crest of the foothill)

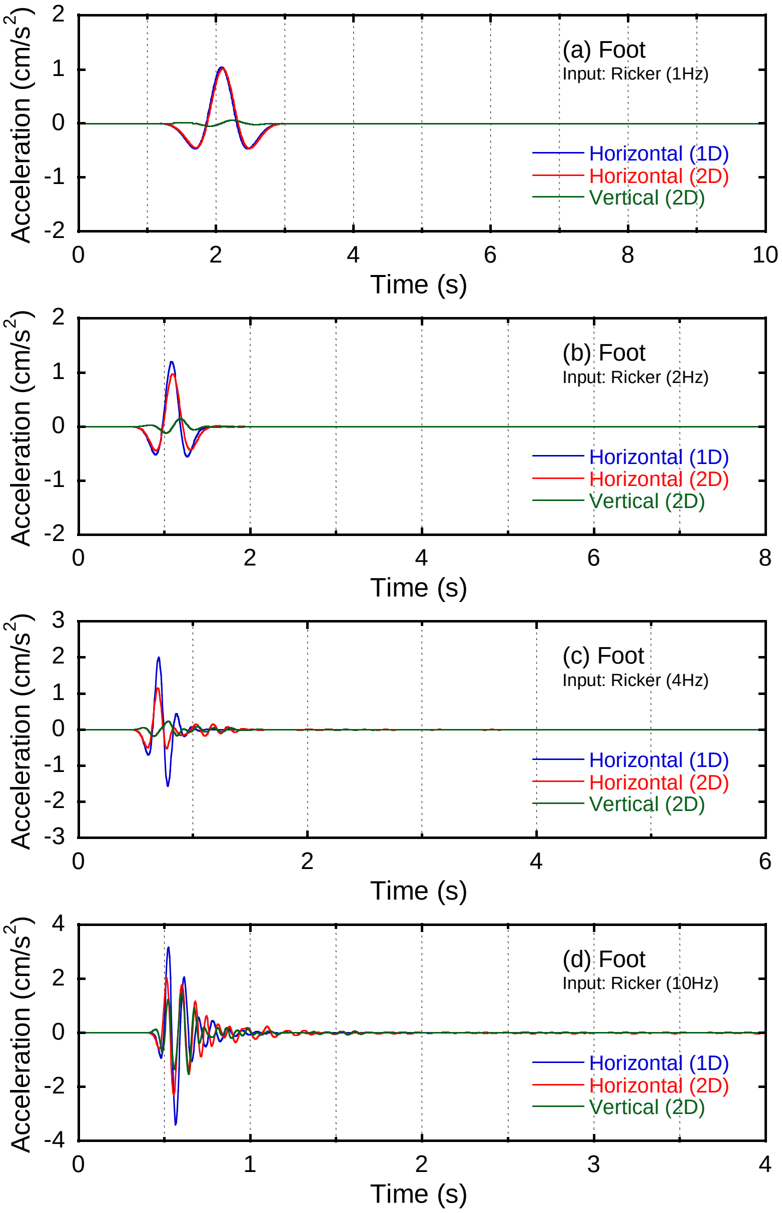

Fig. 5.17 Waveforms at the foot of the slope in Villa El Carmen for different Ricker wave inputs

Fig. 5.17 shows the acceleration waveforms obtained at the foot of the slope for Ricker inputs of different energetic frequencies. By the comparison of the horizontal components obtained from one and two-dimensional analyses, it is evident that restriction of motion affects the total range of frequencies considered and becomes more significant for the higher ones, reaching values of amplitude reduction of about 40%. In case of vertical motion, its generation becomes more noticeable while increasing the frequency which is consistent with the nature of surface waves described in the previous section.

With regard to the crest of the slope, it is a general trend that the response amplifies due to more free vibration allowed. However, this is not the case for the slope in Villa El Carmen since high areas entirely consist of very stiff materials which counterbalance the topographic effects causing the difference in response to be negligible. Therefore, in order to avoid misleading conclusions, in addition to the fact that our target area strictly corresponds to the populated areas, waveforms and comparisons for the highest location of the model are not presented.

5.4.5 Simplified Basin-shaped Model

As mentioned in Section 5.4.3, the generation of surface waves close to the foot of the slope in Villa El Carmen is intrinsically connected to its particular geological conditions. This can be defined as a basin-shaped soil structure adjacent to a rigid body rock, which is characteristic not only for the area under study but also for the populated slopes placed along the foothills of the Central Andes in the north part of the city of Lima.

In order to isolate the plane wave propagation problem from the effects of multiple irregular soil layering, which increases the difficulty of the problem by the generation of diverse reflection and refraction paths, the basin-shaped region of the model was assumed to be comprised of an uniform soil material with shear-wave velocity, V_S, of 500m/s, density, ρ, of 1800kg/m^3 and Poisson's ratio, υ, equal to 0.30. In case of the shallow layer with poor properties representing the filled soil in the low areas of the foothill, it was kept as in the original model since it represents a distinctive construction feature of populated slopes contiguous to rocky bodies.

It is known that the propagation of inclined body waves generates reflected and transmitted (refracted) waves when reaching the interface between two media with different dynamic properties. In the specific case of inclined SV-waves with an incident angle i_1 (dark green arrow in Fig. 5.18), since particle motion is induced in the direction perpendicular to the plane of the interface, both reflected and refracted P- (red arrows), SV-waves (light green arrows) are produced. Formation of the aforementioned waves is governed by the Snell's rule which states that

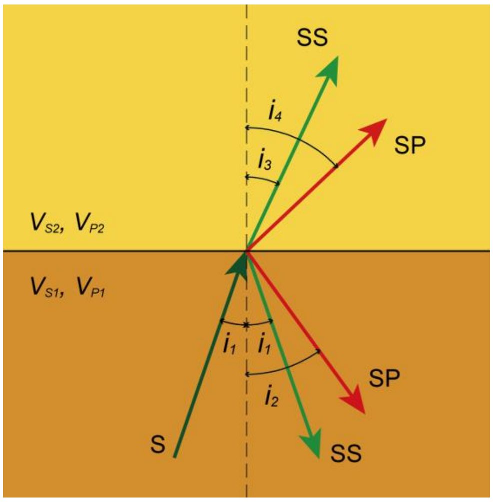

Fig. 5.18 Reflected and refracted P- and SV-waves generated due to the incidence of an inclined SV-wave at the interface between two different media

$$\frac{\sin i_j}{V} = \text{constant} \tag{5.13}$$

where i_j is the angle between the reflected/refracted wave and the normal to the media boundary. The above equation holds for P- and SV-waves and V takes its respective value depending on the type of wave analyzed.

Another aspect to take into account when considering irregular soil layering is the critical angle of incidence. This quantity is independently calculated for each of the reflected P- and refracted P- and SV-waves and determines the inclination angle at which a wave travels parallel to the interface. Waves reaching the boundary at incident angles above this value will travel in the form of inhomogeneous waves whose transmission path, under certain conditions, may derive in the behavior of Stoneley waves along the contact surface between two elastic media.

Due to its comparative simplicity, the simplified basin-shaped model for Villa El Carmen was analyzed by the aforementioned Snell’s rule aiming to understand the effects of the subsurface soil topography in the propagation of vertically incident SV-waves. Fig. 5.19 shows the particular variation in the ray paths for each wave generated at specific contact surfaces in which the color of the arrows follows the convention adopted in Fig. 5.18. As it can be observed, the leftmost boundary alters the incoming waves (dark green arrows) leading to a probable slight interference in the expected response when reaching the surface. With respect to the central boundaries, almost no variation is obtained due to the virtually horizontality of the subsurface. This aspect practically vanishes towards the sloping part where the inclination angles adopt values greater than the critical angle for P-wave reflection. Therefore, inhomogeneous waves appear to travel along the boundary surface. Finally, it has to be mentioned that the effect of the soft shallow layer at the bottom of the foothill mainly correlates with the generation of surface waves propagating in the direction of the flat areas of the model.

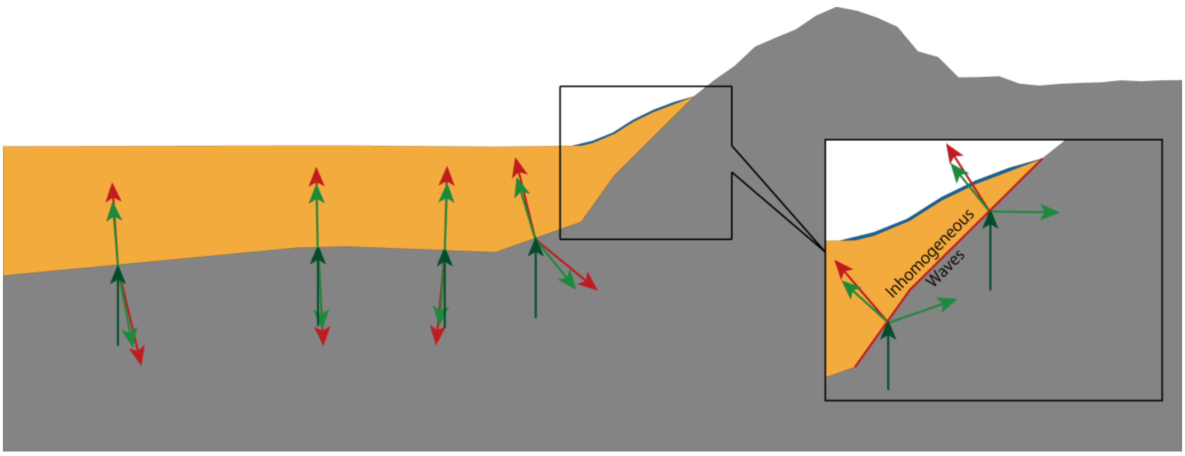

Fig. 5.19 Waves generated at the interface between the rocky body and the basin-shaped simplified stratum

a. Single Motion

The simplified basin-shaped model was subjected to vertically incoming Ricker wavelets whose frequencies were analogous to those utilized for the original adopted model, i.e. 1, 2, 4 and 10Hz. This type of analysis intended to isolate and qualitatively demonstrate the effect of the boundary of the bedrock layer and the slope geometry in the generation of surface waves which, as mentioned in previous sections, is likely to affect the response of the lowlands.

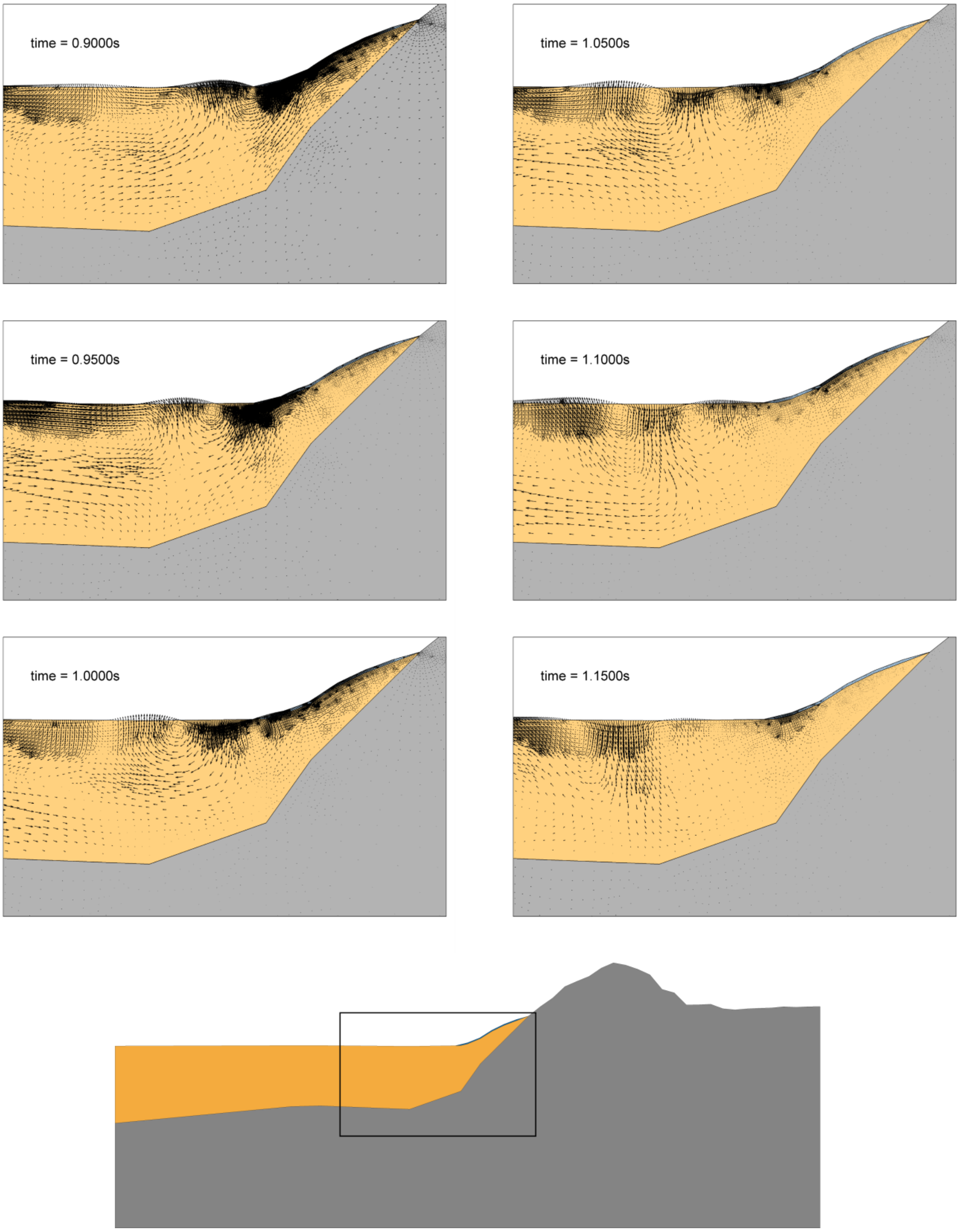

Fig. 5.20 Snapshot sequence of the generation of Rayleigh waves for the simplified basin-shaped model at 4Hz input motion for the specified zoom view

Fig. 5.20 shows a series of snapshots of the acceleration vector at each of the nodal points corresponding to the area close to the bottom of the populated slope for an input Ricker wavelet of 4Hz. This particular value of frequency was chosen since it presents considerable vertical components that make easier to distinguish the propagation of surface waves. In addition, it has to be mentioned that results for some snapshots might appear to have larger amplitudes but that is only a visual misleading effect due to the concentration of nodal points produced during the finite element representation of the soft shallow layer.

Concerning the propagation path governed by the Snell's rule, it is evident that the areas along the surface of the basin-shaped model are first affected by a combination of the P- and SV-waves refracted along the inclined bedrock boundary. Coupling of the aforementioned type of waves and their interaction with the soft shallow layer subsequently produce surface waves in the form of Rayleigh waves in the vicinities of the bottom of the slope. As observed in the snapshot sequence, these generated waves travel down to the foot and towards the left flat part of the model with a characteristic retrograde motion and a calculated phase velocity of about 530m/s which is congruent to the dispersive velocity at 4Hz calculated for a mean soil profile. The above explanation is valid for the complete range of frequencies analyzed and will be of crucial importance when dealing with motions with multiple cycles as explained in the following section.

b. Cyclic Motion

The effect of including more cycles to the input motion of a prescribed frequency was evaluated through analogous analyses conducted for sinusoidal waves whose archetypical waveform was detailed in Section 5.2.3.

With the objective of quantitatively evaluate the impact of the interference of Rayleigh waves, additional calculations for one-dimensional wave propagation were performed for soil columns whose geometrical layering and dynamic properties corresponds to the underlying material at the same discrete surface points were response was calculated in the two-dimensional model. The average spacing of two consecutive considered surface nodes was about 10m.

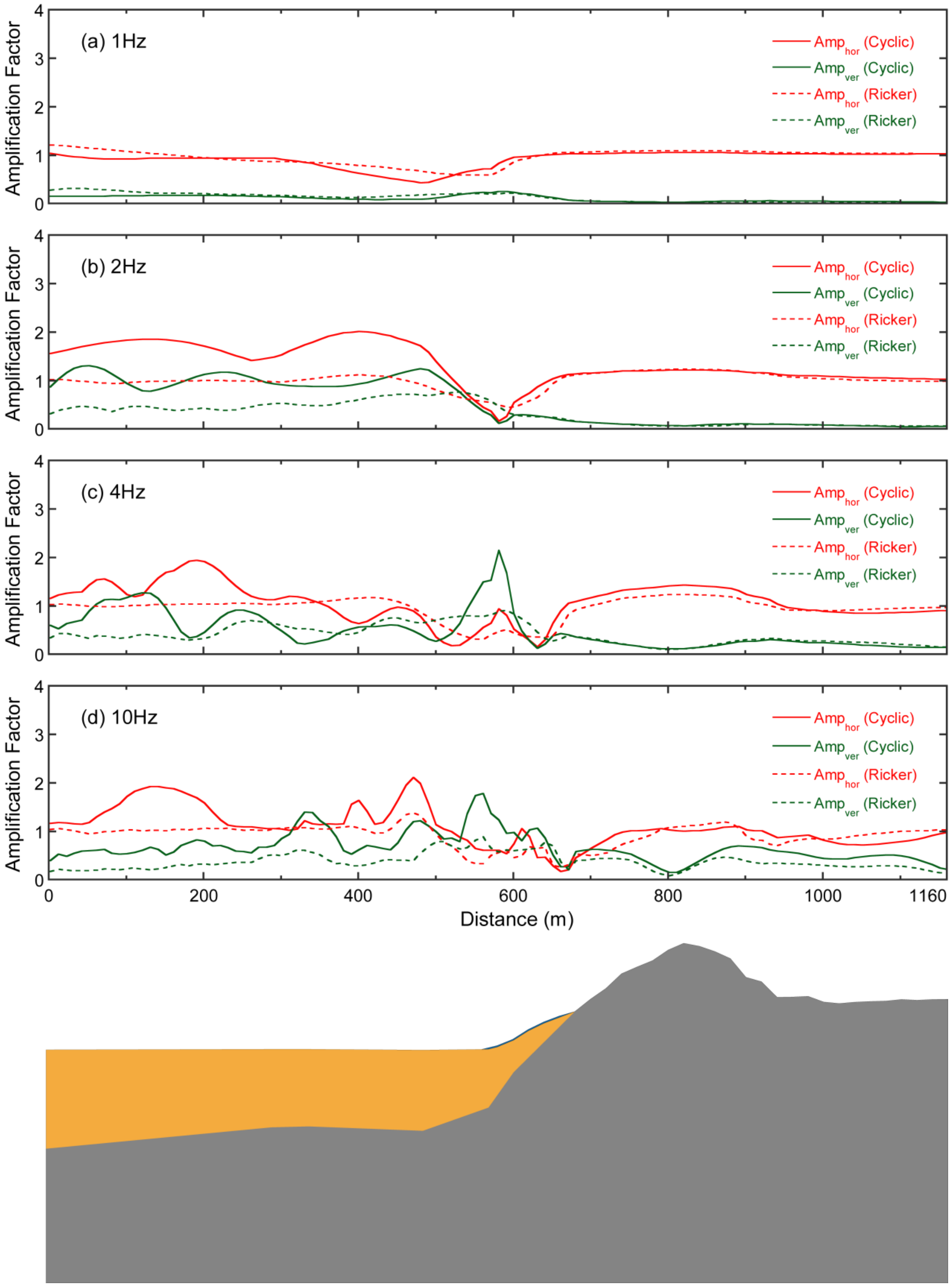

Fig. 5.21 Comparison between the horizontal and vertical amplification factors for Ricker wavelets and cyclic motions for the simplified basin-shaped model

The horizontal and vertical amplification factors at each punctual location along the model surface are respectively defined as

$$\mathrm{Amp}_{\mathrm{hor}} = \frac{\max(acc_{2DH})}{\max(acc_{1D})} \tag{5.14}$$

$$\mathrm{Amp}_{\mathrm{ver}} = \frac{\max(acc_{2DV})}{\max(acc_{1D})} \tag{5.15}$$

where $\max(acc_{2DH})$and $\max(acc_{2DV})$ are the maximum absolute values of the horizontal and vertical surface accelerations for the two-dimensional model, whereas $\max(acc_{1D})$ is the corresponding to the one-dimensional response.

Fig. 5.21 shows the comparison between the computed amplification factors for Ricker wavelets and cyclic motions for the prescribed values of frequency utilized throughout this study. In case of the lowest frequency considered, 1Hz, there is no significant variation of the comparative response for the two types of analysis except for the reduction in the horizontal motion of about 60% at a distance of 80m from the foot of the slope and the generation of a maximum vertical motion of one-fourth of the horizontal response close to the foot.

It has to be noted that the fluctuation of the amplification factors in both directions become larger while increasing the reference frequency. For instance, in regard to motions with an energetic frequency of about 2Hz, the incorporation of more cycles results in horizontal and vertical components of slightly more than two and one times the corresponding one-dimensional response, respectively. On the other hand, a common through close to the foothill is observed where the amplification factor drops to a value of about 0.15 for both directions.

Finally, for the highest frequencies analyzed, 4 and 10Hz, the overall trend of amplification distribution displays substantial values for the vertical motion which surpass those in the horizontal direction for the region close to the foot of the slope. In addition, the areas of influence of effective amplification reduce as well as the distance between peaks as a consequence of the shorter wavelengths involved. It is important to underline that the sequence of peaks and troughs along the basin-shaped part derives from the interference of the multiple Rayleigh-wave trains generated in a manner described in the previous section. The duration of the excitation for cycle motions is sufficiently long that it makes evident the constructive and destructive interference path which is a typical characteristic for complex motions.

5.5 Dynamic Response of Lomo de Corvina

Gonzales et al. (2017) examined the dynamic response of the layered sandy populated slope in Lomo de Corvina under the effect of the matched synthetic accelerogram discussed in Section 5.2.1. Additional evaluated cases correspond to the study of the influence of motions of various prescribed frequencies and the assumption of homogeneous dynamic properties throughout the slope model.

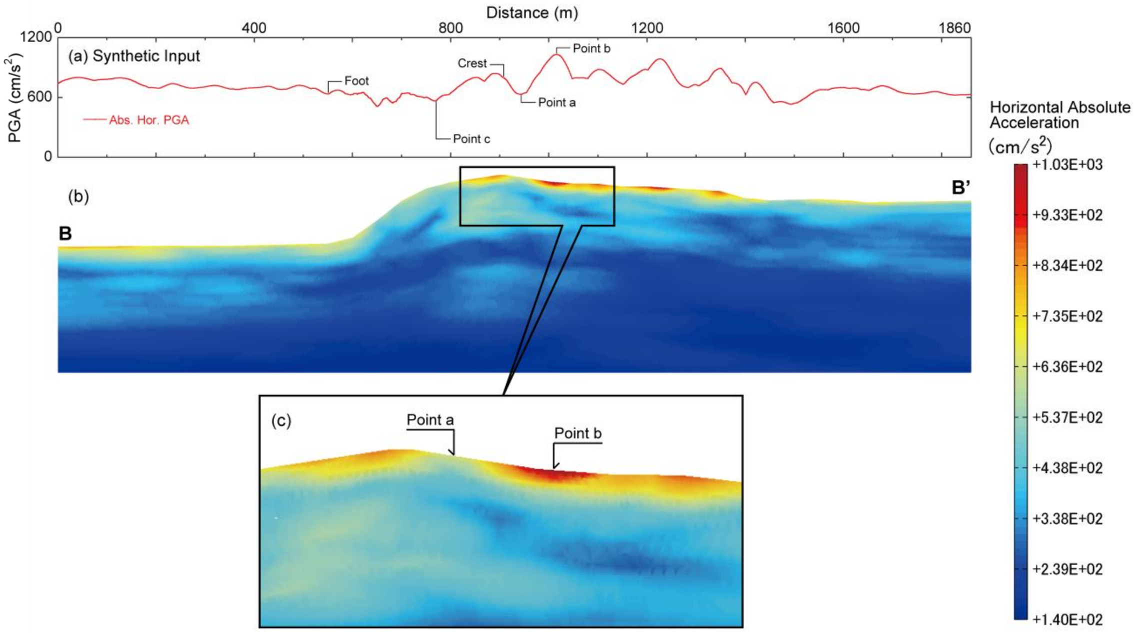

Fig. 5.22 (a) Absolute horizontal PGA, (b) distribution of the horizontal absolute acceleration and (c) zoom view of the areas opposite to the seashore of the slope in Lomo de Corvina

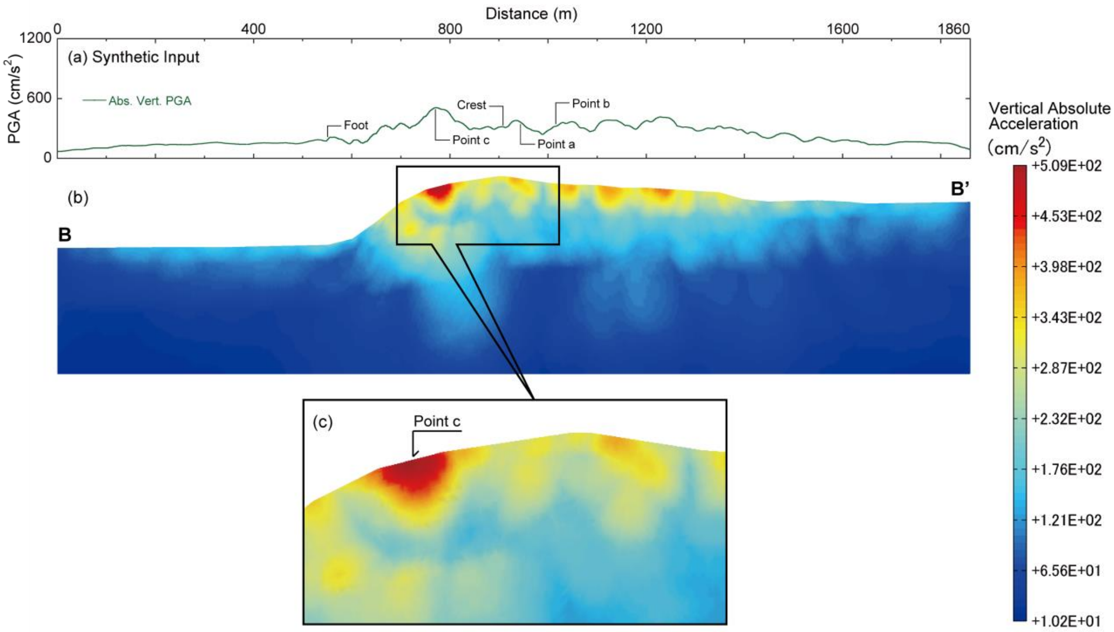

Fig. 5.23 (a) Absolute vertical PGA, (b) distribution of the vertical absolute acceleration and (c) zoom view of the areas of maximum vertical values in the slope in Lomo de Corvina

5.5.1 Synthetic Response

The application of the deconvoluted accelerogram presented in Fig. 5.2 for Lomo de Corvina as the horizontal input motion (SV-wave) at the bottom of the finite element model adopted for line B-B' resulted in the distributions of absolute horizontal and vertical acceleration shown in Fig. 5.22 and Fig.5.23, respectively.

Variation of the absolute horizontal PGA (Fig. 5.22a) shows that, for areas close to both left and right boundaries, acceleration reach a fairly constant value of about 700cm/s^2. In contrast, an irregular pattern of peaks and troughs appears along the face opposite to the seashore (Fig. 5.22b). To analyze this difference in the response, waveforms were extracted at two locations with apparent opposite behavior, Points a and b, and compared with their correspondent one-dimensional finite element analyses of soil columns with the same mechanical and dynamic properties.

When considering one-dimensional propagation only, absolute values of PGA for both points (Fig. 5.24c, Fig. 5.25c) showed an average increment of 40% when compared to the surface motion at VSV* (500 cm/s^2). This is associated with the variation of the soil substructure, since a marked increase in the thickness of strata 2 (V_S = 341m/s) and 3 (V_S = 527m/s) can be found from the center part of the district of Villa El Salvador in the direction of the top of the slope.

Opposite behavior can be observed for both points when the effect of the topographic irregularity is included. Whereas Point a (Fig. 5.24d) shows a decrease of about 10% of the absolute PGA, as well as the shape of the Fourier and response acceleration spectra for some periods, Point b (Fig. 5.25d) reveals amplification of the response of more than 40%. It is important to highlight that the distance between these two points is merely 75m.

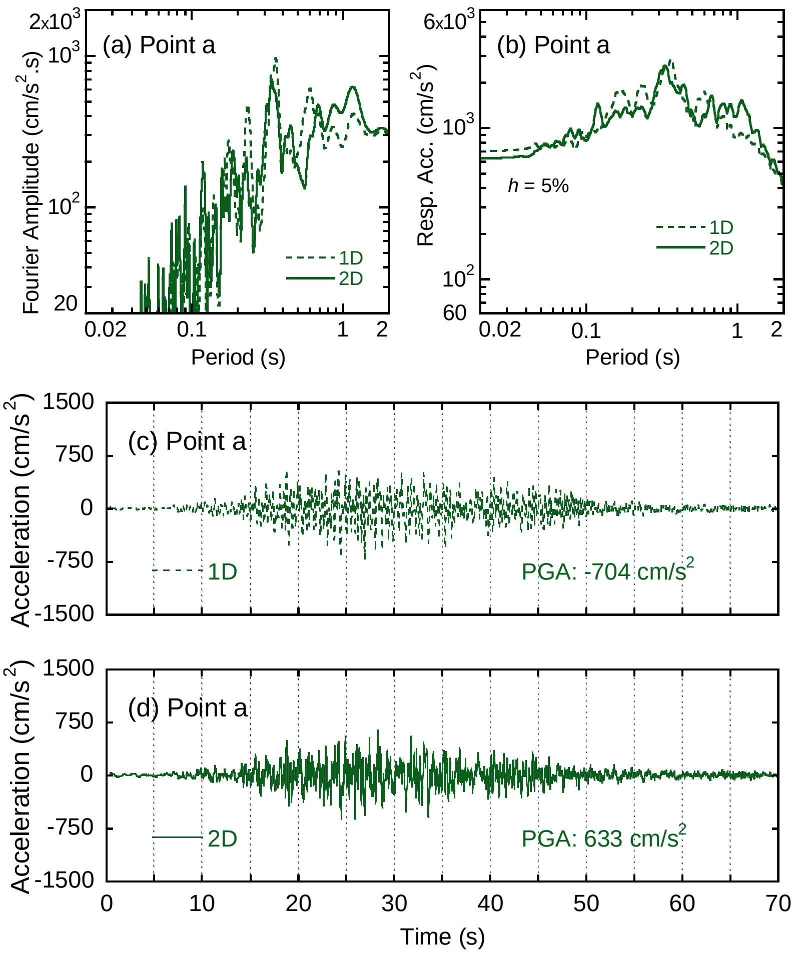

Fig. 5.24 (a) Fourier spectrum, (b) acceleration response spectrum and (c), (d) waveforms of the horizontal acceleration at Point a obtained by one and two-dimensional analyses in Lomo de Corvina, respectively

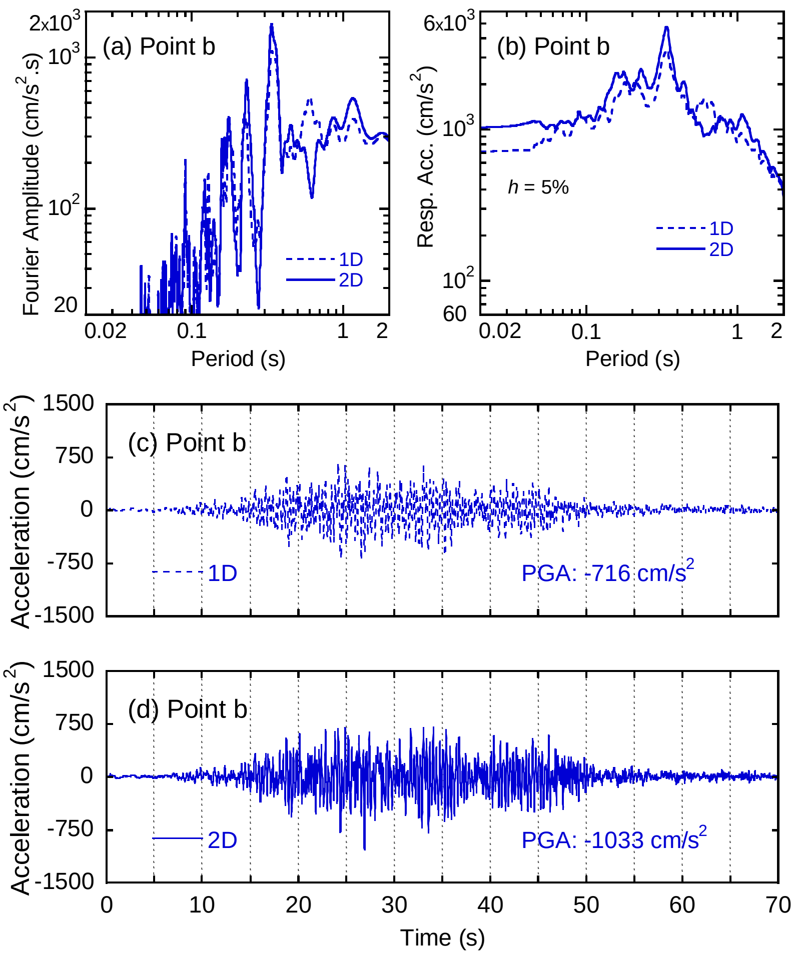

Fig. 5.25 (a) Fourier spectrum, (b) acceleration response spectrum and (c), (d) waveforms of the maximum horizontal acceleration (Point b) obtained by one and two-dimensional analyses in Lomo de Corvina, respectively

With respect to the distribution of absolute acceleration in the vertical direction (Fig. 5.23), high values are concentrated in the areas strictly belonging to the sloping parts which decrease towards both sides of the model. In addition, amplification of almost two times of the absolute PGA can be identified at some points on the side opposite to the slope, when compared to the results at their surroundings. On the other hand, the maximum vertical PGA was found on the side facing the seashore (Point c, Fig. 5.23c) with a considerable value of around 500cm/s^2 and a peak in the Fourier and response acceleration spectra in the vicinity of 0.35s (Fig. 5.26), the same as for horizontal motion for Points a and b.

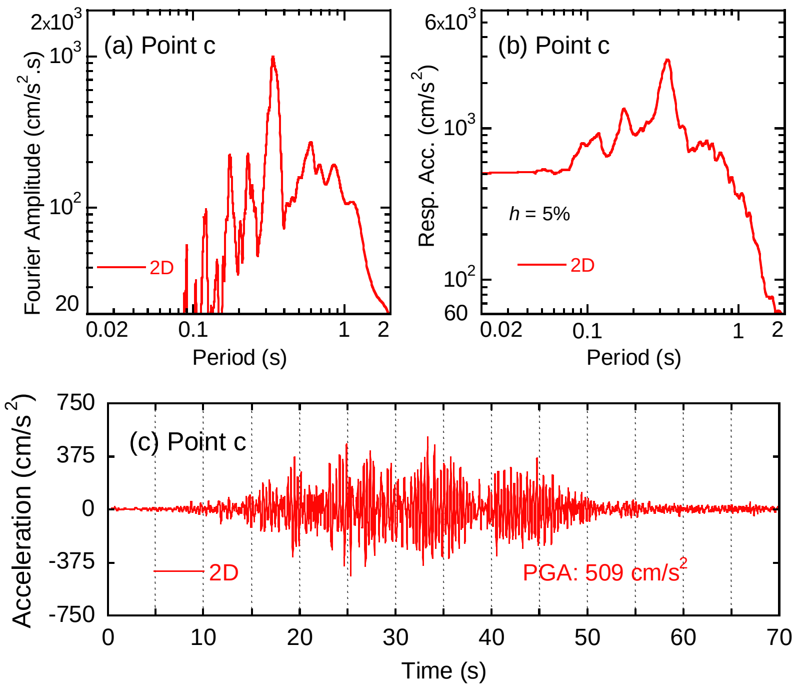

Fig. 5.26 (a) Fourier spectrum, (b) acceleration response spectrum and (c) waveform of the maximum surface vertical acceleration (Point c) obtained by two-dimensional analysis in Lomo de Corvina

It is important to mention that, unlike CSM*, results for two-dimensional analysis for the profile corresponding to VSV* were not able to be presented since its location is out of the scope of the generated finite element model for Lomo de Corvina.

Results that support the aforementioned are presented by means of complementary computations for prescribed-frequency motions in the subsequent sections.

5.5.2 Effect of Most Energetic Frequency

In order to separate the factors affecting the complex response of the slope in Lomo de Corvina, a set of parametric analyses was conducted.

The first variable taken into consideration was the impact of the frequency of the input motion in the slope behavior. Hence, the adopted stratigraphic finite element model was subjected to horizontal acceleration Ricker wavelets of unit amplitude as specified in Section 5.2.2.

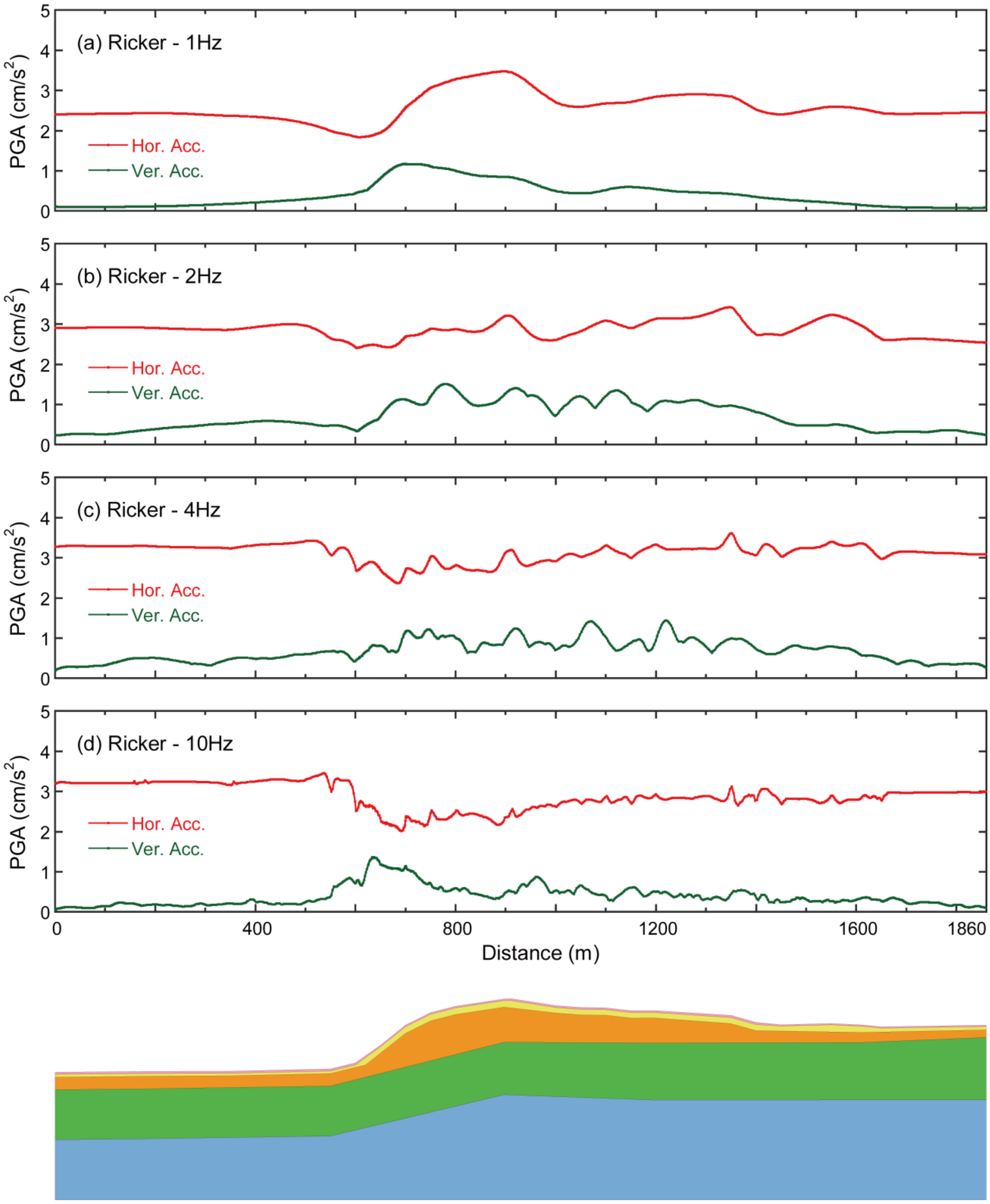

Fig. 5.27 Variation of the peak ground acceleration for different input motions (Ricker wavelets) in Lomo de Corvina

Fig. 5.27 shows the variation of the absolute values of horizontal and vertical PGA along the model for the most energetic frequencies considered. At first inspection, values of horizontal acceleration tend to stabilize towards the regions close the model side boundaries with a gradual reduction of those in the vertical direction, in all cases. This might be related to the basis of the substructure method in which the behavior of the side boundary columns is idealized as that for one-dimensional response, in addition to the negligible effect of surface waves reaching those areas, as explained in the subsequent cases.

Changes in the location of the punctual high acceleration areas along the surface were also encountered. Moreover, the distance between two consecutive local maximum values reduces, as well as the peaks become sharper, when considering high frequencies. Therefore, the influence of the predominant frequency of the input waveform in the propagation path is confirmed as suggested in Nakai et al. (2008).

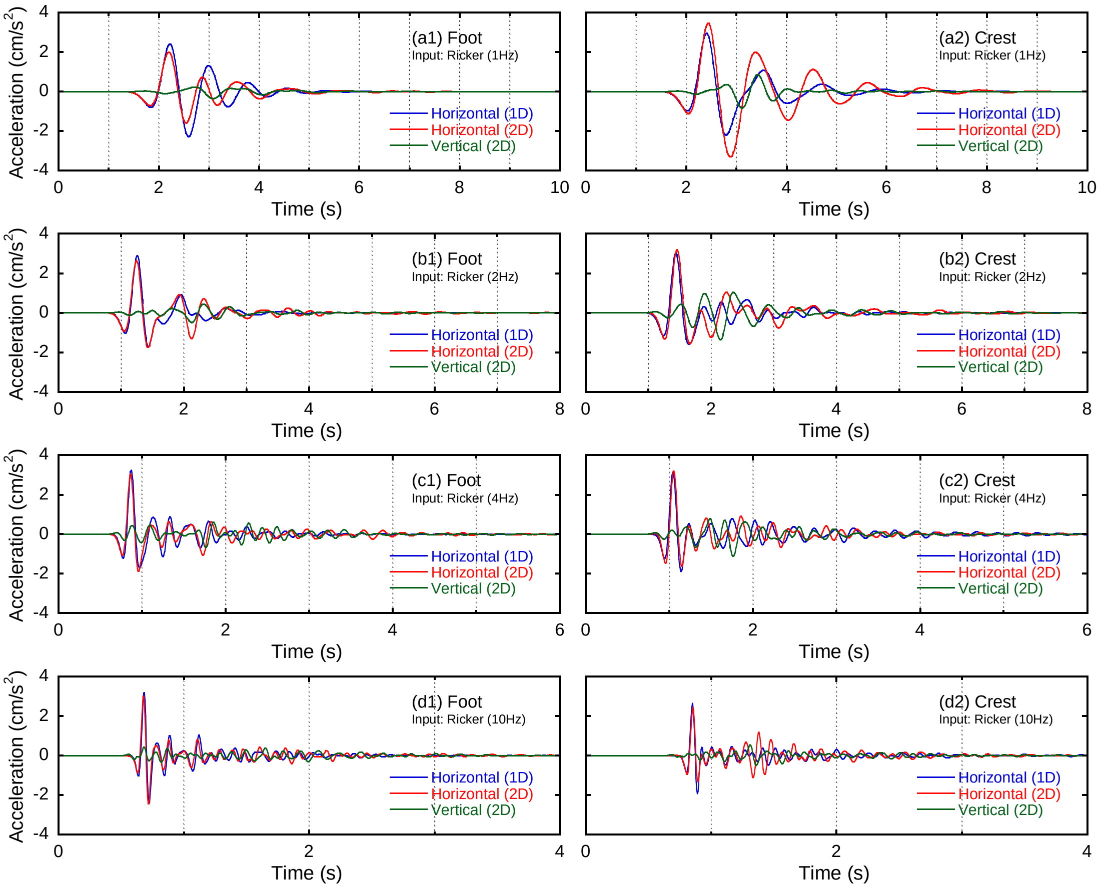

Fig. 5.28 Waveforms at the foot and crest of the slope in Lomo de Corvina for different Ricker wavelet inputs

Acceleration waveforms were extracted at points corresponding to the foot and crest of the slope (Fig. 5.28). A reduction of the response was observed at the foot whereas an increment was found in the crest, when including the geometric irregularity and variation in the soil substructure. This effect tends to be reduced while increasing the frequency. In addition, the presence of vertical components is more evident at the crest of the slope which might be an indicator of the stronger influence of surface waves along the face opposite to the seashore.

5.5.3 Simplified Homogeneous Slope

In order to examine the effect of the geometric irregularity only, simplified analyses of the slope with homogeneous properties throughout the entire model were performed. Two study cases were considered: the first one, a slope consisting of soft materials with a shear-wave velocity, V_S, of 250m/s and the second one, of an intermediate soil with V_S = 750m/s. In both cases, the density, ρ, was equal to 1800kg/m^3, the Poisson's ratio, υ, adopted a value of 0.35, whereas a damping ratio, ξ, of 2.5% was assumed.

The dispersive nature of surface waves is well-studied. In case of Love waves, it is known that the simplest layered condition in which this type of waves is developed is when considering a half-space overlaid by a material with lower body wave velocity. On the other hand, Rayleigh waves can coexist with body waves in a homogeneous elastic half-space, being its respective non dispersive phase velocity, V_R, obtained as a function of the Poisson's ratio and body waves, but generally simplified as $V_R = 0.919V_S$. Therefore, for the soil conditions idealized in this section, it is possible to evaluate the impact of surface waves, in the form of Rayleigh waves, by identifying the phase velocity of this type of waves from the wave propagation path along the slope.

Another aspect to take into consideration is the effect of the sloping areas in varying the direction of upcoming ray paths. It is known that SV-waves vertically propagating are reflected into P- and SV-waves when reaching an inclined free surface. Moreover, the values of their respective reflection angles are governed by the Snell's rule given in Eq. (5.13).

From the stated above, each of the homogeneous slopes considered uniquely affect the propagation path depending only on the particular ratio between its shear- and compressional-wave velocities, as it is seen in Fig. 5.29.

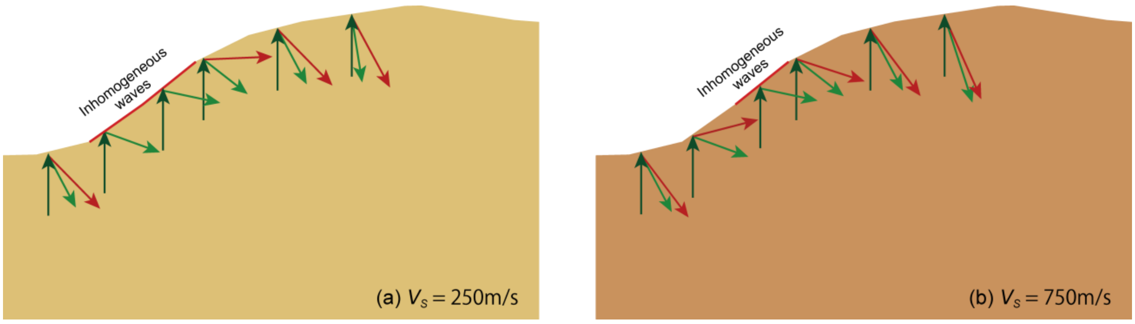

Fig. 5.29 Variation in the direction of the ray paths due to the slope for the two homogeneous models considered: (a) V_S = 250m/s and (b) V_S = 750m/s

It has to be mentioned that Fig. 5.29 follows the color convention for upcoming the SV-wave and reflected P- and SV-waves declared in Fig. 5.18. In case of the model with V_S = 250m/s, it is found that the slope inclination at areas close to the foot exceed the calculated value of critical angle for P-wave reflection (28.7^o) and therefore post-critical P-waves are generated along its surface (denoted by a red line). In addition, it is observed that areas on the face opposite to the seashore might be affected by P-waves reflected close to the crest of the slope.

On the other hand, from the stiffer model with V_S = 750m/s, a value of 37.8^o is obtained for the critical angle for P-wave reflection, which is surpassed by the inclination angle in a more limited extension than in the previous model. Finally, the face opposite to the seashore is still affected by the impinging of the reflected P-waves generated, in this case, close to the foot of the slope.

Analogous to the study of the simplified basin-shaped slope in Villa El Carmen, both homogeneous models for Lomo de Corvina were subjected to single (Ricker wavelets) and cyclic (sinusoidal waves) motions with the objective of identifying the generation of surface waves and the interference pattern, respectively.

a. Single Motion

The main advantage of dealing with models with homogeneous properties lies in the ability of representing the propagation characteristic by a unique value of frequency. Thus, Fig. 5.30 and Fig. 5.31 show the horizontal and vertical acceleration wavefield obtained for 2Hz input motions for the two homogeneous slopes examined, respectively.

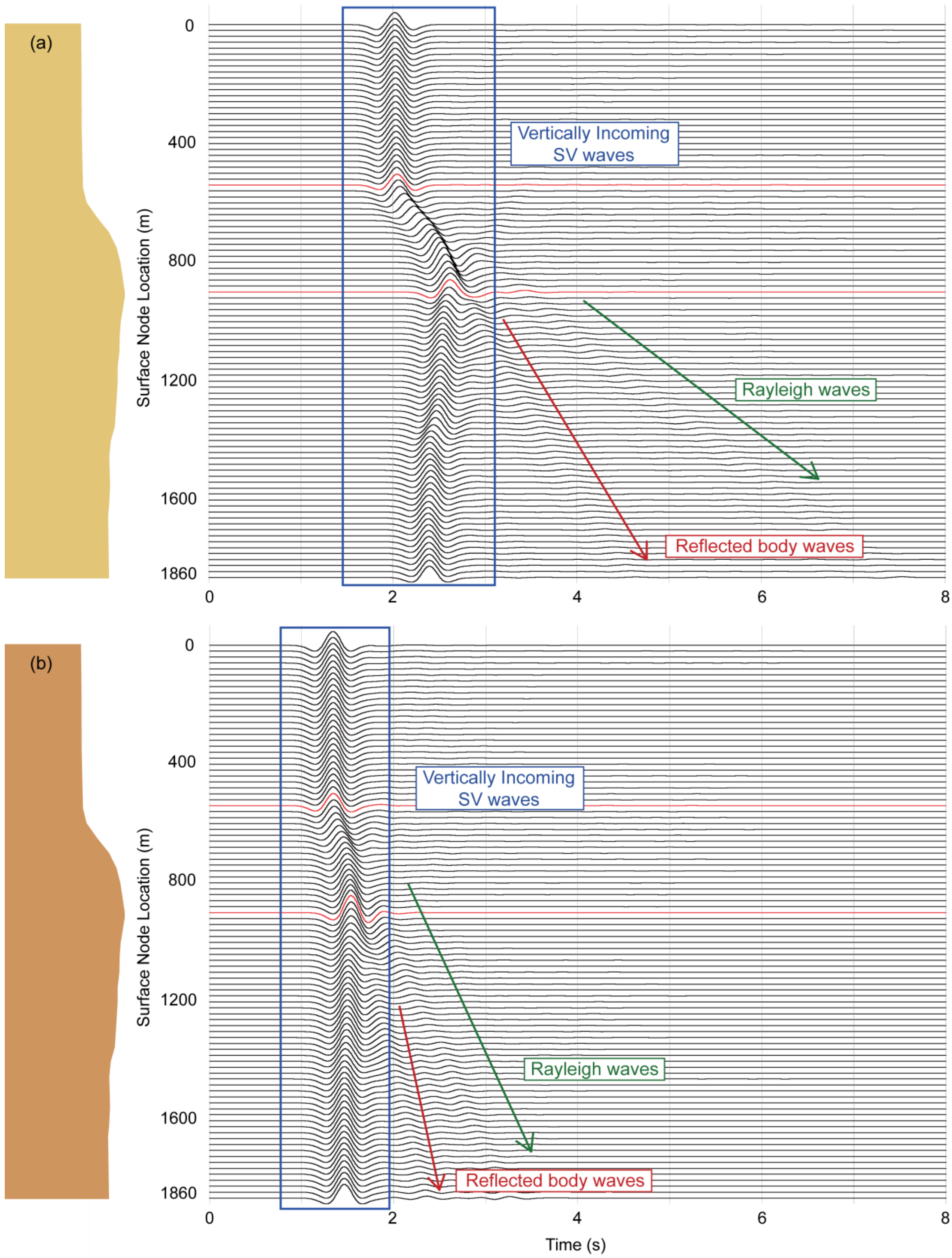

Fig. 5.30 Surface horizontal wavefield corresponding to a 2Hz Ricker wavelet horizontal input for a homogeneous model with V_S equal to (a) 250m/s and (b) 750m/s Lomo de Corvina

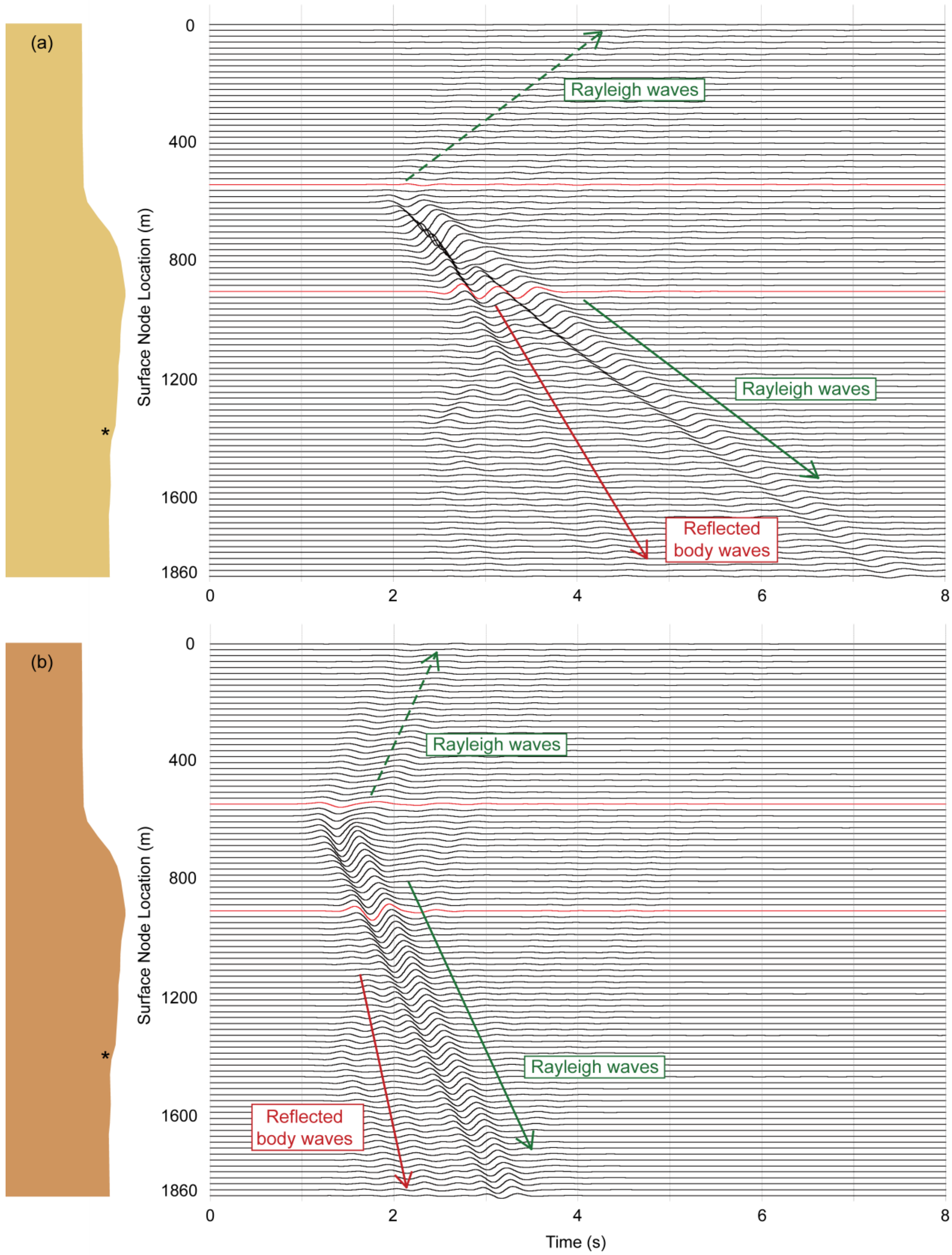

Fig. 5.31 Surface vertical wavefield corresponding to a 2Hz Ricker wavelet horizontal input for a homogeneous model with V_S equal to (a) 250m/s and (b) 750m/s Lomo de Corvina

In case of the horizontal motion, vertically incoming SV-waves are clearly first observed, in which the difference in the arrival time is obviously attributed to the changes in height along the evaluated slope. In addition, reflected body waves, travelling with a velocity within the range for P and S waves, and Rayleigh waves, propagating with a phase velocity of about 0.9 times that for the S-wave velocity, appear in the high areas of the model with an appreciable decrease in amplitude.

The existence of the above types of waves is assured when examining the vertical components of the wavefield. Reflection of body waves is apparent to occur along the inclined face whereas the generation of Rayleigh waves starts at a location close to the foot of the slope. It is important to mention that Rayleigh waves propagate in both directions of the model, being of much lower energy towards the flat low lands (dashed lines in Fig. 5.31).

Additional reflected waves can be observed since the geometry adopted for the corresponding model differs from the idealized case of a step-like slope. The nature of these waves is strictly linked to the minor geometric irregularities found along the slope, such as those appearing from the point characterized by an asterisk in Fig. 5.31.

The aforementioned behavior corroborates the hypothesis related to the impact of surface waves in the areas opposite to the seashore in Lomo de Corvina. This fact, added to the inclusion of a larger number of cycles in the input motion, alters the response in the form of possitive or destructive interference, such in the case of the synthetic motion analyzed in Section 5.5.1.

b. Cyclic Motion

As mentioned before, with the objective of quantifying the effect of the interference of Rayleigh waves in the surface response, cyclic motions consisting on eight cycles of sinusoidal waves were applied as vertically propagating SV-waves to both homogeneous models considered.

Analyses were performed at suitable values of frequency in each case that could assure reliable results by fulfilling the following requirements: first, the maximum propagation frequency applied had to be compatible with the generated mesh size and, second, the minimum frequency analyzed was chosen to be congruent with one wavelength of the applied excitation, which is the common limit when considering the influence of Rayleigh waves in depth. Thus, results are presented for 1, 2 and 4Hz for the homogeneous slope with V_S = 250m/s, whereas values of 2, 4 and 10Hz were preferred for that with V_S = 750m/s.

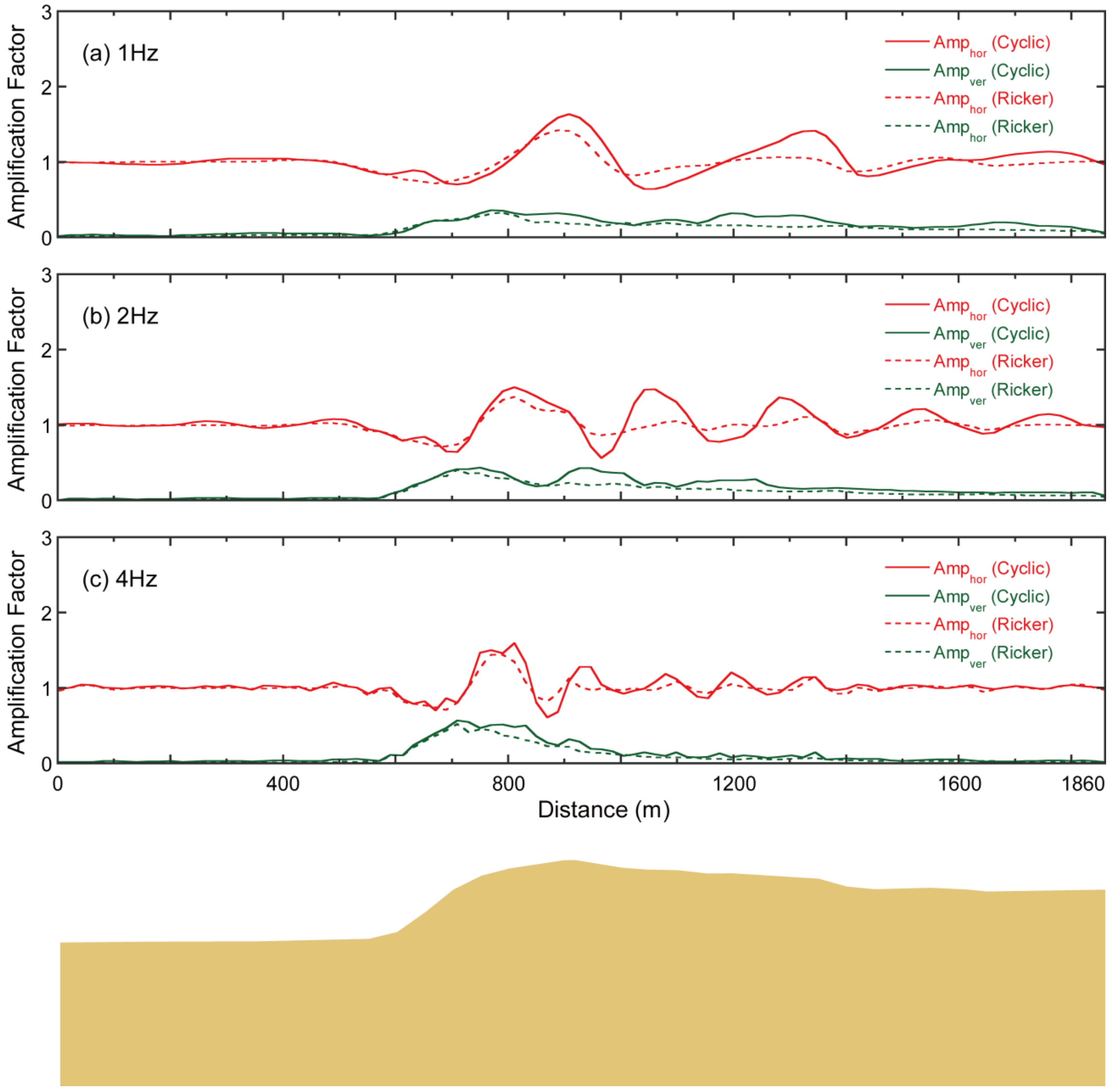

Fig. 5.32 Comparison between the horizontal and vertical amplification factors for Ricker wavelets and cyclic motions for the homogeneous model with V_S = 250m/s

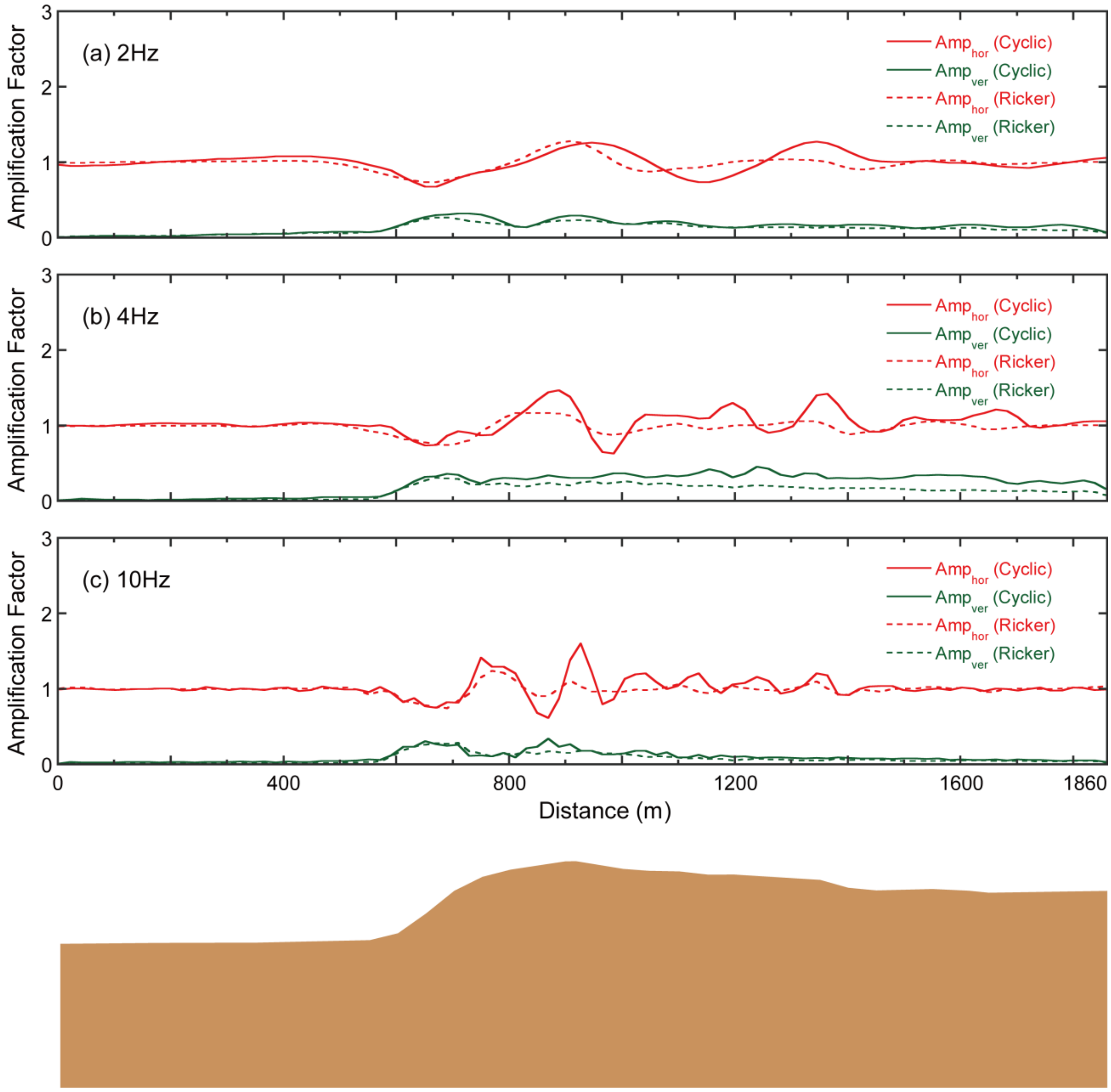

Fig. 5.33 Comparison between the horizontal and vertical amplification factors for Ricker wavelets and cyclic motions for the homogeneous model with V_S = 750m/s

In addition, one-dimensional response analyses were conducted for soil columns every 20m and the comparison of their maximum absolute results at the surface with those for the slope model was computed by means of the $\mathrm{Amp_{hor}}$ and $\mathrm{Amp_{ver}}$ factors defined in Eq. (5.14) and Eq. (5.15), respectively, for Ricker and cyclic motions.

As a general trend, the amplification factors obtained for the soft and stiff models (Fig. 5.32 and Fig. 5.33, respectively) confirm the negligible effect of Rayleigh waves along the lowlands on the left side of the models for both types of excitation. On the other hand, the minor fluctuations in these amplification factors encountered on the face opposite to the seashore for the case of Ricker wavelets can be attributed to the small topographic variations. Finally, when including more cycles in the waveform, as expected, constructive and destructive interference of Rayleigh waves is evident as well as location shift, in some cases, of the maximum amplification value.

Particularly, with respect to the model with 250m/s (Fig. 5.32), the minimum horizontal amplification factor encountered was about 0.70, evidencing deamplification, located in the lower third of the sloping part for all values of frequency and both types of excitation. On the other side of the slope, horizontal amplification factors for cyclic motion fluctuate within the range of 1.60 and 0.60, in average, aggravating the values computed for the case of Ricker wavelets. It has to be mentioned that values of vertical motion vary from 0.35 to 0.60 times those for the horizontal motion and its location coincides with that for the minimum horizontal amplification factor calculated.

With regard to the stiffer model (Fig. 5.33), similar values for the minimum amplification factor (0.70) were measured, whereas slightly lower maximum factors, both in the horizontal direction and cyclic motions, were found. Furthermore, maximum values of vertical motion are only of about 0.30 times those for the horizontal motion with the same characteristic location as in the soft model.

Finally, it should be pointed out that, for the same analyzed model, the distance between two consecutive peaks, or troughs, of the distribution of amplification factors decrease while increasing the frequency of analysis. This is related to the wavelength of the excitation involved in the analysis.

5.6 Sensitivity of Model’s Size

Models adopted for computations throughout this study are those listed in Section 4.4.1 (Fig. 4.4) and Section 4.4.2 (Fig. 4.5) for Villa El Carmen and Lomo de Corvina, respectively.

It is known that when defining the maximum transmitting frequency for certain type of problem, size of elements constituting the finite element mesh is crucial, in order to be able to capture information from high-frequency wavelengths. In the aforementioned sections, it was shown that the considered meshes were fine enough to represent the high-frequency characteristics of the applied motions investigated.

On the other hand, in case of low-frequency behavior, as well as in the study of surface waves, global size of the analyzed model in the vertical and horizontal directions might be of significant importance. Nevertheless, the consideration of larger models may have an undesirable impact on the computation time and, therefore, equilibrium between these two aspects must be reached.

It can be observed that both adopted finite element models possess a considerable length in the horizontal direction and, in consequence, the assessment of their respective sensitivity to changes in global size was decided to be conducted by increasing the thickness of the bedrock layer by 2000m for both cases.

Analyses for deep models were performed for Ricker wavelets of the lowest frequency adopted, 1Hz and 2Hz, and for a motion with complex frequency content, such as the synthetic accelerograms deconvoluted for each site.

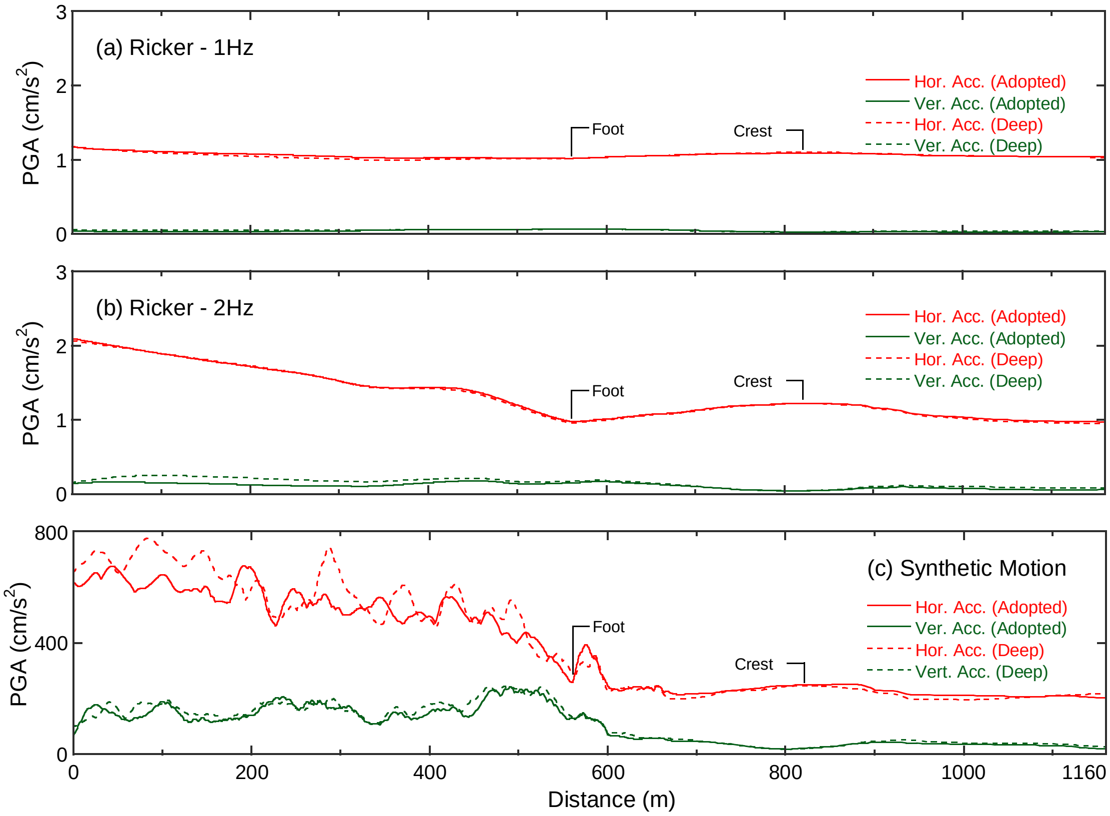

Fig. 5.34 Comparison of absolute values of horizontal and vertical PGA for the originally adopted and the 2000m-deeper model in Villa El Carmen

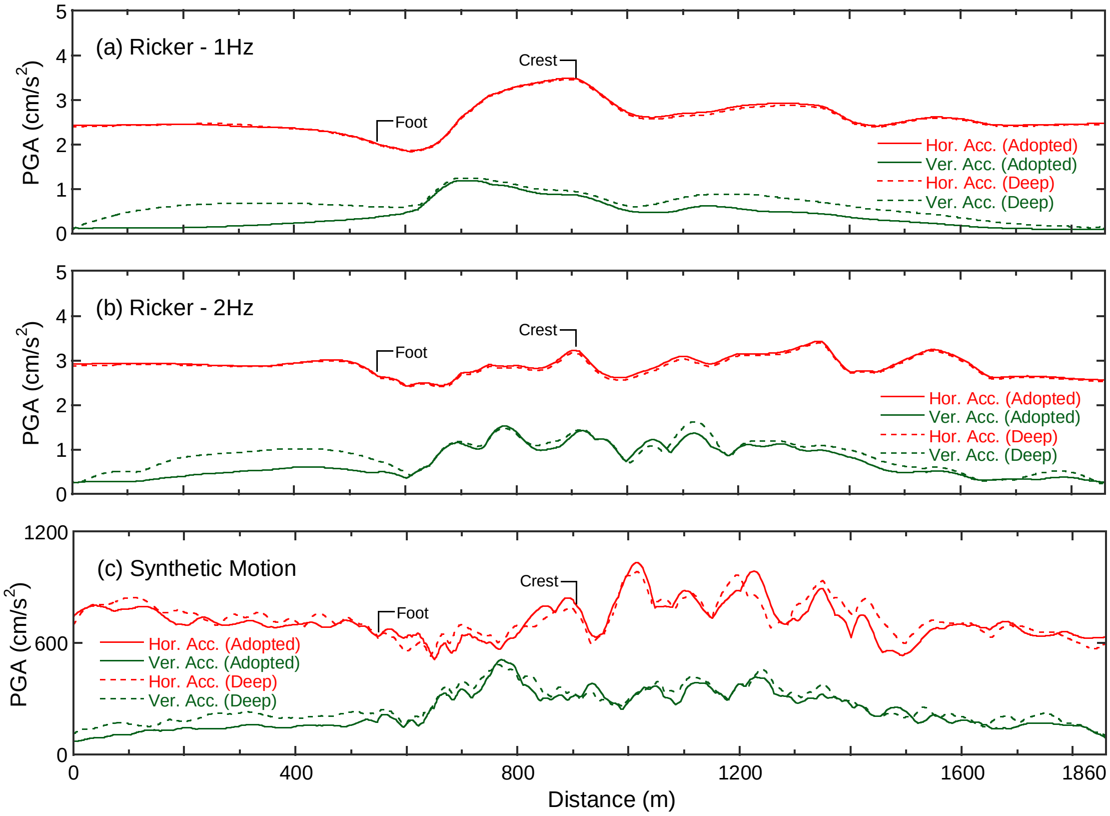

Fig. 5.35 Comparison of absolute values of horizontal and vertical PGA for the originally adopted and the 2000m-deeper model in Lomo de Corvina

In case of Villa El Carmen, comparison of the distribution of the absolute values of horizontal and vertical PGA for the adopted and the deep models (Fig. 5.34) shows that, for motions with prescribed low frequency, the effect of considering a deeper model does not affect considerably the response at the surface. Distinct behavior is found when analyzing the synthetic motion. With regard to the horizontal components, drastic changes in the location of peaks and amplitudes are detected in the flat areas which might suggest a stronger interaction between surface waves travelling from the foot of the slope and the vertically incoming and refracted body waves.

The above fact indicates the relatively high sensitivity of the horizontal response of model to depth and complex frequency of the input motion. Therefore, quantitative analyses of the flat areas in Villa El Carmen should be conducted for each specific case and the remarks given in the previous sections must be taken as indicators of the overall behavior exclusively. In addition, populated areas strictly located in the sloping part within the foot and crest of the model do no present considerable variations for both models, hence results are still applicable to that scope. Finally, only minor fluctuations in the values of acceleration for the vertical direction were encountered.

Analogous analyses were performed for Lomo de Corvina and presented in Fig. 5.35. In relation to low-frequency Ricker input motions, appreciable variations are observed for accelerations in the vertical direction towards the side boundaries of the model. This might suggest a stronger influence of the surface waves in the flat low areas than the expected in previous sections. Moreover, deviations in the surface response were encountered to some extent in both directions when considering a synthetic input motion. Thus, the originally adopted model can still be considered to predict the global dynamic behavior in Lomo de Corvina.

Chapter 6: Conclusions

6. Conclusions

The present study aimed to comprehend the determining factors in the seismic response of slopes with contrasting characteristics in the city of Lima, in Peru, which started to be populated as a result of the massive migration from the provinces about sixty years ago. To accomplish this goal, a systematic series of procedures involving the reliable determination of the soil substructure, the accurate numerical modeling and solution of the considered dynamic problem was established and applied to two target slopes: one characterized as a basin-shaped slope adjacent to a rocky mountain (Villa El Carmen) and the other located in a sandy dune (Lomo de Corvina). The aforementioned was carefully listed in the chapters comprising this thesis and the major findings are described as follows:

- **Estimation of Shear-wave Velocity Profiles along the Populated Slopes**

Surface wave methods have been tested in order to be considered, to some extent, as reliable tools in the extraction of dispersion curves for the further estimation of shear-wave velocity profiles along a ground with irregularities.

In case of the field survey in Villa El Carmen, circular microtremor arrays were mainly performed, with their size being limited by the availability of areas large enough to deploy the sensors in a polygonal arrangement. This was a crucial factor in the overcrowded areas strictly located in the sloping parts and, therefore, only miniature circular and linear arrays were carried out on roads or limited free spaces.

Much restricted conditions were found in Lomo de Corvina due to its chaotic urbanization process. To overcome this difficulty, MASW tests were selected in this case with the receiver line placed perpendicular to the plane of the slope in order to avoid the effects of height variation. This allowed a maximum penetration depth of about 30m for each of the conducted tests.

The combination of the shear-wave velocity profiles obtained by the above methods with the deep information available in the flat areas permit a reliable representation of the vibration characteristics of the underlying ground column represented by the fundamental period of the soil calculated from single point microtremor measurements.

- **Dynamic and Finite Element Modeling**

The soil substructure profile for certain slope model was obtained by the interpolation of the results at the selected locations along the surface. This procedure took under consideration the variations of altitude between points and was carefully performed in order to avoid large discrepancies with the vibration properties originally estimated.

Two meshing techniques were adopted within the framework of this work and applied to each of the target areas, separately. The advancing front technique employed for Villa El Carmen resulted in a mesh adaptable to the change in stiffness of the corresponding layers, which is the common practice in finite element modeling. On the other hand, even though the convex polygon approach generated a relatively uniform mesh within each of the subdomains defined for Lomo de Corvina, the size of elements was still satisfactory due to the adoption of the quadratic isoparametric formulation which, for the same wavelength considered, allows elements of larger size when compared with their linear counterpart.

The substructure method was utilized for the finite element modeling of a soil system with irregularities. Numerical applications in horizontal layered media have shown that, even though the input motion is of the form of vertically propagating shear waves, undesirable vertical acceleration components are produced on the side boundaries due to the use of dashpots as absorbing elements and frequency-dependent material damping. However, their amplitudes are in the order of less than 1% of the maximum expected horizontal acceleration and, therefore, the method is still applicable if the boundaries are placed far enough from the irregularity.

- **Seismic Response and Comprehension of Behavior Factors**

a. Villa El Carmen

The dynamic behavior of the multilayered basin-shaped populated slope contiguous to a rock body in Villa El Carmen is mainly determined by the influence of the very stiff materials comprising most parts of the model.

Analysis of a motion of complex-frequency content, such as the synthetic accelerogram considered, evidenced a reduction in the response for areas close to the foot when compared with the results from one-dimensional soil columns with the same dynamic properties. This effect tends to decrease towards the top.

With respect to the zones of maximum acceleration, these can be strictly found along the flat lowlands in a distribution of sharp peaks. This fact might imply the influence of basin effects in conjunction with the interference of surface waves.

Simpler input motions, such as unit Ricker wavelets within the range of 1Hz-10Hz were also contemplated. Distribution of the absolute PGA in both directions suggests a stronger influence of high-frequency components in the global response as well as in the generation of surface waves from the topographic irregularity. Thus, the overall seismic behavior of Villa El Carmen can be understood as the massive rock body being almost unaltered and the basin in the low part affected by the joint interference of vertically propagating and refracted body waves and surface waves travelling from the foot provoking zones of particular amplification.

Variations in the direction of the propagation paths of vertically incoming SV-waves were also considered through the analysis of a simplified model in which, for the sake of simplicity, the basin-shaped part was assumed to be comprised of materials with the same dynamic properties and a thin layer representing the shallow borrowed soil. The calculation of amplification factors with respect to the maximum response of equivalent soil columns evidenced the generation of considerable amplitudes of vertical motion for high frequencies and amplification values as larger as two in both directions along the surface of the basin when cyclic motions are considered.

b. Lomo de Corvina

In case of the layered sandy populated slope in Lomo de Corvina, when considering a complex synthetic waveform, selected areas of local amplification and deamplification of the horizontal component are encountered along the face opposite to the seashore with respect to their respective results from one-dimensional response. Regarding the vertical motion, considerable values of acceleration of low-frequency content are found along the strictly sloping face.

The analysis of Ricker wavelets evidenced a stronger influence of motions within the range from low to medium frequency in the surface response and in the restricted and freed motions expected at the foot and crest of the slope, respectively.

Surface wave generation plays an important role in the seismic behavior of Lomo de Corvina as demonstrated by the study of slope cases with homogeneous properties. First, it was identified that each of the inclined surfaces that make up the main slope have a particular impact in the propagation path of vertically incoming

SV-waves leading to the generation of surface waves, some of them producing post-critical reflected P-waves and others generating reflected P-waves that eventually impinge on the face opposite to the seashore. Finally, constructive and destructive interference of surface (Rayleigh) waves was quantified by means of amplification factors as well. Minor variations were encountered along the areas corresponding to the seashore, whereas important fluctuations happen on the opposite face when considering cyclic waveforms. Amplification factors were as large as 1.60 for the horizontal motion close to the crest and had a minimum value of 0.70, in average, whose location coincide with that for the maximum vertical amplification factor.

Further works would involve the estimation of more accurate soil layering structures of the slopes studied through the execution of a larger number of geophysical tests and topographic surveys. The inclusion of additional places in the surveys will allow their further analysis and widening the understanding of populated slopes in Lima. Finally, validation of the results by means of real seismic records is a pendent task of vital importance.

References

1. Aguilar Z. (2005): Seismic Microzonation of Lima. Japan-Peru *Workshop on Earthquake Disaster Mitigation*, Japan-Peru Center for Earthquake Engineering Research and Disaster Mitigation (CISMID), Faculty of Civil Engineering, National University of Engineering, Lima, Peru (in Spanish).

2. Aki K. (1957): Space Time Spectra of Stationary Stochastic Waves, with Special Reference to Microtremors. *Bulletin of Earthquake Research Institute*, Vol. 35, pp. 415-456.

3. Ashford S., Sitar N., Lysmer J. and Deng N. (1997): Topographic Effects on the Seismic Response of Steep Slopes. *Bulletin of the Seismological Society of America*, Vol. 87, No. 3, pp. 701-709.

4. Assimaki D., Kausel E. and Gazetas G. (2005): Soil-dependent Topographic Effects: A Case Study from the 1999 Athens Earthquake. *Earthquake Spectra*, Vol. 21, No. 4, pp. 929-966.

5. Athanasopoulos G.A., Pelekis P.C. and Leonidou E.A. (1999): Effects of Surface Topography on Seismic Ground Response in the Egion (Greece) 15 June 1995 Earthquake, *Soil Dynamics and Earthquake Engineering*, 18, pp. 135-149.

6. Bard P-Y. and SESAME participants (2004): The SESAME project and Main Results, *Proceedings of the 13th World Conference on Earthquake Engineering*, Paper No. 2207.

7. Bouckovalas G. D. and Papadimitriou A. G. (2005): Numerical Evaluation of Slope Topography Effects on Seismic Ground Motion, *Soil Dynamics and Earthquake Engineering*, 25, pp. 547-558.

8. Calderon D., Lazares F., Aguilar Z., Sekiguchi T. and Nakai S. (2011): Estimation of Deep Soil Profiles in Lima, Peru, *Journal of Civil Engineering and Architecture*, Vol. 5, No. 7, pp. 618-627.

9. Calderon D., Sekiguchi T., Nakai S., Aguilar Z. and Lazares F. (2012a): Study of Soil Amplification based on Microtremor and Seismic Records in Lima Peru, *Journal of Japan Association for Earthquake Engineering*, Vol. 12, No. 2, pp. 1-20.

10. Calderon D. (2012b): *Dynamic Characteristics of the Soils in Lima, Peru, by Estimating Shallow and Deep Shear-Wave Velocity Profiles*, Doctoral Thesis, Graduate School of Engineering, Chiba University, Japan.

11. Calderon D., Aguilar Z., Lazares F., Sekiguchi T. and Nakai S. (2013): Estimation of Deep-Shear Wave Velocity Profiles in Lima, Peru, Using Seismometers Arrays, *Journal of Disaster Research*, Vol. 8, No. 2, pp. 252-258.

12. Capon J. (1969): High-resolution Frequency-wavenumber Spectrum Analysis, *Proceedings of the IIEE*, Vol. 57, No. 8, pp. 1408-1418.

13. Celebi M. (1987): Topographical and Geological Amplifications Determined from Strong-Motion and Aftershock Records of the 3 March 1985 Chile Earthquake, *Bulletin of the Seismological Society of America*, Vol. 77, No. 4, pp. 1147-1167.

14. Chambi G. (2001): *Local Development with Participatory Management. Participatory Budget in Villa El Salvador*, Institute of Housing and Urban Development Studies (IHS) of the Netherlands, Support for Implementation of National Plans of Action (SINPA) Papers, Vol. 9 (in Spanish).

15. Chavez-Garcia F. J., Sanchez L. R. and Hatzfeld D. (1996): Topographic Site Effects and HVSR. A Comparison between Observations and Theory, *Bulletin of the Seismological Society of America*, Vol. 86, No. 5, pp. 1559-1573.

16. Chavez-Garcia F. J., Rodriguez M., Field E. H. and Hatzfeld D. (1997): Topographic Site Effects. A Comparison of Two Nonreference Methods, *Bulletin of the Seismological Society of America*, Vol. 87, No. 6, pp. 1667-1673.

17. Cho I., Tada T. and Shinozaki Y. (2004): A New Method to Determine Phase Velocities of Rayleigh Waves from Microseisms, *Geophysics*, 69, pp. 1535-1551.]

18. CISMID. Japan-Peru Center of Earthquake Engineering Research and Disaster Mitigation (2005): *Vulnerability and Seismic Risk in 42 Districts in Lima and Callao* (in Spanish).

19. CISMID. (2011): *Report: Seismic Microzonation of the District of Villa El Salvador, Lima, Peru*, Specific Interinstitutional Agreement between the Ministry of Housing, Construction

and Sanitation and the National University of Engineering (in Spanish).

20. CISMID. (2013a): *Report: Seismic Microzonation of the District of Independencia*, Activity 5.003430: Development of Seismic and Tsunami Microzonation, Product 3.000481: Local Governments with Evaluation of the Risk under Earthquakes and Tsunamis, Program 0068: Reduction of the Vulnerability and Emergency Response (in Spanish).

21. CISMID. (2013b): *Generation of Synthetic Accelerograms for the Coast of Peru. Product No. 2* (in Spanish).

22. CISMID. (2014): *MASW and Seismic Refraction Test in the Zone of Lomo de Corvina-Villa El Salvador, Lima, Peru* (in Spanish).

23. Clough R.W. and Penzien J. (2003): *Dynamic of Structures*, Third Edition. Computers & Structures Inc. Berkeley CA.

24. Dal Moro G., Pipan M and Gabrielly P. (2006): Rayleigh Wave Dispersion Curve via Genetic Algorithms and Marginal Posterior Probability Density Estimation, *Journal of Applied Geophysics*, Vol. 61, No. 1, pp. 39-55.

25. Ergatoudis I., Irons B. M. and Zienkiewicz O. C. (1968): Curved, Isoparametric, “Quadrilateral” Elements for Finite Element Analysis, *International Journal of Solids and Structures*, Vol. 4, No. 1, pp. 31-42. Pergamon Press.

26. Gabas A., Macau A., Benjumea B., Bellmut F., Figueras S. and Vila M. (2014): Combination of Geophysical Methods to Support Urban Geological Mapping, *Surveys in Geophysics,* Vol. 35, No. 4, pp. 983-1002.

27. Gelagoti F., Kourkoulis R., Anastasopoulos I., Tazoh T. and Gazetas G. (2010): Seismic Wave Propagation in a Very Soft Alluvial Valley: Sensitivity to Ground-Motion Details and Nonlinearity, and Generation of a Parasitic Vertical Component, *Bulletin of the Seismological Society of America*, Vol. 100, No. 6, pp. 3035-3054.

28. Goldberg D. E. (1989): *Genetic Algorithms in Search, Optimization, and Machine Learning*, Addison-Wesley Publishing Company Inc.

29. Gonzales C., Nakai S., Sekiguchi T., Calderon D., Aguilar D. and Nakai S. (2014a): Estimation of the Dynamic Properties and Seismic Response of a Populated Slope in Lima, Peru, *Journal of Disaster Research*, Vol. 9, No. 1, pp. 17-26.

30. Gonzales C., Nakai S., Sekiguchi T., Calderon D., Aguilar D. and Nakai S. (2014b): Analysis of Topographic Effects in Dynamic Response of a Typical Rocky Populated Slope in Lima, Peru, *Journal of Disaster Research*, Vol. 9, No. 6, pp. 946-953.

31. Gonzales C., Sekiguchi T. and Nakai S. (2017): Seismic Response of a Sandy Populated Slope in Lima, Peru, *Journal of Structural Engineering*, Vol. 63B, pp. 317-324.

32. Harmsen S. and Harding S. (1981): Surface Motion over a Sedimentary Valley for Incident Plane P and SV Waves, *Bulletin of the Seismological Society of America*, Vol. 71, No. 3, pp. 655-670.

33. Hashash Y. and Park D. (2002): Viscous Damping Formulation and High Frequency Motion Propagation in Non-linear Site Response Analysis, *Soil Dynamics and Earthquake Engineering*, 22, pp. 611-624.

34. Hinton E. and Owen D. (1977): *Finite Element Programming*, Academic Press Inc. (London) Ltd.

35. Horike M. (1985): Inversion of Phase Velocity of Long-Period Microtremors to the S-wave Velocity Structure Down to the Basement in Urbanized Areas, *Journal of Physics of the. Earth*, Vol. 33, No. 2, pp. 59-96.

36. INADUR. National Institute of Urban Development (1996): Municipality of the District of Villa El Salvador. *Urban Plan of Villa El Salvador. Project Narrative. Vol. 1* (in Spanish).

37. INDECI. National Institute of Civil Defense (2014): *Landslide Hazard in Lomo de Corvina. Villa El Salvador*, Risk Report No. 621-25/09/2014/COEN-INDECI/10:00, Report No. 3 (in Spanish).

38. INEI. National Institute of Statistics and Informatics (2012): *Peru: Estimations and Projections of the Total Population in the Main Cities by Gender, 2000-2015*, Special

Bulletin No. 23 (in Spanish).

39. Irons B. M. (1970): A Frontal Solution Program for Finite Element Analysis, *International Journal for Numerical Methods in Engineering*, Vol. 2, pp. 5-32.
40. Jafarzadeh F., Shahrabi M. and Jahromi H. (2015): On the Role of Topographic Amplification in Seismic Slope Instabilities, *Journal of Rock Mechanics and Geotechnical Engineering*, Vol. 7, pp. 163-170.

41. Joe B. (1991): GEOMPACK – A Software Package for the Generation of Meshes Using Geometric Algorithms, *Advances in Engineering Software and Workstations*, Vol. 13, No. 5/6 combined, pp. 325-331.

42. Joe B. (1995): Quadrilateral Mesh Generation in Polygonal Regions, *Computer-Aided Design*, Vol. 27, No. 3, pp. 209-222.

43. Kramer S.L. (1996): *Geotechnical Earthquake Engineering*, Prentice-Hall International Series in Civil Engineering and Engineering Mechanics, Upper Saddle River, NJ.

44. Ktenidou O. J., Raptakis D., Apostolidis P. and Pitilakis K. (2007): Aspects of Surface Topography and Site Effects – Experimental and Numerical Studies at Aegion, Greece, *Proceedings of the 4th International Conference on Earthquake Geotechnical Engineering*.

45. Kurita T., Annaka T., Takahashi S., Shimada M. and Suehiro T. (2003): Effect of Irregular Topography on Strong Ground Motion Amplification, *Transactions of the 17th International Conference on Structural Mechanics in Reactor Technology (SMiRT 17)*. Paper # K03-1.

46. Lanzo G. and Vucetic M. (1999): Effect of Soil Plasticity on Damping Ratio at Small Cyclic Strains, *Soil and Foundations*, Vol. 39, No. 4, pp. 131-141.

47. Lopez Soria J., Ueda A. and Quiñones L. (2012): *History of the National University of Engineering (UNI)*, Book IV, Institutionalization of the University to Meet Development Challenges (1955-1984), UNI History Center: Science, Technology and Innovation, General Research Institute, University Press. Second Edition (in Spanish).

48. Matos J. (1990): *Rural Migrations and the Urbanization Process in Peru*, UNESCO. (in

Spanish)

49. Matsushima T., Koyanago T., Miyakoshi K. and Okada H. (1992): Estimation of Deep Geological Structures in Urban Areas from Long-period Microtremor Data, *Proceedings of the International Symposium on Earthquake Disaster Prevention*, Mexico, pp. 178-186.

50. Matsuoka M., Miura H., Midorikawa S. and Estrada M. (2013): Extraction of Urban Information for Seismic Hazard and Risk Assessment in Lima, Peru Using Satellite Imagery, *Journal of Disaster Research*, Vol. 8, No. 2, pp. 328-345.

51. Mauricio M. (2007, November 9): Lights and Shadows in Villa El Salvador, *La República*, retrieved from: http://www.larepublica.pe (in Spanish).

52. Ministry of Economy, Trade and Industry (METI) of Japan and the United States National Aeronautics and Space Administration (NASA): ASTER Global Digital Elevation model (GDEM), http://www.jspacesystems.or/jp/GDEM/E/1.html (last version released in October, 2011).

53. Nakagawa H. and Nakai S. (2008): Analysis of Surface Wave Propagation Based on the Thin layered Element Method, *Proceedings of the 14th World Conference on Earthquake Engineering*, Beijing, China.

54. Nakai S. et. al. (1985): On an Interface Substructure Method for Soil-Structure Interaction-Part I. Classification of an Interface Substructure Method, *Summaries of Technical Papers of the Annual Meeting of the Architectural Institute of Japan*, pp. 349-350 (in Japanese).

55. Nakai S., Tosauchi Y., Sekiguchi T., and Nagata Y. (2008): A Study on the Wave Propagation in the Ground with a Slope: Effect on Topography of the Ground on the Vibration Characteristics, *Summaries of Technical Papers of the Annual Meeting of the Architectural Institute of Japan*, pp. 973-974.

56. Nakai S. and Nakagawa H. (2009): Propagation of Rayleigh Waves in an Irregular Ground, *Proceeding of the 6th International Conference on Urban Earthquake Engineering*, Tokyo Institute of Technology, Tokyo, Japan.

57. Nakai S. (2012): Urban Disaster Mitigation Engineering. Lecture Notes, Chiba University, Japan.

58. Newmark N. (1959): A Method of Computation for Structural Dynamics, *Journal of the Engineering Mechanics Division*, 85, pp. 611-624.

59. Nuñez S., Vasquez J. (2009): *Critical Zones due to Geological Hazards in Metropolitan Lima*, First Report, Technical Report, Bureau of Environmental Geology and Geological Risk, The Geological, Mining and Metallurgical Institute of Peru (in Spanish).

60. Ohtsuki A. and Harumi K. (1983): Effect of Topography and Subsurface Inhomogeneities on Seismic SV Waves, *Earthquake Engineering and Structural Dynamics*, Vol. 11, pp. 441-462.

61. OYO Corporation. (2012): *Implementation of PS logging in Peru*, Report (in Japanese).

62. Palacios O., Caldas J. and Vela Ch. (1992): *Geology of the Quadrangle of Lima, Lurin, Chancay and Chosica*, The Geological, Mining and Metallurgical Institute of Peru, pp. 25-29 (in Spanish).

63. Park C. B., Miller R. D. and Xia J. (1998): Imaging Dispersion Curves of Surface Waves on Multichannel Record, *SEG Technical Program Expanded Abstracts*, pp. 1377-1380.

64. Park C. B., Miller R. D. and Xia J. (1999): Multichannel Analysis of Surface Waves, *Geophysics*, Vol. 64, No. 3, pp. 800-808.

65. Park C. B., Miller R. D. and Miura H. (2002): Optimum Field Parameters of a MASW Survey, *Proceedings of the 6th International Symposium of the Society of Exploration Geophysicists of Japan*.

66. Park D. and Hashash Y. (2004): Soil Damping Formulation in Nonlinear Time Domain Site response Analysis, *Journal of Earthquake Engineering*, Vol. 8, No. 2, pp. 249-274.

67. Pitilakis K., Raptakis D., Makra K. Ktenidou E. J., Pandi K., Manakou M. Pitilakis D. and Diagourtas D. (2004): Effects of Surface and Subsurface Topography on Strong Ground Motion at the City of Aegion-Greece, *Proceedings of the 13th World Conference on*

Earthquake Engineering.

68. Proaño R. and Zavala C. (2003): Estimation of the Seismic Response of Structures based on SDOF Systems for Calculation of Seismic Vulnerability, *Proceedings of the XIV National Conference of Civil Engineering, Iquitos, Peru*, Paper No. EM-38, 12p, 2003 (in Spanish).

69. Pulido N., Aguilar Z., Tavera H., Chlieh M., Calderon D., Sekiguchi T., Nakai S. and Yamazaki F. (2015): Scenario Source Models and Strong Ground Motion for Future Mega-earthquakes. Application to Lima, Central Peru, *Bulletin of the Seismological Society of America*, 105(1), pp. 368-386.

70. Quiroz L. (2014): *Evaluation of Seismic Performance of Residential Buildings in Lima, Peru: A Case Study of Buildings Constructed with Thin RC Walls and Confined Masonry Walls*, Doctoral Thesis, Graduate School of Engineering, Chiba University, Japan.

71. Quispe S., Chimoto K., Yamanaka H., Tavera H., Lazares F. and Aguilar Z. (2014): Estimation of S-Wave Velocity Profiles at Lima City, Peru Using Microtremor Arrays, *Journal of Disaster Research*, Vol. 9, No. 6, pp. 931-938.

72. Rayleigh J. W. S. and Lindsay R. B. (1945): *The Theory of Sound*, 1st American Ed. New York, Dover Publications.

73. Ricker N. (1952): The Form and Laws of Propagation of Seismic Wavelets, *Third World Petroleum Congress*.

74. Riofrio G. (2003): *Understanding Slums: Case Studies for the Global Report on Human Settlements. The case of Lima, Peru*, The United Nations Human Settlements Programme (UN-Habitat) and the Development Planning (DPU), University College London, available at: http://www.ucl.ac.uk/dpu-projects/Global_Report/home.htm

75. Saez E., Garcia J. and Roch F. (2010): Growing Cities from Houses: Spontaneous cities in Lima, *Invi Magazine*, Vol. 25, No. 70, pp. 77-116 (in Spanish).

76. Sekiguchi T., Calderon D., Nakai S., Aguilar Z. and Lazares F. (2013): Evaluation of Surface Soil Amplification for Wide Areas in Lima, Peru, *Journal of Disaster Research*,

Vol. 8, No. 2, pp. 259-265.

77. Stokes S. (1989): *Politics and Popular Awareness in Lima. The Case of the District of Independencia*, Working Document No. 31, Sociological/Political Series No. 5, IEP Press (in Spanish).

78. Tachikawa T., Hato M., Kaku M. and Iwasaki A. (2011): The Characteristics of ASTER GDEM version 2, *Proceedings of the 2011 IEEE International Geoscience and Remote Sensing Symposium*.

79. Tada T., Cho I. and Shinozaki Y. (2007): Beyond the SPAC Method: Exploiting the Wealth of Circular-array Methods for Microtremor Exploration, *Bulletin of the Seismological Society of America*, Vol. 97, pp. 2080-2095.

80. Wada K., Nakai S. and Sekiguchi T. (2014): Time-history Elastoplastic Analysis of Irregular Ground by Two-dimensional Finite Element Method, *Summaries of Technical Papers of the Annual Meeting of the Architectural Institute of Japan*, pp. 415-416 (in Japanese).

81. Wang Y. (2015): Frequencies of the Ricker Wavelet, *Geophysics*, Vol. 80, No. 2, pp. A31-A37.

82. Xia J., Miller R. and Park C. (1999): Estimation of Near-surface Shear-wave Velocity by Inversion of Rayleigh Waves, *Geophysics*, Vol. 64, No. 3, pp. 691-700.

83. Yamanaka H. and Ishida H. (1996): Application of Genetic Algorithms to an Inversion of Surface-Wave Dispersion Data, *Bulletin of the Seismological Society of America*, Vol. 86, No. 2, pp. 436-444.

84. Yamanaka H., Quispe M., Chimoto K., Saguchi K., Calderon D., Lazares F. and Aguilar Z. (2016): Exploration of Deep Sedimentary Layers in Tacna City, southern Peru, using Microtremors and Earthquake Data for Estimation of Local Amplification, *Journal of Seismology*, Vol. 20. No. 1, pp. 107-116.

85. Yamazaki F. and Zavala C. (2013): SATREPS Project on Enhancement of Earthquake and Tsunami Disaster Mitigation Technology in Peru, *Journal of Disaster Research*, Vol. 8, No.

2, pp. 224-234.

86. Zhao J. (2005): *Rock Mechanics for Civil Engineers*, Chapter 4, Lecture Notes, School of Architecture, Civil and Environmental Engineering, Swiss Federal Institute of Technology.

87. Zhu J. Z., Zienkiewicz O.C., Hinton E. and Wu J. (1991): A New Approach to the Development of Automatic Quadrilateral Mesh Generation, *International Journal for Numerical Methods in Engineering*, Vol. 32, pp. 849-866.

88. Zienkiewicz O. C., Taylor R. L. and Zhu J. Z. (2013): *The Finite Element Method: Its Basis and Fundamentals*, Seventh Edition, Elsevier Ltd.

Articles Submitted to Journals

1. Gonzales C., Sekiguchi T. and Nakai S. (2017). Seismic Response of a Sandy Populated Slope in Lima, Peru. *Journal of Structural Engineering*. Vol. 63B. pp. 317-324.

2. Gonzales C., Nakai S., Sekiguchi T., Calderon D., Aguilar D. and Lazares F. (2014). Analysis of Topographic Effects in Dynamic Response of a Typical Rocky Populated Slope in Lima, Peru. *Journal of Disaster Research*. Vol. 9, No. 6, pp. 946-953.

Articles submitted to Conferences

1. Gonzales C., Sekiguchi T. and Nakai S. (2016). Topographic Effects on the Seismic Response of a Sandy Populated Slope in Lima, Peru. *Proceedings of the Annual Meeting of the Japan Association of Earthquake Engineering.*

Related Articles

1. Gonzales C., Nakai S., Sekiguchi T., Calderon D., Aguilar Z. and Lazares F. (2014). Estimation of the Dynamic Properties and Seismic Response of a Populated Slope in Lima, Peru. Journal of Disaster Research. Vol. 9, No.1, pp. 17-26.

Acknowledgements

I would like to dedicate some lines to thank those who help me in the development of the current thesis. First, I am particularly grateful to my supervisor Prof. Toru Sekiguchi. His constant guidance, comprehension and assistance along these years have meant an invaluable help to me.

I would like to offer my special thanks to Prof. Shoichi Nakai. Without his patience, support, motivation and immeasurable capacity to share his knowledge and experiences, this research would not have been made possible.

My deepest gratitude is extended to the staff and professors who I had the pleasure to meet in Chiba University; to those who I took classes with and especially to Prof. Yamazaki, Prof. Okano and Prof. Arai for their comments and suggestions during the revision process of this thesis.

My sincere acknowledgment to the Japan International Cooperation Agency (JICA) and the Ministry of Education, Culture and Sports of Japan (MEXT) which financially supported my studies in Japan. This experience of more than six years has represented a personal growth in several aspects in my life and I will be infinitely grateful for that.

I owe a very important debt to the professors of the Japan-Peru Center of Earthquake Engineering Research and Disaster Mitigation (CISMID); those belonging to the Planning Department, Dr. Zenon Aguilar, MSc. Fernando Lazares and Dr. Diana Calderon, for their guidance, motivation and encouragement, and Dr. Miguel Estrada and Dr. Carlos Zavala for their comprehension, moral support and opportunity given at the beginning of this journey.

I cannot omit to comment about all the fantastic people I had the pleasure to connect and offered me their help in different circumstances during my stay in Japan. From my lab mates, international students, through fellow compatriots and musicians who never made me feel alone.

Last but not least, I would like to thank my family. Although we were physically separated, all this effort was made thinking of all of you with the only objective of, hopefully, giving you back all of what you did for me through my whole life.